

CONTROL OF PNEUMATIC-MUSCLE-ACTUATOR-DRIVEN JOINTS IN ROBOTIC APPLICATIONS

Connecting pneumatic muscle actuators with robots via a torque control interface

vorgelegt von
M. Sc.
Mirco Martens
ORCID: 0000-0003-4121-7049

an der Fakultät IV – Elektrotechnik und Informatik
der Technischen Universität Berlin
zur Erlangung des akademischen Grades

Doktor der Ingenieurwissenschaften
– Dr.-Ing. –
genehmigte Dissertation

Promotionsausschuss:

Vorsitzender: Prof. Dr.-Ing. Clemens Gühmann

Gutachter: Prof. Dr.-Ing. Jörg Raisch

Gutachter: Prof. Dr.-Ing. Ivo Boblan

Gutachter: Prof. Dr.-Ing. Thomas Seel

Tag der wissenschaftlichen Aussprache: 10. November 2021

Berlin 2021

To Larissa, Toni and Felix.

Abstract

Many robotic systems can be improved by novel, lightweight, and elastic actuators. While smaller weight reduces the kinetic energy of the system, elasticity offers the potential to absorb and release potential energy. Thus, the safety of the robot can be increased only by the use of light and elastic actuators, so that there is less energy transmitted in the case of collisions and damages or injuries would therefore be milder. In addition, stored potential energy can be used to perform motion sequences with increased energy efficiency. One type of these actuators are pneumatic-muscle-actuator-driven joints – a combination of two pneumatic-muscle-actuators (PMAs) and a pulley –, as they provide a high torque-to-weight ratio with an adjustable stiffness. Analogously to biological muscle pairs, PMA-driven joints also yield the opportunity to change their stiffness via co-contraction and, due to this, to adapt to the demands of varying tasks. The investigation of the properties of PMA-driven joints and their integration into robotic systems form the core of this dissertation. Since PMA-driven joints consist essentially of two pneumatic muscle actuators, there is an initial chapter devoted to force modeling of pneumatic muscles in addition to the study of PMA-driven joints. It compares existing force models based on a new quality measure and introduces a new model with higher accuracy.

Although there were numerous publications on robots with PMA-driven joints prior to this work, little attention has been given to their properties in general. It remains mostly unclear why a specific robot with PMA-driven joints is able to fulfill its task and how this depends on the characteristics of the chosen PMA-driven joints. Motivated by this, the present thesis provides a general discussion on the characteristics of PMA-driven joints, like their static torque range, their joint stiffness and the bandwidth of their joint torque. All results are discussed with the goal to drive a robotic system with PMA-driven joints and all essential information will be provided within this thesis. With this information at hand it will be demonstrated how to use this information to drive three different robotic systems with PMA-driven joints, successfully. Unlike most other publications on robots with PMA-driven joints, the focus of this work is less on the issue of controlling a particular robot but rather on discussing, developing and proposing a general framework for successful control of any robot with PMA-driven joints. Depending on the robot and its task, joint torques must be provided at an adequate height and speed, and only if these specifications can be met by the actuators, the robot can fulfill its task. As an interface between the robot on the one side and the actuators on the other side, a torque controller for PMA-driven joints will be developed and employed for different applications in this thesis. With this torque controller in

place, the complex PMA-driven joint dynamics can be reduced to only the static torque characteristic and the bandwidth of the controller. Since these properties of PMA-driven joints are examined in detail in this dissertation, this thesis forms the necessary basis for the successful application of PMA-driven joints in robotic systems. The simplicity of integrating PMA-driven joints under torque control into robots will be demonstrated by using three different robots. Firstly, a robot with one degree of freedom is positioned with PMA-driven joints, and secondly, the same is demonstrated for a robot with two degrees of freedom. Lastly, a rehabilitation robot with a PMA-driven joint is realized which facilitates a controlled-active-motion therapy, as used after cruciate ligament rupture.

Zusammenfassung

Viele Robotersysteme können durch neuartige, leichte und elastische Aktoren verbessert werden. Während ein geringeres Gewicht die kinetische Energie des Systems verringert, bietet Elastizität die Möglichkeit, potentielle Energie aufzunehmen und wieder abzugeben. Somit erhöht sich, allein durch den Einsatz leichter und elastischer Aktoren, die Sicherheit des Roboters, da im Falle einer Kollision weniger Energie übertragen wird und somit Schäden oder Verletzungen milder ausfallen. Darüber hinaus kann gespeicherte potentielle Energie dazu genutzt werden, Bewegungsabläufe mit erhöhter Energieeffizienz auszuführen. Aktoren mit variabler Elastizität und einem besonders hohen Kraft-zu-Eigengewicht-Verhältnis sind pneumatisch-muskel-aktuierte (PM-aktuierte) Gelenke. Analog zu biologischen Muskelpaaren haben auch PM-aktuierte Gelenke die Möglichkeit, ihre Steifigkeit durch Kokontraktion zu ändern und sich so an die Ansprüche variierender Aufgaben anzupassen. Die Untersuchung der Eigenschaften dieser Aktoren und deren Integration in Robotersysteme bilden den Kern der vorliegenden Arbeit.

Obwohl es bereits vor dieser Arbeit zahlreiche Publikationen zu Robotern mit PM-aktuierten Gelenken gab, wurden deren Eigenschaften nicht ausreichend diskutiert. In dieser Dissertation wird die Diskussion über die Charakteristiken von PM-aktuierten Gelenken bereitgestellt. Im Gegensatz zu anderen Publikationen über Roboter mit PM-aktuierten Gelenken steht weniger die Frage nach der Regelung eines bestimmten Roboters im Vordergrund, sondern vielmehr die Grundlage für eine erfolgreiche Regelung eines beliebigen Roboters mit PM-aktuierten Gelenken. Je nach Roboter und dessen Aufgabe müssen Gelenkmomente in adäquater Höhe und Geschwindigkeit bereitgestellt werden, und nur falls diese Vorgaben von den Aktoren eingehalten werden können, kann der Roboter seine Aufgabe erfüllen. Die Schnittstellenkommunikation zwischen dem Roboter und den Aktoren übernimmt ein in dieser Arbeit entwickelter Momentenregler. Mit diesem Momentenregler kann das PM-aktuierte Gelenk ausschließlich anhand seiner statischen Momentencharakteristik und der Bandbreite des Reglers beschrieben werden. Da die Eigenschaften PM-aktuierter Gelenke in dieser Dissertation vordergründig untersucht werden, bildet die vorliegende Arbeit die nötige Grundlage für einen erfolgreichen Einsatz PM-aktuierter Gelenke in Robotern. Die Einfachheit, PM-aktuierte Gelenke mit Momentenregler in Roboter zu integrieren, wird anhand dreier verschiedener Roboter gezeigt. Dabei werden jeweils ein Roboter mit einem Freiheitsgrad und ein Roboter mit zwei Freiheitsgraden in der Position geregelt sowie ein Rehabilitationsroboter, der die Möglichkeit bietet, eine Widerstandsmomententrajektorie beliebig vorzugeben.

Da PM-aktuierte Gelenke im Wesentlichen aus zwei pneumatischen Muskelaktoren bestehen, ist neben der Untersuchung von PM-aktuierten Gelenken ein Kapitel dieser

Dissertation zunächst der Kraftmodellierung pneumatischer Muskeln gewidmet. In diesem werden bestehende Kraftmodelle anhand eines neuen Gütemaßes miteinander verglichen und ein neues Model mit höherer Genauigkeit eingeführt.

Acknowledgments

There are projects in life that you cannot do alone and this thesis is such a project for me. Without the help of a lot of people, this work would not have become what it is today. I would like to thank all my colleagues and friends for being a part of this project!

First of all, I would like to thank Prof. Dr. Jörg Raisch and Prof. Dr. Ivo Boblan for giving me the opportunity to write my doctoral thesis. Further, I would like to thank Ivo Boblan for his enthusiasm and his deep understanding of pneumatic muscles and pneumatic robots. His visions of alternative drive concepts for modern robots have often inspired me and encouraged me to continue research in this important field of robotics.

I would also like to thank my colleagues and friends Alexander Pawluchin and Johannes Zawatzki. They have never hesitated to help me when I needed help. I really enjoyed the time with you at the TU Berlin and later at the Beuth Hochschule für Technik and it will always remain in my memory.

A special thanks also goes to Dr. Thomas Seel, who with his enthusiasm for dynamic systems and his many years of experience as a scientist has more than once given me the strength and inspiration to break new ground and critically question existing knowledge. I would also like to thank him for the accuracy with which he has brought both my doctoral thesis and my published papers to a level that I would not have achieved without him.

During the time of writing this thesis, I have supervised a large number of students in their theses and each of them has enriched my work with his insights. I would like to thank Michael Drummond, Florian Bandau, Amador Cabos, Stefan Kriehs, Johannes Sonnenberg and Fritz Lange. It was a pleasure to work with you.

As it is so often the case, colleagues in the background of this work have also contributed, whose essential contributions usually remain invisible in the shadows. I would like to thank the technical staff of the Institute of Control Systems at the TU Berlin Astrid Bergmann and Ralph Dorn. With their expertise, both of them have helped me to get rid of many stones lying on my way.

Finally, I would like to thank my wonderful wife Larissa Gericke-Martens and my two sons Anton Martens and Felix Martens. You gave me the strength to complete this work and made me laugh whenever you could. Without you I would not have come this far.

Contents

1. Introduction	1
1.1. Motivation	1
1.2. State of the Art	3
1.2.1. Pneumatic Muscle Actuators (PMAs)	3
1.2.2. Robots with PMA-driven Joints	5
1.3. Contribution to the State of the Art	7
1.3.1. Contributions	7
1.3.2. Related Publications of the Author	8
1.3.3. Related Theses Supervised by the Author	9
2. Fundamentals	10
2.1. Pneumatic Pressure Dynamics of time-varying Volumes	10
2.2. Modeling Serial Link Manipulators with the Lagrangian Formalism	13
2.2.1. Modeling a General Serial Link Manipulator	13
2.2.2. Modeling a 1 DOF Robot	14
2.2.3. Modeling a 2 DOF Planar Robot	16
3. Modeling of Pneumatic Muscle Actuators (PMAs)	20
3.1. Introduction	20
3.2. Experimental Force Determination	22
3.2.1. Isometric Measurement	22
3.2.2. Isobaric Measurement	24
3.2.3. Comparing the Measurement Data	25
3.3. Modeling the Static Force	27
3.3.1. Geometric Characteristics	28
3.3.2. Existing Static Force Models	29
3.3.3. A New Approach for Modeling the Static Force	30
3.3.4. An Extension of the New Approach	32
3.3.5. Methodology of Parameter Identification	33
3.3.6. A Comparison of Accuracy	35
3.4. Modeling the PMA Hysteresis	36
3.4.1. The Maxwell-Slip Model	37
3.4.2. Identifying a Specific PMA Hysteresis	37
3.5. Quality of the PMA Force Model	39
3.6. The PMA – An Actuator with Variable Stiffness?	39
3.7. Conclusion and Future Work	42

4. The PMA-driven Joint under Torque Control	44
4.1. Introduction	44
4.2. Overview	45
4.3. Torque Characteristics	47
4.3.1. Torque-to-Pressure Conversion by Force Separation – The FIT Converter	47
4.3.2. Torque-to-Pressure Conversion by Mean Pressure Definition – The PM Converter	49
4.3.3. A Comparison of Two Torque Characteristics	52
4.4. The PMA-driven Joint - An Actuator with Variable Stiffness?	52
4.4.1. Stiffness Adjustment with the FIT Converter	54
4.4.2. Stiffness Adjustment with the PM Converter	55
4.5. Pneumatic Pressure Control Inside Time-varying Volumes	56
4.5.1. The Mass Flow as Virtual System Input	57
4.5.2. A Linear Interpretation of the System Dynamics	58
4.5.3. Gain Scheduling Pressure Controller	58
4.5.4. Gain Scheduling Pressure Controller with Integral Action and Anti-windup	62
4.5.5. The Sensitivity to Modeling Errors of the Closed Pressure Control Loop	62
4.5.6. Bandwidth of the Torque Controller	64
4.6. Conclusion and Future Work	64
5. Pose Control of a Robot with 1 DOF and a PMA-driven Joint	65
5.1. A System Description	66
5.2. Definition of the Reference Angle Trajectory and Discussion of its Feasibility	67
5.3. Inner Torque Control Loop	69
5.4. Outer Angular Position Controller	72
5.5. Experimental Investigation of the Trajectory Following Behavior	74
5.6. Experimental Investigation of the Influence of Hysteresis Compensation	75
5.7. Conclusion	76
6. Pose Control of a Robot with 2 DOF and PMA-driven Joints	78
6.1. A System Description	78
6.2. Model	79
6.3. Definition of the Desired Angle Trajectory and Discussion of its Feasibility	80
6.4. Design of the Inner Torque Controller	82
6.5. Pose Control	83
6.5.1. Backstepping Controller without Time-delayed Torque Signals	84
6.5.2. Disturbance Torque Observer	85
6.6. Experimental Investigation of the Pose Controller	87
6.7. An Interim Conclusion	88
6.8. Pose Control with Time-delayed Torque Inputs	89
6.8.1. Backstepping Controller	89

6.8.2. Disturbance Torque Observer	91
6.9. Experimental Investigation of the Pose Controller with Time-delayed Torque Signals	92
6.10. Conclusion	93
7. Controlled Active Motion (CAM) Control of the Rehabilitation Robot PMA-CAMOPED	95
7.1. Introduction	95
7.2. A System Description	96
7.3. Design of a CAM Controller	98
7.4. Experimental Results	102
7.5. Conclusion	103
8. General Conclusion and Outlook	104
8.1. General Conclusion on Modeling PMAs	104
8.2. General Conclusion on the Torque Control Interface for PMA-driven Joints	105
8.3. General Conclusion on Robotic Systems with PMA-driven joints	106
8.4. Future Research	107
List of Figures	XV
List of Tables	XVII
Acronyms	XVIII
List of Symbols	XIX
Bibliography	XXIII
A. Appendix	i
A.1. Derivatives for Chapter 3 and 4	i
A.2. Derivatives for Chapter 6	i

1. Introduction

1.1. Motivation

Assembling products fully autonomously was the major motivation from which the first robots were born. While at first, the accuracy and the speed were improved over decades – for the sake of higher lot sizes and profit –, during the last decades, the human-robot coexistence or even the physical human-robot interaction defines new demands for modern robotic systems [28, 16]. Furthermore, robots are leaving the factory buildings and conquering everyday life [1]. Due to the changing requirements and tasks, many new types of robots like humanoids or mobile robots were developed, especially during the last years.

The closer humans and robots are getting, the more the question of safety arises. While robots that are made purely for autonomous assembly have to be very stiff to provide good accuracy at high speed and need not consider human safety as much, robots that are acting closer to humans, or those getting into direct contact with them, have to ensure human safety at any time. Nowadays, it is common sense that robots made for collaboration with or assistance of humans have to be lightweight and passively compliant [74], such that the energy stored in the moving robot and the energy that is set free in case of collisions is kept as small as possible. Since pneumatic muscle actuators (PMAs) are very light, able to provide very high forces, and are passively compliant, driving robots with these actuators is a promising strategy to achieve higher safety levels.

Besides their intrinsic safety, compliant actuators like PMAs are a promising technology for another reason. Since their passive compliance makes them behave not only as pure force source but also as mechanical spring, they have the ability to store potential energy. This advantage can be illustrated by a robotic leg in an upright position which jumps periodically, i.e. when the phase of falling downward and the phase of jumping upward are alternating. Starting in the falling-phase, in the moment when the foot of the robot touches the ground for the first time, the actuators have to carry the weight and also – since the system is slowing down – the inertia of the robotic leg. In case the actuators are compliant, they can store some amount of the energy by getting pretensioned and releasing the energy again during the jumping phase. As a result, compliant actuators are expending less energy in comparison to non-compliant actuators without an energy reservoir. Following the argumentation of Van Ham et al. [74], compliant robots and actuators will mostly come into focus not for their higher

safety but for their energy efficiency. This statement gets emphasized by the pursuit of efficiency in nature, since the composition of force-exerting actuators – organic muscles – and compliant, energy-storing, structures – tendons – is the same for human beings and most animals. In accordance to the ideas of Charles Darwin, a compliant actuation system is advantageous for moving through and adapting to everyday life. This is then especially true for biologically-inspired robots like humanoids or animal-like robots.

Another encouraging attribute of so-called PMA-driven joints is their ability to vary their stiffness via co-contraction. As it will be explained in more detail in Chapter 4, a PMA-driven joint is a combination of two muscles which are pulling around a common joint, i.e. both muscles are acting as an antagonistic pair. The co-contraction, i.e. the joint stiffness, can be increased if both muscles are pulling simultaneously. In bodies of human beings and most animals, the concept of co-contraction (or co-activation) is used by the central nervous system to stiffen the body and, due to this, to increase the accuracy and/or the speed of movements if needed [33]. Equivalent behavior can be transferred to a robot with PMA-driven joints. In addition, a robot with PMA-driven joints can execute movements with more natural appearance, i.e. the trust of a human user in the robot can be improved [14] by the choice of compliant, co-contraction-providing actuators.

Since most robots have only revolute joints – which enable a rotation around one axis – and PMAs are only able to pull linearly, an antagonistic pairing of two PMAs which are pulling around one joint is common practice. Although many publications are proving that PMA-driven robots are controllable and appropriate to fulfill different tasks, it is remarkable that none of these PMA-driven robots ever left the laboratories.

In contrast to their advantageous attributes, a still small number of PMA-driven robots indicates that the challenges of using PMAs seem to outweigh their advantageous in the eyes of most researchers. The question is: Why is that? A reasonable explanation of this situation is the existence of a gap of knowledge between engineers dealing with PMAs and robotic engineers. This gap is mainly constituted by two parts: Firstly, finding one valid model of the PMA itself is rather challenging. Although different models of the PMA exist, there is no consensus about one general applicable model, nor are there any established criteria for measuring the quality of the models. Secondly, by driving a robot pneumatically, the positioning control problem gets complicated due to the non-linearity of the pressure dynamics. From this perspective it is understandable that most engineers stick to electrical motors, since their use for driving robots is way more established and already well studied and discussed. This partly missing discussion about PMA-driven joints, their specific characteristics and dynamics and their influence to the problem of controlling a robot, will be provided during the next chapters of this theses.

By keeping the perspective of an engineer who wants to build and control a robot, mainly two pieces of information about the actuator are of interest:

1. What force or torque is the actuator able to exert? What is the force/torque range?
2. How fast can the force/torque be provided? What is the actuator's bandwidth?

Only with this information at hand, the decision whether or not the actuator is suitable to drive the robot can be made.

Walking towards a solution of this problem, this dissertation strives to create and insert the missing link between robotics on the one hand and PMA-driven joints on the other hand. By definition of a torque-control-interface for PMA-driven joints, the challenging non-linearities are handled internally. As a result of this interface, the torque-controlled PMA-driven joint is fully described by its static torque range and its bandwidth, such that their integration into robotic systems gets simplified. Their integration into three different robotic systems, discussed in the following thesis, will prove the generality and simplicity of torque-controlled PMA-driven joints.

1.2. State of the Art

1.2.1. Pneumatic Muscle Actuators (PMAs)

A PMA is an actuator that mainly consist two stiff end-connectors and a rubber tube between them. By putting pressure inside the PMA it contracts in length, while the diameter expands, very much alike biological muscles. By connecting the PMA to a load, the load can be pulled by the actuator, i.e. the PMA exerts a pulling force. The PMA force depends on its length and its internal pressure and has been studied for decades by many researchers [48], whereby finding the most accurate model for describing the PMA force represents the major challenge. The PMA force can be subdivided into a static force and a dynamic force, whereby the former one dominates the PMA force by far.

Starting with the static force, it is remarkable that a lot of different models can be found in literature. The most popular approach, modeling the static PMA force, was introduced by Chou and Hannaford [23], yet it is shown in Boblan [17] that this model is not valid for PMAs produced by the manufacture Festo. Since Festo is the only industrial manufacturer of PMAs, nowadays most PMA-driven robots are driven by Festo PMAs. Models that were developed for the specific use on Festo PMAs are the models of Hildebrandt et al. [36], Wickramatunge and Leephakpreeda [79], and Sárosi et al. [61]. What all of them have in common is that they model the static PMA force as a function of the PMA length (or contraction rate) and its pressure. Furthermore, all models have some parameters that must be tuned by comparison to a measured static force map describing the PMA of interest. However, there is to date no consensus available to make different models comparable, neither about how to measure the PMA force correctly, nor about any superior method for estimating the

free model parameters, nor about any measure of quality. The present thesis aims at providing enough information to enable the definition of such a consensus in future. Moreover, despite important achievements the shortcomings of existing literature are still remarkable.

Although Hildebrandt et al. [36] mentioned that the free parameters are determined via minimizing the least squares error between the measured PMA force and the force calculated by the model, the cost function is not explicitly shown, so that reproducing the findings is barely possible. In addition, the achieved approximation of the measured PMA force is at worst greater than 15 % of the maximum PMA force, which is about 1.5 kN in this case. In other words, the difference between the true and the calculated force can be greater than 225 N. In Wickramatunge and Leephakpreeda [79], the presented model of the PMA force is adapted to a measured PMA force map via minimizing the least-squares error and the cost function is explicitly given. Notwithstanding, no measure of quality of the presented model is defined nor is the model validated. Due to this, it remains unexplained whether or not the model of Wickramatunge and Leephakpreeda [79] is suitable to describe the PMA force with sufficient accuracy. Although it is not explained how the free model parameters PMA force model of Sárosi et al. [61] can be estimated, an evaluation of their model is given. As proven by measurement, their model is close to the measured PMA force, yet an error plot or any other error quantification is missing. Due to this, the accuracy of the model is only given qualitatively.

In summary: Many different models describing the PMA force were already developed; however, there is no generic approach for accessing their accuracy, no generalized method for identifying their free tunable parameters and no method for making different models comparable. As a result the choice of a suitable PMA model is mostly impossible. The present thesis strives to fill this gap of knowledge.

In addition, it is possible to measure the static PMA force in two different setups. Although Minh et al. [54] are saying that the measured force can vary significantly in dependency of the chosen measurement setup, it is not clear which setup is advantageous for model identification and controller design. This further complicates the definition of best practice for PMA force modeling.

As it will be shown in Chapter 3, the quality of all existing models varies significantly. Furthermore, a systematic identification method to estimate free parameters and a measure of quality will be introduced, which simplifies the comparison of methods. In addition, a novel approach modeling the PMA static force will be introduced. It will be shown that this new approach approximates the measured PMA static force with improved precision than existing models.

The dynamic PMA force is mostly caused by hysteresis and investigated e.g. by Minh et al. [54], Vo-Minh et al. [76], and Schindele and Aschemann [64]. In contrast to the static force, a comparison of accuracy of different models describing the dynamic PMA force is given in Aschemann and Schindele [9]. Due to this already existing comparison,

the focus is set to the investigation of the static PMA force in this dissertation. The dynamic PMA force will only be investigated on the margin of Chapter 3.

1.2.2. Robots with PMA-driven Joints

Since most robots have only revolute joints [47], i.e. they are driven only by joint torques, and PMAs are actuators that can only pull linearly in one direction, it is common practice to combine two PMAs via a rope and a pulley to create an antagonistic pair, as can be found in e.g. Noritsugu and Tanaka [56], Boblan et al. [19], and Büchler et al. [20]. The particular configuration of two PMAs will be further denoted as a PMA-driven joint and treated as an actuator of its own. This is reasonable since a PMA-driven joint has its own characteristics. Although it is of crucial importance to guarantee the feasibility of the robotic system to fulfill a specifically controlled task, the PMA-driven joint has not been investigated in its entirety so far, and it is typically discussed only on the margin. The focus of most publications about robots with PMA-driven joints is set to the controller design for a particular robot while the choice of a particular set of PMA-driven joints is mostly left open.

In Hildebrandt et al. [36], the tool center point (TCP) of a PMA-driven robot with 2 degree of freedom (DOF) is controlled by a cascade-structured motion controller with an underlying torque controller. While the overlying flatness-based motion controller is designed for the whole robot, two equal torque controllers are regulating the joint torque of the first and second PMA-driven joint, respectively. It is shown that by controlling the joint torques on a lower level, the motion controller design gets simplified. Furthermore, the mean pressure of all PMAs is calculated so that the joint stiffness of both joints is at its respective maximum. On the one hand, Hildebrandt et al. [36] are showing that the chosen cascade-structured control concept is suitable for making the robot with PMA-driven joints follow the desired trajectory. On the other hand, it remains unclear how to apply the findings to another robot with PMA-driven joints because no discussion of the requirements of the overlying position controller with respect to the PMA-driven joints is given. This would be important to understand what preconditions are necessary to enable a successful position controller design. Due to this, it remains unclear how to achieve an equivalent controller performance with the same controller design but another robot with different PMA-driven joints.

Although the parallel robot with two PMA-driven joints and the overlying motion control approach is different in Schindele and Aschemann [63], the limitation of their controller design to their particular system is close to Hildebrandt et al. [36]. Schindele and Aschemann [63] are demonstrating that a cascaded control structure reduces the complexity of the control problem, but it remains unclear what the characteristics of the PMA-driven joints are and how this guarantees the feasibility of the robotic system to follow the reference TCP trajectory. Furthermore, the ability of PMA-driven joints to vary their joint stiffness remains completely disregarded within their controller design.

Another exemplary robot with PMA-driven joints is the lower limb exoskeleton of Aguilar-Sierra et al. [3], which is driven by a combination of PMA-driven joints and harmonic drives. Thereby, the knee and hip joint of both legs are actuated respectively. In accordance with most other publications about robots with PMA-driven joints, the authors of this paper are using a cascade-structured joint angle controller with underlying torque controller, which controls the joint torque of the knee and hip joints individually. Although the authors are showing that the control goal can be achieved, no information about the feasibility of the desired reference trajectory is given either. Due to this, it remains unclear why the system is able to fulfill the desired control task. As a result, the findings are hardly transferable to another robotic system with PMA-driven joints.

In summary, it is remarkable that most publications about robots with PMA-driven joints share the demonstration of an individual control task fulfilled by sufficient control. However, it remains mostly unclear how the feasibility of the control goal is guaranteed by the right choice and control of the PMA-driven joints. Due to this, the findings of most publications are only valid for particular robots but not for a larger class of robots with PMA-driven joints. To clarify whether or not a PMA-driven joint is suitable for a particular robotic system, an information about its torque range and its torque bandwidth should always be provided. Furthermore, the stiffness of a PMA-driven joint can be varied via the mean pressure of both PMAs, but this feature of a PMA-driven joint remains mostly unused.

As a contribution to the current state of the art, this dissertation, specifically Chapter 4, will investigate the attributes of PMA-driven joints in a more general way in comparison to existing investigations and their effect on the robotic system that is actuated by the PMA-driven joint. Chapter 4 will provide a general concept of how to analyze and design a PMA-driven joint in accordance with the needs of a particular robotic system and a given control task. With the information about the static and dynamic characteristics of a PMA-driven joint at hand, it can be clarified in advance what torque range the PMA-driven joint has to provide and what bandwidth the torque controller has to have. Due to this, the design process of a robot with PMA-driven joints gets simplified. In addition, a discussion about the joint stiffness of PMA-driven joints will be given, i.e. their stiffness range is defined quantitatively.

The generality of the findings of Chapter 4 will be demonstrated by their application to a 1 DOF robot in Chapter 5, a 2 DOF robot in Chapter 6, and a rehabilitation robot in Chapter 7. All three robotic systems are actuated by PMA-driven joints and their different control goals will be achieved by following the same methodology.

1.3. Contribution to the State of the Art

In the current section, the contributions of this dissertation are listed briefly. The findings of this thesis were to some extent already published in conference and journal papers and supported by different supervised Bachelor and Master theses.

1.3.1. Contributions

1. Modeling PMAs

- Comparison of different approaches modeling the static PMA force with a novel quality measure
- Development of two new approaches for modeling the static PMA force, describing the static PMA force more precisely than any existing approaches
- Investigation and quantification of the PMA's mechanical stiffness of the static force

2. Investigation of PMA-driven joints under torque control

- Definition of the PMA-driven joint as a standalone actuator
- Investigation of the static attributes of a PMA-driven joint defined by two different methods of torque-to-pressure conversion
 - Broad investigation of the static torque characteristic for torque-to-pressure conversion under the condition of a common mean pressure (denoted as the PM converter)
 - Introduction of a new torque-to-pressure conversion by separation of force and the definition of a common initial tension (denoted as the FIT converter)
 - Investigation of the static torque characteristic of a PMA-driven joint as a result the novel FIT converter.
 - Investigation and quantification of the torsional stiffness of a PMA-driven joint with respect to PM- and the FIT-converter, respectively
- Investigation of the torque control bandwidth of a PMA-driven joint
- Development of an adaptive pressure controller for time-varying volumes with measurable volume
- Development of an adaptive pressure controller with integral action and anti-windup for time-varying volumes with measurable volume

3. Investigation of a 1 DOF robot with PMA-driven joint

- Proof of concept for the novel FIT torque control approach for PMA-driven joints as an underlying controller embedded inside an overlying position control loop
 - Comparison of PM and FIT converters with respect to the tracking error of the robot
 - Integration of a hysteresis compensation strategy to the novel torque control framework for PMA-driven joints
4. Investigation of a 2 DOF planar robot with PMA-driven joints
- Application and investigation of the novel torque control interface for PMA-driven joints inside a multi-dimensional robot
 - Development of a backstepping controller for the present 2 DOF planar robot
 - Development of a disturbance torque observer that the controller can be extended with, i.e. the stationary error vanishes
 - Development of a backstepping controller for the present 2 DOF planar robot and time-delayed torque input signals
 - Development of a disturbance torque observer for a system with time-delayed torque inputs, the controller can be extended with, i.e. the stationary error vanishes
5. Development of a novel, PMA-driven rehabilitation robot
- Development of a controller that enables a continuous active motion (CAM) therapy like it is applied to patient with knee injuries

1.3.2. Related Publications of the Author

As it is common for PhD-thesis, the content was developed over a few years and interim results and findings were already published on conferences and within journals. The following publications were published by the author, before summarizing all results in the present thesis:

[50] M. Martens, A. Passon, and I. Boblan. A sensor-less approach of a torque controller for pneumatic muscle actuator driven joints. In *2017 3rd International Conference on Control, Automation and Robotics*, pages 477–482. IEEE, April 2017

[48] M. Martens and I. Boblan. Modeling the static force of a festo pneumatic muscle actuator: A new approach and a comparison to existing models. *Actuators*, 6(4.33), 2017

- [49] M. Martens and I. Boblan. Erratum: Modeling the static force of a festo pneumatic muscle actuator: A new approach and a comparison to existing models. *actuators* 2017, 6, 33. *Actuators*, 7, 2018
- [51] M. Martens, T. Seel, and I. Boblan. A decoupling servo pressure controller for pneumatic muscle actuators. In *23rd International Conference on Methods and Models in Automation and Robotics*. IEEE, 2018
- [52] M. Martens, T. Seel, J. Zawatzki, and I. Boblan. A novel framework for a systematic integration of pneumatic-muscle-actuator-driven joints into robotic systems via a torque control interface. In *Actuators*, volume 7, page 82. Multidisciplinary Digital Publishing Institute, 2018
- [53] M. Martens, J. Zawatzki, T. Seel, and I. Boblan. A pneumatic-muscle-actuator-driven knee rehabilitation device for CAM therapy. In *41st International Engineering in Medicine and Biology Conference*. IEEE, 2019

1.3.3. Related Theses Supervised by the Author

In addition to the authors publications, the research presented in this thesis was supported by the following bachelor and master thesis:

- [31] M. Drummond. Development of a test rig for the automated measurement of the static force characteristic of pneumatic muscle actuators. Bachelor's thesis, TU Berlin, Germany, 2016
- [44] S. Kriehs. Vergleich verschiedener messprinzipien zur längenmessung pneumatischer muskelaktoren. Bachelor's thesis, TU Berlin, 2017
- [12] F. Bandau. EMG-basierte regelung und evaluation eines ellenbogen-exoskeletts. Master's thesis, TU Berlin, 2018
- [21] A. Cabos. Parameter identification of a pneumatic servo valve and design of a model-based pressure controller. Master's thesis, TU Berlin, Germany, 2018
- [68] J. Sonnenberg. Dynamische mobilisierung von patienten mittels aktoren. Master's thesis, Beuth Hochschule für Technik Berlin, Germany, 2018
- [81] J. Zawatzki. Konstruktion und regelung eines mit pneumatischen muskeln angetriebenen humanoiden nackengelenkes. Master's thesis, TU Berlin, 2018

2. Fundamentals

The present chapter will simplify the understanding of this thesis by briefly discussing some selected fundamentals of pneumatic systems on the one hand and robotics on the other hand. Instead of explaining every detail – this would go beyond the scope of this thesis – this chapter is kept as short as possible.

For more detailed information about the fundamentals of pneumatic systems and pneumatic pressure control, the author of this dissertation refers to Beater [13], Watter [78], Grollius [34] and Murrenhoff [55].

Especially for robotics, there is a great number of books available, which give excellent introductions to this field. The two books mostly used for this thesis are Siciliano and Sciavicco [67] and Lynch and Park [47].

2.1. Pneumatic Pressure Dynamics of time-varying Volumes

In a nutshell, a pneumatic system always consists of a pressure-filled chamber that can be either connected to the constant up-side pressure – mostly a constant supply pressure – and a constant down-side pressure, mostly represented by the atmospheric pressure. The atmospheric pressure represents the minimum pressure for this thesis; hence, vacuum technology will be fully excluded from this thesis' discussion.

A pneumatic valve connects the supply pressure, respectively the atmospheric pressure with the chamber, in dependency of the valve control signal. The fluid – air for pneumatic systems – streams along the tubes into or from the chamber. Although long tubes have their own dynamics, delaying the fluids massflow, this influence can be neglected for short tubes [60]. During all experiments presented within the following chapters, only short tubes were used and therefore the tube dynamics were neglected. As long as air streams into the chamber, the inner pressure increases until it equals the supply pressure. In case the chamber is made of an elastic material, the volume will change, as it is the case for PMAs. Due to this, the focus is set on time-varying volumes, but this is no loss of generality since constant volumes can be seen as a sub-group of time-varying volumes.

Within the following section, the basic ideas of modeling pneumatic systems will be explained. A state-space model, describing the pressure dynamics, will be obtained

by exploiting the ideal gas law. Later in this thesis the state model will be used to design a pressure controller, which controls the pressure inside a volume according to the demands of a pneumatically-driven system.

The pressure dynamics of a time-varying volume consists of three different parts: Firstly, the air inside the air-filled volume has its own fluid dynamics. Secondly, the mass flow \dot{m} shaped by the pneumatic valve and the valve dynamics themselves must be included within a proper model.

Since air behaves like an ideal gas, its dynamics

$$\dot{p} = \frac{\chi R_{\text{gas}} T}{V} \dot{m} - \chi p \frac{\dot{V}}{V} \quad (2.1)$$

is described accurately by the ideal gas law and can be found e.g. in [13]. In (2.1) p represents the absolute pressure, V the volume, T the temperature, χ is the polytropic coefficient and R_{gas} (288 Nm/kgK under reference conditions) is called the ideal gas constant. With respect to the input signal \dot{m} , Eq. (2.1) has an input-affine structure, such that the change in pressure depends only linearly on the mass flow. In case of PMAs, the polytropic exponent was identified by measurement as $\chi = 1.26$ by Hildebrandt et al. [36], i.e. state changes of the included air are somewhere in between isothermal ($\chi = 1$) and isentropic ($\chi = 1.4$) conditions.

In accordance to the ISO 6358 or [13], the mass flow passing through a pneumatic valve can be calculated as follows

$$\dot{m} = \begin{cases} C(x_v) p_s \rho_0 \sqrt{\frac{T_0}{T}} & 0 \leq \frac{p}{p_s} < b \wedge x_v \in [0,1] \\ C(x_v) p_s \rho_0 \sqrt{\frac{T_0}{T}} \sqrt{1 - \left(\frac{p/p_s - b}{1-b}\right)^2} & b \leq \frac{p}{p_s} \leq 1 \wedge x_v \in [0,1] \\ C(x_v) p \rho_0 \sqrt{\frac{T_0}{T}} \sqrt{1 - \left(\frac{p_0/p - b}{1-b}\right)^2} & b \leq \frac{p_0}{p} \leq 1 \wedge x_v \in [-1,0) \\ C(x_v) p \rho_0 \sqrt{\frac{T_0}{T}} & 0 \leq \frac{p_0}{p} < b \wedge x_v \in [-1,0) \end{cases} \quad (2.2)$$

In this equation, $p_0 = 100$ kPa, $T_0 = 293.15$ K and $\rho_0 = 1.185$ kg/m³ represent the pressure, the temperature and the density of air under reference conditions, respectively [13]. Furthermore, x_v represents the valve slide stroke, T the temperature, C is called the sonic conductance and b the critical pressure ratio of the valve.

The mass flow (2.2) can be read in the following way: Dependent on the valve slide stroke x_v and the pressure ratio p/p_s , respectively p_0/p , (2.2) distinguishes four different cases. For $x_v \in [0,1]$, the supply pressure p_s is connected to the volume. For $x_v \in [-1,0)$, the volume is connected to atmospheric pressure. Additionally, the fluid flows with the local speed of sound in at least one section of the valve for $0 \leq p/p_s < b$, respectively $0 \leq p_0/p < b$ (choked flow), or with subsonic speed for $b \leq p/p_s \leq 1$, respectively $b \leq p_0/p \leq 1$ (subsonic flow).

The general form of (2.2) is adapted to a specific form by inserting a specific critical pressure ratio b and sonic conductance $C(x_v)$, which characterize a particular valve. For the present thesis this will be a Festo MPYE-5-1/8-LF-010-B proportional servo valve for all applications and experimental testing. The constant critical pressure ratio of this valve is identified by measurement to $b = 0.35$. The sonic conductance C has been measured in dependency of the normalized valve slide stroke. The measured values are depicted in Figure 2.1 and are taken from Cabos [21].

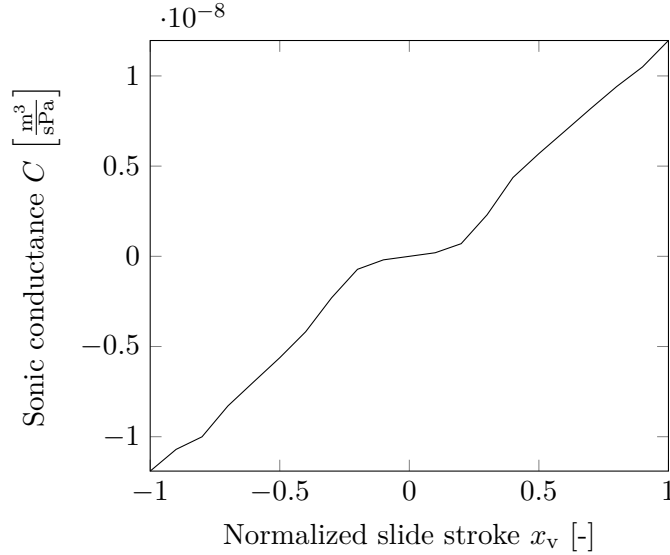


Figure 2.1.: Sonic conductance $C(x_v)$ in dependency of the normalized valve slide stroke x_v of a Festo MPYE-5-1/8-LF-010-B proportional servo valve taken from Cabos [21]

The slide stroke of the Festo MPYE-5-1/8-LF-010-B is controlled by an internal position controller. According to [41] and [60], the transfer function, which connects the normalized valve control signal $u_v \in [-1,1]$ and the normalized valve slide stroke $x_v \in [-1,1]$, can be approximated by a first-order lag filter. The transfer function is given in the frequency domain, where X_v and U_v are the unilateral Laplace transforms, with Laplace variable s , of the control signal and the valve slide stroke, respectively:

$$\frac{X_v(s)}{U_v(s)} = \frac{1}{T_v s + 1}. \quad (2.3)$$

The time constant $T_v = \omega_v^{-1} = (2\pi f_v)^{-1}$ can be calculated from the valve cut-off frequency $f_v = 95$ Hz [41] provided in the data sheet of the Festo MPYE-5-1/8-LF-010-B proportional servo valve. Since the bandwidth of this particular valve is very high, the influence of (2.3) will be fully neglected within this thesis, i.e. $x_v(t) = u_v(t) \forall t$.

2.2. Modeling Serial Link Manipulators with the Lagrangian Formalism

In a nutshell, the present thesis investigates the application of PMA-driven joints in robotic systems. Thereby, the actuator itself but especially its static and dynamic attributes and their influence to the robotic system are in focus. Accordingly, this thesis does not focus on the extension of the theory about modeling and controlling robots but finding and investigating a suitable and general interface between PMA-driven joints on the one hand and robotics on the other hand. As two exemplary robots, a 1 DOF robot with PMA-driven joint will be investigated in Chapter 5 and a 2 DOF robot in Chapter 6. While the 1 DOF robot represents the simplest platform to investigate the actuator PMA-driven joint in general, the 2 DOF robot gives more insights into coupling effects, which only occur in multi-dimensional robots.

This section will only provide the fundamentals of robotics for understanding the robotic systems that were part of the investigations of Chapter 5 and 6. Starting with the Lagrange formalism to determine the equation of motion of a robot, this section will provide the modeling of a 1 DOF and a 2 DOF planar robot. For more general information about robotics, the reader is referred to standard text books about robotics like Siciliano and Sciavicco [67] or Lynch and Park [47].

2.2.1. Modeling a General Serial Link Manipulator

Typically robots consist of rigid parts called links that are connected via joints. Although joints can be either *prismatic* – enabling a sliding motion along one axis – or *revolute* – enabling a rotation around one axis –, most robots have only revolute joints, as it is the case with the robots of interest in the following chapters. The focus is therefore set on robots with only revolute joints.

The physical behavior of a robot is described by its *equation of motion* or *forward dynamics*

$$\ddot{\varphi} = M^{-1}(\varphi) [\tau - h(\varphi, \dot{\varphi})], \quad (2.4)$$

where $\varphi \in \mathbb{R}^n$ represents a minimum set of n generalized coordinates (degrees of freedom) – angles in case of only revolute joints –, $\dot{\varphi} \in \mathbb{R}^n$ and $\ddot{\varphi} \in \mathbb{R}^n$, its first and second time derivatives, and $\tau \in \mathbb{R}^n$, a set of generalized forces, which are torques in case of only revolute joints. These joint torques are summarizing all external torques and can be further subdivided into the actuation torque exerted by the actuators and energy dissipating torques e.g. friction. The mass matrix $M \in \mathbb{R}^{n \times n}$ is positive-definite and invertible [47] and holds all information about the robot's mass and inertia. At last, the vector $h(\varphi, \dot{\varphi}) \in \mathbb{R}^n$ lumps together all torques occurring from gravity, centripetal, or Coriolis effects.

Since the mass matrix is symmetric and positive definite, Eq. (2.4) can be directly

calculated from the *inverse dynamics*

$$\tau = M(\varphi)\ddot{\varphi} + h(\varphi, \dot{\varphi}). \quad (2.5)$$

An elegant way to derive this equation was developed by Joseph-Louis Lagrange and is therefore denoted as the Lagrangian formalism. Following the ideas of Lagrange, any change of a loss-free mechanical system can be explained by the ratio of its kinetic energy \mathcal{K} and its potential energy \mathcal{P} . Lumped together, this statement can be expressed by the Lagrange function

$$\mathcal{L} = \mathcal{K} - \mathcal{P}, \quad (2.6)$$

where the kinetic energy of a rigid body, moving in a plane

$$\mathcal{K} = \frac{1}{2} \left(mv_S^2 + \Theta^{(S)} \dot{\varphi}^2 \right) \quad (2.7)$$

is a result of the translational velocity v_S of the center of gravity S , the body mass m , the angular velocity $\dot{\varphi}$, and the body inertia $\Theta^{(S)}$ around S . The potential energy

$$\mathcal{P} = mgh_s \quad (2.8)$$

in relation to an arbitrary zero level is defined by the body mass, the gravity g , and the distance to the level of zero potential energy. Following the ideas of the Lagrangian formalism, the inverse dynamics is derived by

$$\tau = \frac{d}{dt} \left(\frac{\partial \mathcal{L}}{\partial \dot{\varphi}} \right) - \frac{\partial \mathcal{L}}{\partial \varphi}, \quad (2.9)$$

since the joint torques represent so-called non-conservative generalized forces. A concrete solution of (2.9) will be provided for a 1 DOF and a 2 DOF serial link robots in the next to sections.

2.2.2. Modeling a 1 DOF Robot

The robot used for all investigations in Chapter 5, is a robot with 1 DOF, as depicted schematically in Fig. 2.2.

The robot's only generalized coordinate is given by the joint angle $\varphi \in \mathbb{R}$. Hence, the generalized velocity is $\dot{\varphi} \in \mathbb{R}$. Furthermore, the robot is defined by constant parameters like the link mass m , its length l , the distance l_s between the base joint, the center of gravity S of link 1, and its inertia with respect to S .

To derive the robot's inverse kinematics via the Lagrange formalism, it is necessary to combine the kinetic energy

$$\mathcal{K} = \frac{1}{2} \left(\Theta^{(S)} + ml_s^2 \right) \dot{\varphi}^2, \quad (2.10)$$

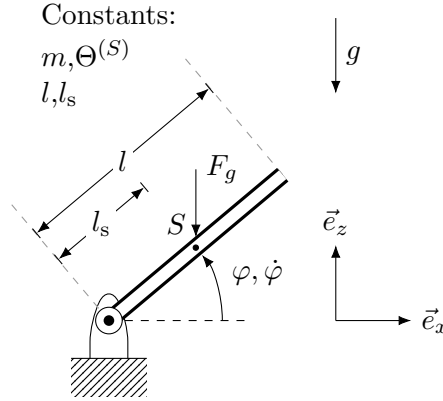


Figure 2.2.: Schematic of the planar robot with 1 DOF

and the potential energy

$$\mathcal{P} = mgl_s \cos \varphi \quad (2.11)$$

of the robot and combine them to the Lagrange function

$$\mathcal{L} = \frac{1}{2} \left(\Theta^{(S)} + ml_s^2 \right) \dot{\varphi}^2 - mgl_s \cos \varphi. \quad (2.12)$$

The partial derivative of the Lagrange function with respect to the generalized velocity is

$$\frac{\partial \mathcal{L}}{\partial \dot{\varphi}} = \left(\Theta^{(S)} + ml_s^2 \right) \dot{\varphi} \quad (2.13)$$

and its time derivative is given by

$$\frac{d}{dt} \left(\frac{\partial \mathcal{L}}{\partial \dot{\varphi}} \right) = \left(\Theta^{(S)} + ml_s^2 \right) \ddot{\varphi}. \quad (2.14)$$

Furthermore, the partial derivative of the Lagrange function with respect to the generalized coordinate is defined by

$$\frac{\partial \mathcal{L}}{\partial \varphi} = -mgl_s \sin \varphi. \quad (2.15)$$

Finally, the inverse dynamics

$$\tau = \left(\Theta^{(S)} + ml_s^2 \right) \ddot{\varphi} - mgl_s \sin \varphi. \quad (2.16)$$

can be found by equating the sum of non-conservative torques $\tau \in \mathbb{R}$ and the derivatives of the Lagrange function. Thereby, $M(\varphi) = \left(\Theta^{(S)} + ml_s^2 \right) \in \mathbb{R}$ represents the mass matrix and $h(\varphi, \dot{\varphi}) = -mgl_s \sin \varphi \in \mathbb{R}$ the Coriolis vector.

Due to friction, a robotic system is damped. As a non-conservative torque this damping will be explicitly separated from τ , the vector of all non-conservative torques. As a result the inverse kinematics with linear damping is given by

$$\tau = \left(\Theta^{(S)} + ml_s^2 \right) \left[\ddot{\varphi} + 2\delta\dot{\varphi} - \frac{mgl_s}{\Theta^{(S)} + ml_s^2} \sin \varphi \right]. \quad (2.17)$$

The fraction

$$\omega_0^2 := \frac{mgl_s}{\Theta^{(S)} + ml_s^2} \quad (2.18)$$

defines the squared natural frequency ω_0^2 , the eigenfrequency of the non-damped mechanical system. The constant δ is called the damping factor and defines the energy dissipation from the mechanical system due to e.g. friction. Finally, the inverse kinematics of the system is given by

$$\tau = \frac{mgl_s}{\omega_0^2} \left[\ddot{\varphi} + 2\delta\dot{\varphi} - \omega_0^2 \sin \varphi \right]. \quad (2.19)$$

Thus, a model describing a 1 DOF is now available and will be used for a position controller design in Chapter 5.

2.2.3. Modeling a 2 DOF Planar Robot

The 2 DOF robot depicted in Fig. 6.1 is an open chain or serial link manipulator, with only revolute joints. It can be described by its inverse dynamics (2.5), where $\varphi = (\varphi_1, \varphi_2)^T \in \mathbb{R}^2$ and $\dot{\varphi} = (\dot{\varphi}_1, \dot{\varphi}_2)^T \in \mathbb{R}^2$ are representing the joint angles and angular velocities, and $\tau \in \mathbb{R}^2$ represents the joint torques driving the robot. The inertia representing mass matrix $M(\varphi) \in \mathbb{R}^{2 \times 2}$ is symmetric, positive-definite, invertible, and $h(\varphi, \dot{\varphi}) \in \mathbb{R}^{2 \times 1}$ lumps together all centrifugal and Coriolis effects [47]. Since the robot only moves in a plane that is perpendicular to gravity, h is free of any influence of gravity.

In addition, the 2 DOF robot is defined by a set of constants like the masses m_1, m_2 , the link lengths l_1, l_2 , the position of each link center of gravity S_1, S_2 – defined by the distance from the previous joint l_{s1}, l_{s2} –, and the inertia $\Theta_1^{(S1)}, \Theta_2^{(S2)}$ with respect to the center of gravity of link one or two, respectively.

Next, the 2 DOF robot will be modeled, i.e. its mass matrix M and its Coriolis vector h are to be determined. This will be done by applying the Lagrangian formalism to the system. Since the robot acts in a plane perpendicular to gravity, the potential energy of all robot links is $\mathcal{P} = 0$. Due to this, the Lagrange function equals the sum of all kinetic energy, i.e.

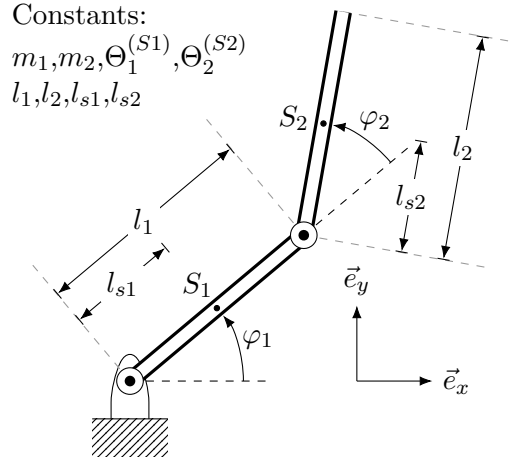


Figure 2.3.: Schematic of the planar robot with 2 DOF

$$\mathcal{L} = \mathcal{K} = \frac{1}{2} \left(\Theta_1^{(S1)} \dot{\varphi}_1^2 + m_1 v_{s1}^2 + \Theta_2^{(S2)} (\dot{\varphi}_1^2 + \dot{\varphi}_2^2) + m_2 v_{s2}^2 \right), \quad (2.20)$$

whereby the unknown velocities v_{s1} and v_{s2} can be determined by the time derivatives of the position vector of S_1

$$r_{s1} = l_{s1} \cos \varphi_1 \vec{e}_x + l_{s1} \sin \varphi_1 \vec{e}_y \quad (2.21)$$

and S_2

$$r_{s2} = [l_{s1} \cos \varphi_1 + l_{s2} \cos(\varphi_1 + \varphi_2)] \vec{e}_x + [l_{s1} \sin \varphi_1 + l_{s2} \sin(\varphi_1 + \varphi_2)] \vec{e}_y, \quad (2.22)$$

respectively. By taking the time derivative, the velocity of S_1 is

$$v_{s1} = -l_{s1} \dot{\varphi}_1 \sin \varphi_1 \vec{e}_x + l_{s1} \dot{\varphi}_1 \cos \varphi_1 \vec{e}_y \quad (2.23)$$

and the velocity of S_2 is

$$v_{s2} = [-l_1 \dot{\varphi}_1 \sin \varphi_1 - l_{s2} (\dot{\varphi}_1 + \dot{\varphi}_2) \sin(\varphi_1 + \varphi_2)] \vec{e}_x + [l_1 \dot{\varphi}_1 \cos \varphi_1 + l_{s2} (\dot{\varphi}_1 + \dot{\varphi}_2) \cos(\varphi_1 + \varphi_2)] \vec{e}_y. \quad (2.24)$$

Therefore, the squares of v_{s1}

$$v_{s1}^2 = (l_{s1} \dot{\varphi}_1)^2 \quad (2.25)$$

and v_{s2}

$$v_{s2}^2 = (l_1 \dot{\varphi}_1)^2 + (l_{s2} (\dot{\varphi}_1 + \dot{\varphi}_2))^2 + 2l_1 l_{s2} \dot{\varphi}_1 (\dot{\varphi}_1 + \dot{\varphi}_2) \cos \varphi_2 \quad (2.26)$$

are known, hence the Lagrange function \mathcal{L} is defined properly.

Following the Lagrange formalism, the sum of all non-conservative, generalized force (or

torque), acting on link 1

$$\tau_1 = \frac{d}{dt} \left(\frac{\partial \mathcal{L}}{\partial \dot{\varphi}_1} \right) - \frac{\partial \mathcal{L}}{\partial \varphi_1}, \quad (2.27)$$

is equal to the partial derivatives of the energy representing the Lagrange function, with respect to the generalized velocity $\dot{\varphi}_1$

$$\begin{aligned} \frac{\partial \mathcal{L}}{\partial \dot{\varphi}_1} = & \Theta_1^{(S1)} \dot{\varphi}_1 + m_1 l_{s1}^2 \dot{\varphi}_1 + \Theta_2^{(S2)} (\dot{\varphi}_1 + \dot{\varphi}_2) + m_2 \left[l_1^2 \dot{\varphi}_1 + l_{s2} (\dot{\varphi}_1 + \dot{\varphi}_2) \right. \\ & \left. + l_1 l_{s2} (\dot{\varphi}_1 + \dot{\varphi}_2) \cos \varphi_2 l_1 l_{s2} \dot{\varphi}_1 \cos \varphi_2 \right], \end{aligned} \quad (2.28)$$

respectively its time derivative

$$\begin{aligned} \frac{d}{dt} \left(\frac{\partial \mathcal{L}}{\partial \dot{\varphi}_1} \right) = & \Theta_1^{(S1)} \ddot{\varphi}_1 + m_1 l_{s1}^2 \ddot{\varphi}_1 + \Theta_2^{(S2)} (\ddot{\varphi}_1 + \ddot{\varphi}_2) + m_2 \left[l_1^2 \ddot{\varphi}_1 + l_{s2}^2 (\ddot{\varphi}_1 + \ddot{\varphi}_2) \right. \\ & + l_1 l_{s2} (\ddot{\varphi}_1 + \ddot{\varphi}_2) \cos \varphi_2 - l_1 l_2 \dot{\varphi}_2 (\dot{\varphi}_1 + \dot{\varphi}_2) \sin \varphi_2 \\ & \left. + l_1 l_{s2} \ddot{\varphi}_1 \cos \varphi_2 - l_1 l_{s2} \dot{\varphi}_1 \dot{\varphi}_2 \sin \varphi_2 \right] \end{aligned} \quad (2.29)$$

and the derivative of the Lagrange function with respect to the generalized coordinate φ_1

$$\frac{\partial \mathcal{L}}{\partial \varphi_1} = 0. \quad (2.30)$$

In accordance to link 1, the sum of generalized forces acting on link 2

$$\tau_2 = \frac{d}{dt} \left(\frac{\partial \mathcal{L}}{\partial \dot{\varphi}_2} \right) - \frac{\partial \mathcal{L}}{\partial \varphi_2} \quad (2.31)$$

is equal to the partial derivatives of the Lagrange function with respect to the generalized velocity $\dot{\varphi}_2$

$$\frac{\partial \mathcal{L}}{\partial \dot{\varphi}_2} = \Theta_2^{(S2)} (\dot{\varphi}_1 + \dot{\varphi}_2) + m_2 l_{s2}^2 (\dot{\varphi}_1 + \dot{\varphi}_2) + m_2 l_1 l_{s2} \dot{\varphi}_1 \cos \varphi_2, \quad (2.32)$$

respectively its time-derivative

$$\frac{d}{dt} \left(\frac{\partial \mathcal{L}}{\partial \dot{\varphi}_2} \right) = \Theta_2^{(S2)} (\ddot{\varphi}_1 + \ddot{\varphi}_2) + m_2 l_{s2}^2 (\ddot{\varphi}_1 + \ddot{\varphi}_2) + m_2 l_1 l_{s2} \ddot{\varphi}_1 \cos \varphi_2 - m_2 l_1 l_{s2} \dot{\varphi}_1 \dot{\varphi}_2 \sin \varphi_2, \quad (2.33)$$

and the derivative of the Lagrange function with respect to the generalized coordinate φ_2

$$\frac{\partial \mathcal{L}}{\partial \varphi_2} = -m_2 l_1 l_{s2} \dot{\varphi}_1 (\dot{\varphi}_1 + \dot{\varphi}_2) \sin \varphi_2. \quad (2.34)$$

Finally, the mass matrix is

$$M(\varphi) = \begin{pmatrix} \Theta_1^{(S1)} + \Theta_2^{(S2)} + m_1 l_{s1}^2 + m_2 (l_1^2 + l_{s2}^2 + 2l_1 l_{s2} \cos \varphi_2) & \Theta_2^{(S2)} + m_2 (l_{s2}^2 + l_1 l_{s2} \cos \varphi_2) \\ \Theta_2^{(S2)} + m_2 (l_{s2}^2 + l_1 l_{s2} \cos \varphi_2) & \Theta_2^{(S2)} + m_2 l_{s2}^2 \end{pmatrix} \quad (2.35)$$

and the centrifugal vector is determined as

$$h(\varphi, \dot{\varphi}) = \begin{pmatrix} -m_2 l_1 l_{s1} \sin \varphi_2 [\dot{\varphi}_2 (\dot{\varphi}_1 + \dot{\varphi}_2) + \dot{\varphi}_1 \dot{\varphi}_2] \\ m_2 l_1 l_{s1} \dot{\varphi}_1^2 \sin \varphi_2 \end{pmatrix}. \quad (2.36)$$

Thus, a model describing a 2 DOF is now available and will be used for a position controller design in Chapter 6.

3. Modeling of Pneumatic Muscle Actuators (PMAs)

3.1. Introduction

PMAs are very commonly used actuators. Because of their advantageous attributes, like passive compliance and a high power-to-weight ratio, it is desirable to drive robots with PMAs, especially if they share a work space or are in close contact with human users. Since robotic systems are always driven by forces, respectively torques, finding an exact model that describes the PMA force is of high interest.

Several investigations of PMAs have shown that the PMA force can be subdivided into a static and a dynamic force component. The latter component is constituted by hysteresis [46, 9] and some thermodynamic effects [5, 6], and it acts like a damper on the PMA-driven system [40], i.e. energy is dissipated from the system. Although measuring and compensating the dynamic force of PMAs is possible, the effort to do so is very high, and the improvements are hardly significant [64, 9, 5]. This is due to the fact that the static component dominates the PMA force. This statement gets emphasized by the excellent control results presented in [35, 36, 7, 62, 52], which were achieved only by modeling the PMA by its static force. Due to this, the main focus is placed on the static PMA force in this thesis. The latest findings in modeling the hysteresis of PMAs are discussed briefly in Sec. 3.4.2, while the influence of thermodynamic effects is generally treated as disturbance. Additionally, as it is one of the trending topics in robot actuation [74], the PMA is examined for its variable stiffness at the end of this chapter in Sec. 3.6.

Although it is not clear who developed the first PMA, the first scientific results on the physical behavior of PMAs were published by Schulte [65], who studied its physical behavior. The first approach for modeling the static PMA force was introduced by Chou and Hannaford [23]. Their approach is likely the most popular one for modeling the static force characteristic of a PMA; however, it is important to say that this model was created for a *McKibben* PMA. Nowadays, the majority of PMA-driven robots is driven by *Festo* PMAs, and their structure – and also their physical behavior – slightly differs from *McKibben* PMAs. While *McKibben* PMAs are mostly self-made, *Festo* produces PMAs according to industrial standards, regarding e.g. high resistance. A long life period, and a comparability of PMAs of the same type are guaranteed.

The *McKibben* PMA consists of an internal bladder surrounded by a braided mesh shell.

While the inner bladder incloses the air, the mesh consists of flexible but non-extensible threads and keeps the bladder from exploding. In contrast to the Festo PMA, the inner bladder and the outer mesh shell are not connected, but lying loosely above each other. This is different for Festo PMAs, where the inner rubber encloses the fiber mesh, i.e. both layers are combined to one layer, called the PMA membrane. Both PMA types can be seen in Fig. 3.1.



Figure 3.1.: McKibben-like PMA in the foreground and a Festo PMA in the background

In Boblan [17], it is demonstrated by measurements that the model presented by Chou and Hannaford [23] loses its validity for Festo PMAs. To overcome this problem, modified versions with improved accuracy for Festo PMAs can be found e.g. in Sárosi et al. [61] or Andrikopoulos et al. [5].

Another approach for the specific use on Festo PMAs has been presented in Hildebrandt et al. [36]. The basic idea is the approximation of a Festo PMA as a piston with a virtual, pressure-dependent piston area and a spring that counteracts the expansion. A different approach for the specific use on Festo PMAs is presented in Wickramatunge and Leephakpreeda [79], where the static force characteristic is assumed to be well described by a mechanical spring with variable stiffness.

All models are motivated physically and can be adapted to the "true" physical behavior of a PMA by adjusting a set of freely tunable parameters. These parameters can be identified by optimization, as will be further explained in Sec. 3.3.5.

The "true" PMA force can be measured in two different ways, denoted as the *isometric* or *isobaric force measurement*. Although the measured force can vary significantly in dependency of the chosen measurement setup [54], no consensus about a superior measurement setup can be found in literature. Due to this, the PMA force is measured in an isometric, respectively an isobaric setup in Section 3.2 and compared afterwards. In Section 3.3.1, the geometric characteristics according to [23] of a PMA will be

discussed briefly. Especially the geometric constraints, defined by the PMA membrane, are fundamental for understanding PMAs correctly. After explaining existing models that describe the static PMA force in Section 3.3.2, a new approach, first presented in [48], will be shown in Section 3.3.3. The accuracy of this model can be further improved by a non-physically motivated extension discussed in Section 3.3.4.

In addition, a methodology for adapting all presented models to a measured PMA force map will be explained in Section 3.3.5. All models are identified with the same method. This facilitates the comparison of their accuracy, which is presented in Section 3.3.6.

After giving a brief discussion of the PMA hysteresis in Section 3.4, the PMA is investigated with respect to its mechanical attributes, like stiffness and damping, in Section 3.6. It will be shown that PMAs are actuators with variable stiffness.

Parts of the following chapter were previously published by the author in

M. Martens and I. Boblan. Modeling the static force of a festo pneumatic muscle actuator: A new approach and a comparison to existing models. *Actuators*, 6(4.33), 2017.

3.2. Experimental Force Determination

The major goal of this chapter is defined by the determination of a model describing the PMA force in the most precise way possible. It is clear that the quality and validity of the model crucially depends on the quality and validity of the measured PMA force because it represents the "true" force, and any model is referencing to this measurement.

The PMA force can be measured in two different ways [17]: the *isometric force measurement* [36, 54], i.e. the length of the PMA is kept constant while the pressure is varied, or the *isobaric force measurement* [23, 24, 71, 54, 79, 80], i.e. the pressure is kept constant and the PMA length is varied. Although some publications, e.g. Minh et al. [54], are showing that the measured force map can vary significantly in dependency of the chosen measurement setup, no consensus about a superior measurement setup can be found in literature. Due to this, the PMA force will be measured in both an isometric and an isobaric measurement setup and the results will be compared afterwards. In contradiction to most existing publications, it will be shown that the dependency of the chosen measurement setup is hardly significant.

3.2.1. Isometric Measurement

Measuring the PMA force in an isometric way means that the length is kept constant and the pressure is varied while the exerted force is recorded by a force sensor. In this section, the force map of a Festo *DMSP-20-300* and a *DMSP-20-353* are each measured. The test rig that is used for all isometric measurements is depicted in Fig. 3.2.



Figure 3.2.: Photo of the test rig that is used to measure the characteristic force maps.

The *isometric* measurement procedure will be explained briefly. Before the procedure can be started, a set of pressure points has to be defined. For this thesis, this set is defined as $P_{\text{mset}} = \{0.1, 0.5, 1, 1.5, 2.5, 3, 3.5, 4, 4.5, 5, 5.5, 5.9\}$ bar. For each element of the set of starting pressures, the following is done:

- The PMA is pressurized with $p_i \in P_{\text{mset}}$, where $i \in [1, 12]$ denotes the index of the chosen element. Due to its internal pressure the unfastened PMA contracts in length.
- The fact that the PMA is unfastened, implies that the PMA force must be zero at p_i , i.e. no force is exerted.
- At this pressure-dependent initial length $L_0(p_i)$ the PMA is fastened with screws.
- While the PMA is fastened, the pressure is increased until it reaches the maximum pressure in $\max(P_{\text{mset}})$.
- By increasing the pressure towards the maximum pressure, the PMA pulls harder and the force is measured at every pressure $p \in P_{\text{mset}}$ with $p \geq p_i$.

The full PMA force map is now recorded from low to high pressure. The counteract measurement errors the force map is recorded again from high to low pressure. More precisely, the start pressure at which the PMA is fastened is decreasing, but once the PMA is fastened, the force is being recorded while increasing the pressure until it reaches the maximum pressure.

As a result of an isometric measurement, the force map of a Festo DMSP-20-300 is depicted in Fig. 3.3.

Fig. 3.3 demonstrates that depending on if the PMA gets stretched or contracts, the exerted force is somewhere within a force range (blue area). While stretching the PMA from full contraction 0.22 m back to initial length 0.3 m, the force is on the upper blue solid line. While releasing the PMA, it will move back to full contraction. In doing this, the PMA force will follow the lower blue dashed line. For any other sequence

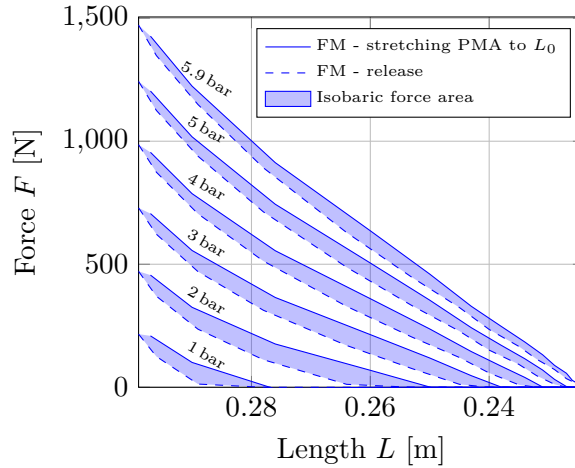


Figure 3.3.: Force of a Festo DMSP-20-300 measured isometrically for different pressures

of stretching and releasing the PMA, the exerted force will be somewhere within the blue area and depends on the contraction direction. This phenomenon is known as the *hysteresis* of the PMA. It should be noted that the blue area represents the integral of the PMA force along a closed path and – since the force for releasing is lower than for stretching – this is always negative, i.e. energy gets dissipated. In other words, the PMA behaves like a mechanical damper.

3.2.2. Isobaric Measurement

Measuring the PMA force map isobarically means that the inner pressure is kept constant by a controller while the PMA length is varied. Because the PMA maximum force can be very high, e.g. about 1.5 kN for a DMSP-20-XXX, different actuators have been used to put the PMA to the test in measurement setups of other researchers. While Lin et al. [46] were using a stronger PMA for stretching the PMA in the test, Schindele and Aschemann [64] were using a hydraulic cylinder instead. The test rig for all isobaric force measurements of this thesis is depicted in Fig. 3.4. In contrast to other measurement setups, in the present measurement setup the PMA length is not measured directly but calculated from the measured angle, multiplied with the pulley radius. Furthermore, the relationship of the levers is designed so that stretching the PMA by hand becomes possible.

The isobaric measurement procedure is explained briefly:

- Before the procedure can be started, a set of pressure points has to be defined. For this thesis, this set is defined as $P_{\text{mset}} = \{0.1, 0.5, 1, 1.5, 2.5, 3, 3.5, 4, 4.5, 5, 5.5, 5.9\}$ bar.
- The pressure is set to $\max(P_{\text{mset}}) = 5.9$ bar and the lever arm is rotated until the

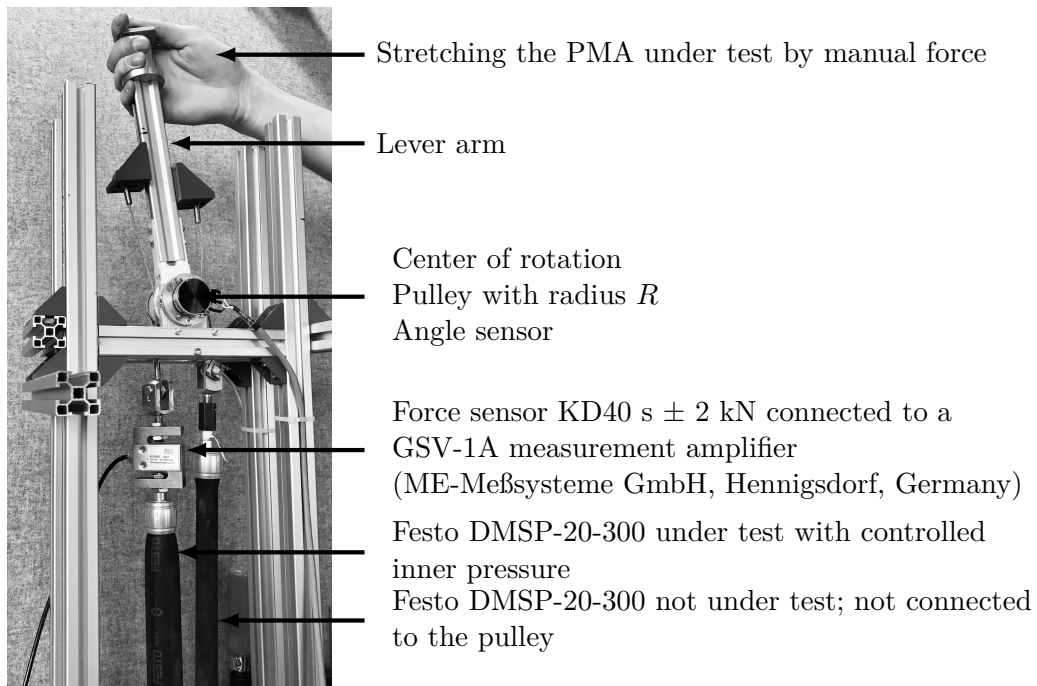


Figure 3.4.: Photo of the test rig for an isobaric measurement of the PMA force map.

rope is tight but the measured force is still zero. This position represents the start position for the following measurement.

- Stretching the PMA back to its initial length L_0 defines the end position.
- The PMA is moved by hand from start to end position for every $p \in P_{\text{mset}}$, while the pressure is varied from high to low. The force is recorded continuously for all pressures.

From the raw measurement data, one force map for stretching and one for contraction can be extracted, respectively. In accordance with Fig. 3.3, Fig. 3.5 shows the PMA force for stretching the fully contracted PMA back to its initial length L_0 (black solid line). For the opposite direction, the PMA contracts (black dashed line) at different exemplary pressures $p \in P_{\text{mset}}$. The enclosed gray area represents the energy that dissipates from the system within one closed cycle of fully stretching and releasing, i.e. the *hysteresis* of the PMA.

3.2.3. Comparing the Measurement Data

While the previous sections are showing how the PMA force map can be measured in two different setups, the results of both measurements (see Fig. 3.3 and 3.5) will be compared in this section. In Fig. 3.6 both measurements are plotted into one graph.

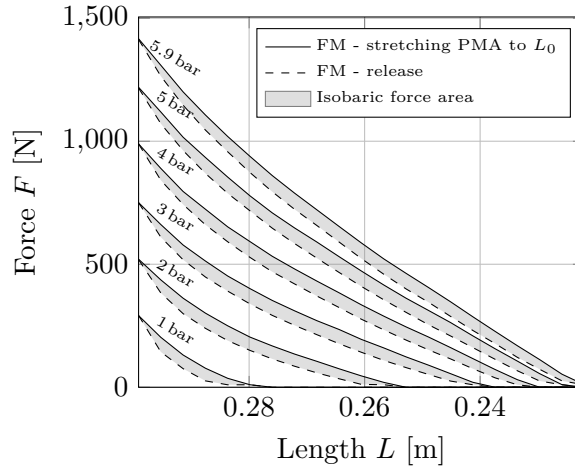


Figure 3.5.: Force map of a Festo DMSP-20-300 measured isobarically

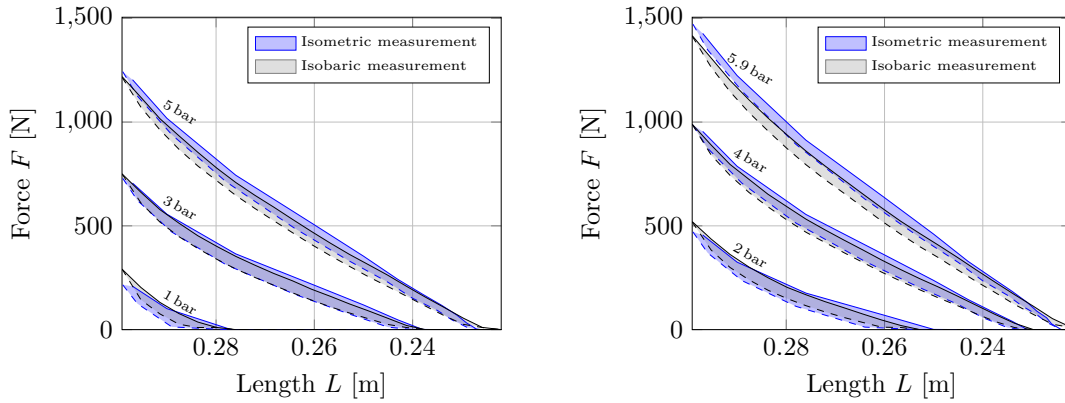


Figure 3.6.: Force of a Festo DMSP-20-300 measured isometrically (blue) and isobarically (black), respectively, for different pressures

The blue curves are representing the isometric, and the black curves the isobaric measurements of the PMA force map. It is striking that the measured data is almost independent of the chosen measurement setup and only minor differences are visible. Especially at the pressures close to the center of P_{mset} , the measured force is almost the same for both measurements. This statement is contradictory to the measurement data that can be found in Minh et al. [54], where the measured data is rather dependent on the measurement setup. However, it seems reasonable that the PMA force is unique and a dependency of the chosen measurement setup is not likely. On the other hand, a perfectly matching measurement is also unlikely because every measurement setup has its drawbacks, i.e. that the "true" force map gets disturbed individually. For this thesis, the isobaric measured force map is used for all following investigations and applications, as this measurement setup is closer to the robotic systems with which the PMAs will be

integrated in Chapter 5 and 6. Nevertheless, using the isometric measured data could be advantageous for other applications.

3.3. Modeling the Static Force

A PMA is mainly characterized by its static force map. The force map itself defines the static force that the PMA exerts for any combination of PMA length and pressure. In addition, the PMA exerts a hysteresis force that overlaps the static force, as can be seen in Fig. 3.3 and 3.5. Due to this, the PMA force is not a single value, but somewhere between a lower and upper force limit. The static force map can be extracted from Fig. 3.3 and 3.5 as the mean value of an upper and lower force limit, which is marked as a solid or dashed line. The resulting force map for a DMSP-20-300 can be seen in Fig. 3.7.

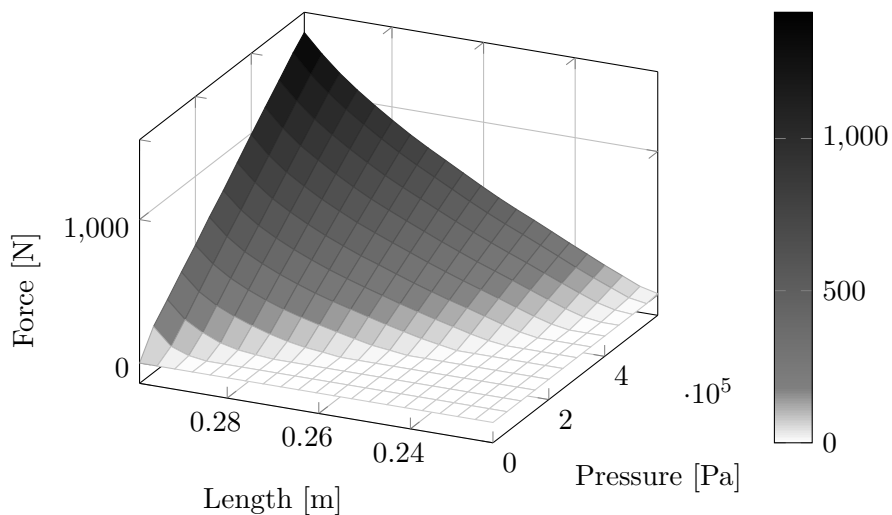


Figure 3.7.: Measured force map of a Festo DMSP-20-300

The static force of a PMA is a function of its length and pressure. As can be seen in Fig. 3.7, the maximum PMA force varies significantly with its length. While the maximum force can only be exerted at initial length, no force can be exerted anymore while the PMA is fully contracted. The curved edge in Fig. 3.7 is the *line of zero force* and separates the areas of pulling, distinguished by positive force values, and – only theoretically – the area of pushing, which is uniformly 0 N.

Before the static PMA force will be approximated by different models, it is important to understand the geometric characteristics of the PMA, which will be explained in Section 3.3.1. The different models – and a methodology of adapting these models to a specific PMA – will be explained afterwards in Section 3.3.2, 3.3.3, 3.3.4, and 3.3.5.

3.3.1. Geometric Characteristics

Following the ideas of [23, 17, 72], the PMA volume can be approximated by a cylinder. The volume

$$V(L,D) = \frac{\pi}{4}D^2L \quad (3.1)$$

of a cylinder is a function of its length L and diameter D . Cutting the PMA membrane open and flattening it to a plane (Fig. 3.8), the dependency of the PMA diameter on its length is defined by Pythagoras theorem [23]. Assuming that the length L_{Fiber} of the fibers, the braided mesh is made of (see Fig. 3.8), stays constant, the diameter equation holds

$$D(L) = \frac{\sqrt{L_{\text{Fiber}}^2 - L^2}}{n\pi}, \quad (3.2)$$

whereby

$$L_{\text{Fiber}} = \frac{L_0}{\cos \theta_0} \quad \text{and} \quad n = \frac{L_0 \tan \theta_0}{\pi D_0}. \quad (3.3)$$

The factor n denotes the number of windings, i.e. it defines how often each fiber circles the PMA bladder on its way from one end to the other (see Fig. 3.8). The index 0 indicates the initial state of the PMA, with atmospheric pressure p_0 , initial length L_0 , inner diameter D_0 , membrane thickness H_0 , and fiber angle θ_0 . In [17], it is demonstrated by measurements that the initial fiber angle is $\theta_0 = 28.6^\circ$. This is the only value that can be found in literature, but whether or not this value is correct will be checked in Section 3.3.5.

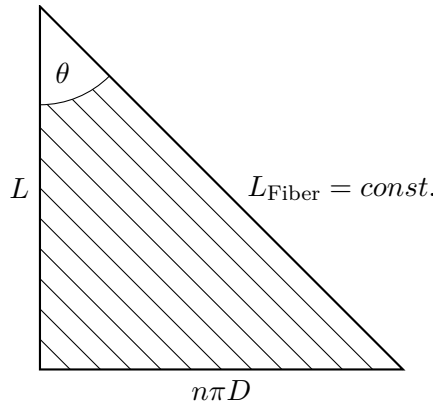


Figure 3.8.: Unreeled membrane of a Festo PMA

Inserting the functional dependency on the diameter back into the approximated volume (3.1), the PMA volume

$$V(L) = \frac{L \cdot L_{\text{Fiber}}^2}{4\pi n^2} - \frac{L^3}{4\pi n^2}. \quad (3.4)$$

loses its dependency on the diameter and is only a function of the PMA length.

3.3.2. Existing Static Force Models

PMAs are mainly defined by their static force map, and many different models can be found in literature. While all models are physically motivated, their accuracy differs significantly, as it will be shown later in this chapter. The first model

$$F_{\text{MK}}(p, L) = -p \cdot \frac{\partial V}{\partial L} = p \cdot \frac{L_{\text{Fiber}}^2 (3 \cos^2 \theta - 1)}{4\pi n^2}, \quad (3.5)$$

actually introduced to describe a McKibben Muscle by Schulte [65], is only based on the energy that is needed to change the inner PMA air volume. Thereby and for the following PMA force models, p denotes the PMA pressure, V its volume, L its length, and θ its fiber angle. Furthermore, the fiber length L_{Fiber} and the number of fiber windings n are constant. Effects of membrane elasticity are fully neglected. As demonstrated in [17], the remaining error between the measured static force characteristic of a Festo PMA and (3.5) is not negligible. The reason for this is that the Festo PMA, in contrast to the McKibben PMA, seems to store potential energy in its deformed membrane.

A modified version of (3.5)

$$F_{\text{Andri}}(p, L) = p \cdot c_0 \cdot \frac{\pi D_0^2}{4} \left[\frac{3}{\tan^2 \theta_0} \left(1 - c_1 \cdot \frac{L_0 - L}{L_0} \right)^2 - \frac{1}{\sin^2 \theta_0} \right] \quad (3.6)$$

was presented in [5, 6], where (3.5) is extended by two additional factors c_0 and c_1 . Although the parameters c_0 and c_1 were calculated directly in [5, 6], in this thesis, both parameters will be identified by solving an optimization problem.

Another model variant

$$F_{\text{Saro}}(p, L) = (c_0 \cdot p + c_1) e^{\frac{c_2 \cdot (L_0 - L)}{L_0}} + p \cdot \left(d_0 \cdot \frac{L_0 - L}{L_0} + d_1 \right) + d_2 \quad (3.7)$$

is presented by Sárosi et al. [61]. This model is also inspired by (3.5) and can be seen as a modification of the model introduced by Chou and Hannaford [23]. In accordance with the model presented by Andrikopoulos et al. [5], the accuracy of (3.7) can be adjusted by a set of tunable parameters.

A model for the specific use on a Festo PMAs is presented in [36]. This model

$$F_{\text{Hilde}}(p, L) = p \cdot A(L) - F_c(L) = p \cdot \sum_{j=0}^2 c_j L^j - \left(\sum_{j=0}^3 d_j L^j + d_4 L^{2/3} \right) \quad (3.8)$$

is a combination of the pressure-virtual-piston-area product $p \cdot A(L)$ and a length-dependent counter force $F_c(L)$. The underlying idea is that the PMA behaves like a combination of a pneumatic piston with a variable piston area and a mechanical spring that counteracts the expansion of the PMA.

In [79], the static force characteristic of a Festo PMA

$$F_{\text{Wick}}(p,L) = \underbrace{(c_3 p^2 + c_2 p \Delta L + c_1 \Delta L^2 + c_0)}_{=k(p,\Delta L)} \cdot \Delta L \quad , \quad \text{with} \quad \Delta L = L - \min(L) \quad (3.9)$$

is assumed to be equivalent to a mechanical spring, with a displacement-pressure-dependent spring stiffness $k(p,\Delta L)$.

3.3.3. A New Approach for Modeling the Static Force

PMAs are a combination of a flexible tube and two stiff aluminium connectors (see Figure 3.1). The membrane that the tube is made of is a combination of a stiff aramid fiber mesh and a flexible rubber that incloses the air inside the PMA. While putting pressure inside the PMA, the membrane expands and, due to the stiff aramid fibers, the PMA gets shorter. According to [23], the approach for the presented PMA model is that the fiber length L_{Fiber} stays constant and, therefore, only the membrane rubber deforms.

While pulling a contracted PMA, the muscle reacts with a force F_{PMA} opposite to the pulling direction. The virtual work of the PMA W_{PMA} is given through

$$W_{\text{PMA}} = -F_{\text{PMA}} \cdot dL. \quad (3.10)$$

Furthermore, the virtual work of the PMA can be subdivided. On the one hand, the virtual work

$$W_v = p \cdot dV \quad (3.11)$$

has to be done to change the included air volume. On the other hand, additional virtual work W_m is necessary to change the potential energy of the elastic membrane rubber [17], so that the total amount of virtual work can be summarized as

$$W_{\text{PMA}} = W_v + W_m. \quad (3.12)$$

While putting pressure inside the PMA, the actuator gets shorter and expands in diameter. The deformation of the membrane is a plane state strain and can be described as the strain in the direction of the PMA length ε_L and the PMA perimeter ε_{pe} . Rotating the coordinate system by the membrane fiber angle θ , the deformation is given by the strain in the mesh fiber direction ε_f and the direction of pure rubber ε_{ru} perpendicular to the fiber direction (see Figure 3.9). Following the approach of a constant fiber length, the strain ε_f is always zero. This means that the PMA membrane

only expands perpendicularly to the fibers. For this thesis, a one-dimensional state of stress is assumed, and therefore, according to Hooke's law, the tension inside the rubber σ_{ru} will be approximated by

$$\sigma_{\text{ru}} = E_{\text{ru}}(L) \cdot \varepsilon_{\text{ru}}, \quad (3.13)$$

where the modulus of elasticity is supposed to be a function of the PMA length.

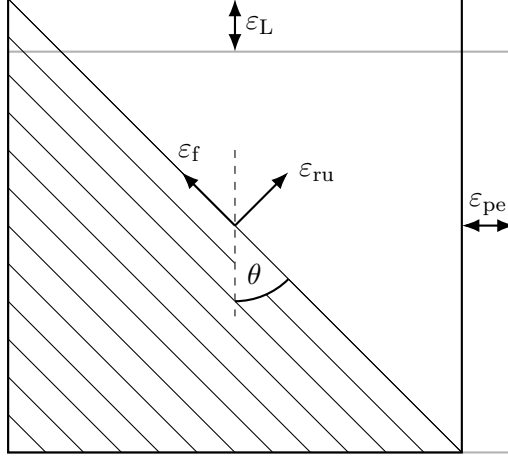


Figure 3.9.: Schematic of the PMA membrane and the fiber angle.

Following the approach of a one-dimensional membrane deformation, the strain

$$\varepsilon_{\text{ru}} = \sqrt{(\varepsilon_{\text{L}})^2 + (\varepsilon_{\text{pe}})^2} = \sqrt{\left(\frac{L - L_0}{L_0}\right)^2 + \left(\frac{D - D_0}{D_0}\right)^2} \quad (3.14)$$

is given by the theorem of Pythagoras. Rotating the tension σ_{ru} back to initial coordinates, it is possible to calculate the tension in the length direction as

$$\sigma_{\text{L}} = \sigma_{\text{ru}} \cdot \sin \theta = E_{\text{ru}}(L) \cdot \varepsilon_{\text{ru}} \cdot \sin \theta = E_{\text{ru}}(L) \cdot \varepsilon_{\text{L}} \quad (3.15)$$

and the tension in the perimeter direction of the PMA as

$$\sigma_{\text{pe}} = \sigma_{\text{ru}} \cdot \cos \theta = E_{\text{ru}}(L) \cdot \varepsilon_{\text{ru}} \cdot \cos \theta = E_{\text{ru}}(L) \cdot \varepsilon_{\text{pe}}. \quad (3.16)$$

Multiplying the tension with the edge surfaces of the unreel membrane, the virtual work to deform the membrane in the length direction is given through

$$W_{\text{Elast-L}} = \pi \cdot H_0 \cdot D \cdot \sigma_{\text{L}} \cdot dL = \pi \cdot H_0 \cdot D \cdot E_{\text{ru}}(L) \cdot \varepsilon_{\text{L}} \cdot dL. \quad (3.17)$$

This approach neglects any effect of lateral contraction. The initial membrane thickness, H_0 , can easily be calculated from the given initial inner diameter D_0 and the measurable

outer initial diameter of the PMA rubber tube. The virtual work necessary to deform the membrane in the perimeter direction can be calculated in an analog way [17]:

$$W_{\text{Elast-pe}} = -\pi \cdot H_0 \cdot L \cdot \sigma_{\text{pe}} \cdot dD = -\pi \cdot H_0 \cdot L \cdot E_{\text{ru}}(L) \cdot \varepsilon_{\text{pe}} \cdot dD. \quad (3.18)$$

The negative sign in (3.18) is necessary because an increase in length of the PMA has to result in a decreasing perimeter, and this is defined to be positive for this thesis. Inserting (3.10), (3.11), (3.17), and (3.18) in (3.12), the PMA force is given by

$$F_{\text{Mart}}(p,L) = F_{\text{PMA}}(p,L) = -p \cdot \frac{\partial V}{\partial L} + \pi \cdot H_0 \cdot E_{\text{ru}}(L) \left(L \cdot \varepsilon_{\text{pe}} \cdot \frac{\partial D}{\partial L} - D \cdot \varepsilon_{\text{L}} \right). \quad (3.19)$$

It must be noted that (3.19) is positive in case the PMA exerts a pulling force. The derivatives $\frac{\partial V}{\partial L}$ and $\frac{\partial D}{\partial L}$ can be found in Section A.1 in the appendix. As the modulus of elasticity of the membrane rubber and the fiber angle cannot be measured directly, both terms are identified by data-based optimization. The modulus of elasticity E_{ru}

$$E_{\text{ru}}(L) = c_3 L^3 + c_2 L^2 + c_1 L + c_0. \quad (3.20)$$

used in (3.15) and (3.16) is approximated by a polynomial of the third order with coefficients c_0 , c_1 , c_2 and c_3 . This order is chosen by experiment. It can be seen that higher-order polynomials do not lead to better results. However, for lower-order polynomials, the calculated error (3.25) defined later in this chapter is much higher. Furthermore, the approximately known fiber angle

$$\theta_0^* = \theta_0 + d_0 \quad (3.21)$$

is corrected by a constant d_0 . θ_0^* and is now used as the new, corrected fiber angle. Furthermore, all parameters c_j and d_j ($j \in \mathbb{N}_0$) have to be identified by solving a data-based optimization. The parameters c_j and d_j are calculated in such a way that the quadratic error between a measured force map and the forces predicted by the models is the smallest. A more detailed discussion of the optimization will be given later in Section 3.3.5.

3.3.4. An Extension of the New Approach

As will be demonstrated in the following sections, (3.19) approximates the static PMA quite well. Nevertheless, experimental testing revealed that the accuracy of (3.19) can be further improved by adding a linear pressure function. The force

$$F_{\text{MartExt}}(p, L) = -p \cdot \frac{\partial V}{\partial L} + \pi \cdot H_0 \cdot E_{\text{ru}}(L) \left(L \cdot \varepsilon_{\text{pe}} \cdot \frac{\partial D}{\partial L} - D \cdot \varepsilon_L \right) - \underbrace{\frac{L_0^2}{4\pi n^2 (\cos \theta_0)^2}}_{\text{Extension}} d_1 p + d_2 \quad (3.22)$$

has two additional free parameters d_1 and d_2 and will be denoted as the *extended static force model*. As already noted, the derivatives $\frac{\partial V}{\partial L}$ and $\frac{\partial D}{\partial L}$ can be found in Section A.1 in the appendix.

3.3.5. Methodology of Parameter Identification

All models presented in the previous sections have in common that they approximate the static force of a PMA. While all of them are physically motivated, not all parameters are measurable, i.e. they must be determined by comparison to a measured PMA force map. A methodology of the identification procedure applicable to all models was first presented in Martens and Boblan [48] and will be explained in this section.

According to the measurement procedure explained in Section 3.2.1 and 3.2.2, the static force maps of a Festo DMSP-10-250, DMSP-20-250, DMSP-20-300, and DMSP-20-353 are measured isometrically, and the force maps of a Festo DMSP-20-300 and DMSP-20-355 are recorded in an isobaric setup. Although the force maps from the isometric measurements are of interest for this chapter, only the force maps measured isobarically will be used within the following chapters. This is justified, as the robotic applications are closer to the isobaric measurement setup than to the isometric setup, i.e. the isobaric force maps are more representative for the applications of interest.

In the following, all presented PMA models (3.22), (3.19), (3.6), (3.7), (3.8), and (3.9) are identified by solving

$$\min \sum_{p_i} \sum_{L_j} (F_{\text{Measurement}}(p_i, L_j) - F_{\text{Model}}(p_i, L_j))^2 \quad (3.23)$$

$i = \text{Number of pressure points}$
 $j = \text{Number of length points,}$

so that the quadratic error between the measured force map and the force map calculated by the model gets minimized. The optimization is solved by using the MATLAB (R2015b, The MathWorks, Inc., Natick, MA, USA) function *fminsearch*. Because the optimization problem (3.23) is nonlinear, the minimum that is found by the algorithm might depend on the start point and might be a local minimum. The start point for all models is identified by iterative testing. It can be seen that good results – in the sense of a small error – can be achieved if the start points are chosen with respect to their physical meaning and within a proper range. According to the SI units – 1 m for lengths and 1 Pa = 1×10^{-5} bar for pressure –, any parameter c_j and d_j ($j \in \mathbb{N}_0$) is set to 1 if it

is only multiplied to a length-dependent factor, and to $1e-5$ if it is multiplied by the pressure. The modulus of elasticity of rubber, necessary for (3.19), is supposed to be in the area of 1 MPa, and therefore the chosen start point is set to 1×10^6 . The initial fiber angle θ_0 in the equation (3.19) is supposed to be correct. The chosen parameter estimation start points for all models are given without units in Tab. 3.2.

Table 3.2.: Start points of parameter estimation for all models without units.

	c_0	c_1	c_2	c_3	d_0	d_1	d_2	d_3	d_4
F_{Andri}	10^{-5}	10^{-5}	-	-	-	-	-	-	-
F_{Wick}	1	1	10^{-5}	10^{-10}	-	-	-	-	-
F_{Hilde}	10^{-5}	10^{-5}	10^{-5}	-	1	1	1	1	1
F_{Saro}	10^{-5}	1	1	-	10^{-5}	10^{-5}	1	-	-
F_{Mart}	10^6	10^6	10^6	10^6	0	-	-	-	-
F_{MartExt}	10^6	10^6	10^6	10^6	0	0	1	-	-

The estimated parameters are adapting the model to a specific, measured force map. The resulting parameters, adapting the models F_{Martens} and F_{MartExt} to the isobaric measured force maps of a Festo DMSP-20-300 and DMSP-20-355, can be seen in Tab. 3.3.

Table 3.3.: Estimated parameters for F_{Martens} and F_{MartExt} ; optimization start point is given in Table 3.2.

	F_{Mart}		F_{MartExt}	
	DMSP-20-300	DMSP-20-355	DMSP-20-300	DMSP-20-355
c_0 in MPa	329.07	318.0334	117.98	104.51
c_1 in MPa/m	-3562.65	-2922.75	-1102.56	-731.49
c_2 in MPa/m ²	13002.7	9061.85	3428.39	1601.6
c_3 in MPa/m ³	-15867.77	-9395.63	-3424.2	-942.75
d_0 in °	-3.07	-3.55	-3.51	-3.49
d_1	-	-	0.0825	0.0786
d_2 in N	-	-	53.76	123.28

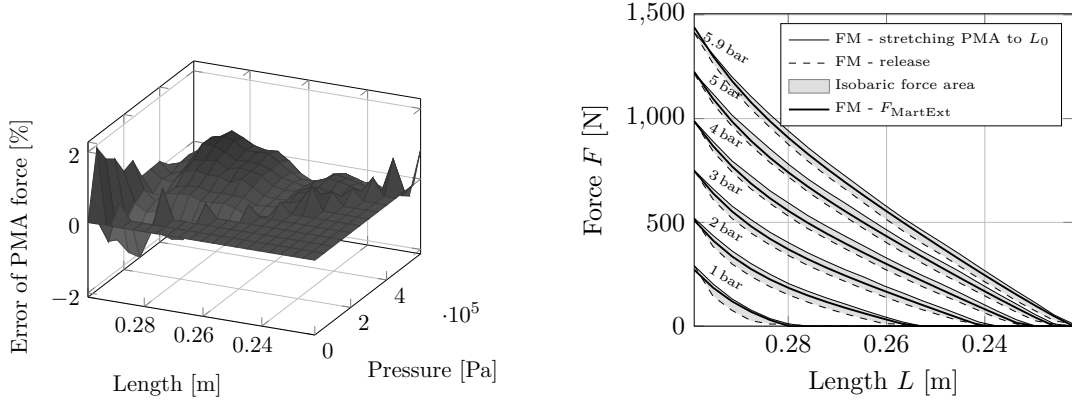
The error

$$\Delta F_{\%}(F_{\text{Measurement}}, F_{\text{Model}}) = 100 \cdot \frac{F_{\text{Measurement}} - F_{\text{Model}}}{\max(|F_{\text{Measurement}}|)} \quad (3.24)$$

is defined as the difference between a measured and a calculated force map, normalized to the absolute maximum measured force. Multiplied by 100, the error is given in percentage and is shown in Fig. 3.10a.

By minimizing the quadratic error according to (3.23), the parameters c_j and d_j ($j \in \mathbb{N}_0$) are estimated in an optimal manner, i.e. the most suitable approximation of the measurement data is found. As a result, the identified model F_{MartExt} lies right between the upper isobaric lines – force map measured for decreasing contraction – and

the lower isobaric line – force map for increasing contraction –, represented as a thick, solid line in Fig. 3.10b.



(a) Force error of a Festo DMSP-20-300 in % between measured force map and its approximation through the identified model F_{MartExt} (3.22)

(b) Isobaric measured force map and approximation by the identified model F_{MartExt} (3.22) of a Festo DMSP-20-300

Figure 3.10.: Isobaric measured force map of a Festo DMSP-20-300 and its approximation

3.3.6. A Comparison of Accuracy

Since the error defined by (3.24) can be either positive or negative, a worst case estimation of the error is given as

$$\overline{\Delta F_{\%}} = \max(\Delta F_{\%}, |\min(\Delta F_{\%})|). \quad (3.25)$$

This value is calculated for all models presented in the previous Sections 3.3.2 and 3.3.3. The results can be seen in Tab. 3.4 for both the isometric and the isobaric measured force maps and different models, respectively.

While all models, besides the model for McKibben PMAs F_{MK} (3.5), are suitable to approximate the Festo PMA static force behavior, their accuracy differs significantly. Tab. 3.4 shows that the most accurate approximation can be reached mostly by adapting the new extended approach (3.22) to a measured force map by solving the optimization problem (3.23). Due to this, the extended approach (3.22) from Section 3.3.4 will be used as a representation of the static PMA force for the rest of this thesis. However, for some measurements, other models like (3.19) or (3.7) are superior.

Table 3.4.: Maximum force error (3.25) of each model by percentage.

$\overline{\Delta F\%}$ of	F_{MK}	F_{Andri}	F_{Wick}	F_{Hilde}	F_{Saro}	F_{Mart}	F_{MartExt}
isometric							
DMSP-10-250	51.16%	21.03%	11.68%	10.81%	8.01%	7.96%	7.38%
DMSP-20-250	31.64%	14.05%	9.45%	5.42%	4.43%	3.63%	3.32%
DMSP-20-300	34.1%	14.73%	9.2%	7%	6.87%	3.11%	3.54%
DMSP-20-353	30.94%	16.03%	9.95%	7.8%	7.42%	4.88%	4.68%
isobaric							
DMSP-20-300	31.35%	11.21%	8.12%	8.31%	6.37%	5.02%	1.92%
DMSP-20-353	36.12%	11.52%	9.18%	8.88%	1.89%	10.32%	2.24%

3.4. Modeling the PMA Hysteresis

As can be seen in Fig. 3.3, 3.5, and 3.10b, the PMA force is a superposition of a static force and a second force that changes according to its own dynamic behavior, denoted as *hysteresis*. This phenomenon was already described in the first publications about PMAs, e.g. by Chou and Hannaford [23][24]. As a result of the hysteresis, the PMA force is not unique for any pair of pressure and length, but lies somewhere within a force range around the static force. Although it is not proven yet, it seems to be very plausible that the hysteresis occurs due to friction between the fibers and the rubber that the membrane is made of. The PMA hysteresis has its own dynamic behavior and can be modeled with e.g. the Maxwell-Slip [54, 76], the Bouc-Wen [64], or the Prandtl–Ishlinskii model [46]. In Aschemann and Schindele [9], all of these models are compared to each other and included into a feed-forward hysteresis compensation. It is shown that both the error between the measured and the predicted PMA force on the one hand and the controller positioning performance on the other hand can be improved by taking hysteresis into account but are almost independent of the chosen modeling approach.

The identification of the Bouc-Wen model – suitable to model dynamic hysteresis – goes along with a very complex and expensive test setup because the PMA length must be varied dynamically with different velocities. For this thesis, it will be supposed that the PMA velocity – the time derivative of the PMA length – is sufficiently small, i.e. the hysteresis can be modeled quasi-statically. Both the Prandtl–Ishlinskii and the Maxwell-Slip model [54, 76] are quasi-static representations of static hysteresis. These models only depend on the sign of the PMA velocity and not on its absolute value. Due to this, the identification process can be done offline with data measured statically or quasi-statically, as done in Section 3.2.1 and 3.2.2. While the Prandtl–Ishlinskii model [46] uses a superposition of play-operators and is hard to interpret physically, the Maxwell-Slip model [54, 76] approximates the hysteresis with a superposition of

friction elements and gives a deeper understanding of the hysteresis. This makes the Maxwell-Slip model the best choice for modeling the hysteresis in accordance with the measured data in the previous sections.

3.4.1. The Maxwell-Slip Model

Following the idea of the Maxwell-Slip model, the hysteresis force

$$F_{\text{Hyst}}(k) = \sum_{i=1}^n k_{\text{MS},i} \delta_{\text{MS},i}(k) \quad (3.26)$$

can be approximated in the discrete time domain by a superposition of n so-called Maxwell-Slip elements, where the index k represents the discrete time step. Each element behaves like a "massless" mass with friction that is pulled by a spring with stiffness $k_{\text{MS},i}$. In relation to the k th time step, the spring deformation for the following time step

$$\delta_{\text{MS},i}(k+1) = \text{sign}(L(k+1) - L(k) + \delta_{\text{MS},i}(k)) \cdot \min(|L(k+1) - L(k) + \delta_{\text{MS},i}(k)|, \Delta_{\text{MS},i}) \quad (3.27)$$

depends on the position, i.e. the PMA length L and the maximum stretching length of the spring $\Delta_{\text{MS},i}$. The variable $\delta_{\text{MS},i}$ represents the state of the dynamical system (3.27), i.e. the spring deformation acts as the non-local memory. While the PMA contracts and releases, each Maxwell-Slip element behaves in the following way: Starting with an unstressed spring, the mass sticks to the ground due to its friction. By pulling the free end of the spring, its force increases until the mass starts to slide. The expansion of the spring where the mass starts to slide is $\Delta_{\text{MS},i}$. While the mass is sliding in one direction, the spring force remains constant. By pulling the mass in the opposite direction, the mass stops immediately and starts to slide again when the spring deformation reaches $-\Delta_{\text{MS},i}$.

3.4.2. Identifying a Specific PMA Hysteresis

The general formulation of the Maxwell-Slip model (3.26) can be adapted to a specific hysteresis behavior by defining the number of Maxwell-Slip elements n , the spring stiffness $k_{\text{MS},i}$, and the individual maximum stretching length $\Delta_{\text{MS},i}$ for every element. As can be seen in Fig. 3.10b, the static PMA force represents the mean line for every pressure. By subtracting the static force from the stretching respectively releasing curve, the shape of the hysteresis can be extracted. The result for an exemplary PMA, a Festo DMSP20-300, can be seen in Fig. 3.11a. In contrast to most hysteresis curves, the mean line is not monotonically increasing but constant zero.

Since a hysteresis compensation will be of interest in Section 5.6 and this particular system is driven by DMSP-20-300, the hysteresis is investigated with this particular

PMA, but it should be mentioned that the methodology is the same for every other PMA.

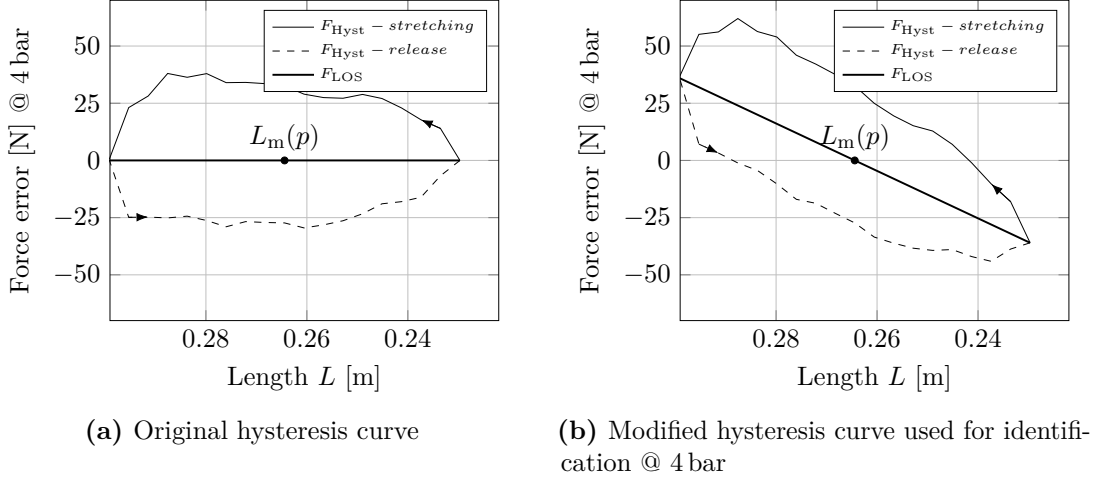


Figure 3.11.: Exemplary hysteresis curve of a Festo DMSP-20-300 measured @ 4 bar

From the data measured in Section 3.2.2, the hysteresis curve for any pressure $p \in P_{\text{mset}} = \{0.1, 0.5, 1, 1.5, 2.5, 3, 3.5, 4, 4.5, 5, 5.5, 5.9\}$ bar is given. In accordance with Vo-Minh et al. [76], the number of Maxwell-Slip elements is set to $n = 4$. The parameters $k_{\text{MS},i}$ and $\Delta_{\text{MS},i}$ can be identified by solving the optimization problem

$$\min_{k_{\text{MS}}, \Delta_{\text{MS}}} \left(100 \cdot \sum_{p_i} \sum_{L_j} \left(F_{\text{Hyst-Measurement}}(p_i, L_j, \dot{L}_j) + F_{\text{LOS}}(p_i, L_j) - F_{\text{Hyst}}(p_i, L_j, \dot{L}_j) \right)^2 \right) \quad (3.28)$$

$i = \text{Number of pressure points in } P_{\text{mset}}$
 $j = \text{Number of length points for } p_i,$

The results of the identification can be improved significantly by adding a monotonically increasing offset-force to the original hysteresis mean curve, as shown in Fig. 3.11b. The simplest monotonic increasing function is given by a first order polynomial, i.e.

$$F_{\text{LOS}}(p, L) = \underbrace{\frac{2 \cdot 40 \text{ N}}{\max(L_{\text{Measurement}}) - \min(L_{\text{Measurement}})}}_{=1.037 \frac{\text{N}}{\text{mm}} \text{ for a DMSP-20-300}} (L - L_{\text{m}}(p)) \quad (3.29)$$

is added to the original hysteresis curve for this section. The slope is chosen arbitrarily by experimental testing. Due to its modification, it is important to subtract the

Table 3.5.: Estimated parameters for the Maxwell-Slip hysteresis model for a Festo DMSP-20-300

$i =$	1	2	3	4
$k_{MS,i}$ in $\frac{N}{mm}$	6.19	1.55	0.88	0.00028
$\Delta_{MS,i}$ in mm	1.93	6.01	24.14	-59.54

artificial offset force F_{LOS} from the hysteresis force after its model-based prediction. The estimated parameters can be found in Tab. 3.5.

3.5. Quality of the PMA Force Model

After modeling the PMA static force and its hysteresis in the previous sections, for an exemplary Festo DMSP20-300 the quality of the force prediction by the estimated models will be of interest now. For validating the model-based force prediction, the PMA is pulled in an isobaric fashion again, as depicted in Fig. 3.4. The PMA force is measured with a force sensor and compared to the force prediction with only the static model and the static model with additional hysteresis, respectively. The results can be found for different exemplary pressures in Fig. 3.12.

During all measurements the pressurized PMA got stretched and released between different lengths. As can be seen e.g. at 4 bar, the circular area gets smaller the closer the points of switching between stretching and releasing are. Without hysteresis, Fig. 3.12 would only show lines, i.e. the PMA force would be independent of stretching and releasing. The existing gap between the force during the stretching and the releasing phase confirms the existence of the PMA hysteresis. The enclosed area represents the dissipation of energy from the mechanical system by the PMAs.

While the only static model (blue curve) has a maximum error of about 50 N, which is 3.33% of the maximum force of about 1500 N of a Festo DMSP-20-300, the static model with additional hysteresis (black curve) is closer to the true PMA force. The maximum force error of the static hysteresis model is about 25 N, i.e. the remaining error between predicted and measured force gets halved by taking hysteresis into account.

3.6. The PMA – An Actuator with Variable Stiffness?

In accordance with the previous sections, the PMA force can be subdivided into a static force and a force due to hysteresis. In summary, the force

$$F(p, L, \dot{L}) = F_{\text{static}}(p, L) + F_{\text{hysteresis}}(p, L, \dot{L}) \quad (3.30)$$

is a function of the PMA pressure, its length, and the first time-derivative of its length. The hysteresis is modeled with the Maxwell-Slip model in Section 3.4.2, which is the

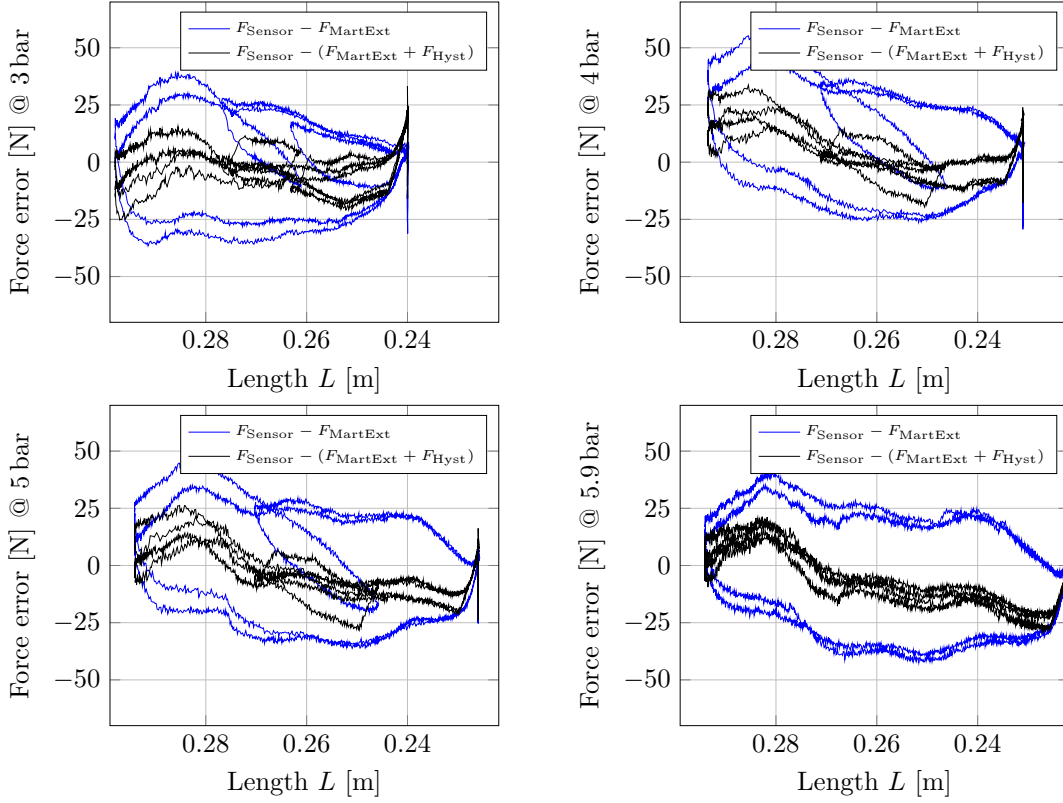


Figure 3.12.: Force prediction error of a model describing the DMSP-20-300 static force with (black) and without hysteresis (blue), respectively.

most accurate model, representing the static PMA force defined by the extended static force model (3.22)

$$F_{\text{static}}(p, L) = F_{\text{MartExt}}(p, L) = -p\mathcal{A}(L) + \mathcal{B}(L), \quad (3.31)$$

where the factors, denoted as \mathcal{A} and \mathcal{B} , can be explicitly written as

$$\mathcal{A}(L) = \frac{\partial V}{\partial L} + \frac{L_0^2}{4\pi n^2 \cos^2 \theta_0} d_1 \quad (3.32)$$

$$\mathcal{B}(L) = \pi \cdot H_0 \cdot E_{\text{ru}}(L) \left(L \cdot \varepsilon_{\text{pe}} \cdot \frac{\partial D}{\partial L} - D \cdot \varepsilon_L \right) + d_2. \quad (3.33)$$

Furthermore, the pressure will be subdivided into a mean pressure p_m on the one hand and an offset pressure of Δp on the other hand, i.e. $p = p_m + \Delta p$. By introducing the

subdivided pressure as well as (3.32) into (3.30), the PMA force is given as

$$F(p, L, \dot{L}) = \underbrace{-\Delta p \mathcal{A}(L)}_{=: F_{\text{so}}} \underbrace{-p_{\text{m}} \mathcal{A}(L) + \mathcal{B}(L)}_{=: F_{\text{sp}}} \underbrace{+ F_{\text{hysteresis}}(p, L, \dot{L})}_{=: F_{\text{d}}}. \quad (3.34)$$

The PMA force now consists of three parts (see Fig. 3.13) that can be interpreted as follows: Firstly, F_{so} represents a force source and only this force is exerted actively by the PMA. Secondly, the force F_{sp} can be interpreted as the result of a pre-stressed spring. The pre-stress is adjustable via a variation of the mean pressure p_{m} . Lastly, in accordance with Section 3.4, the force F_{d} dissipates energy from the PMA while it contracts or expands, hence this force can be interpreted as a damping force.

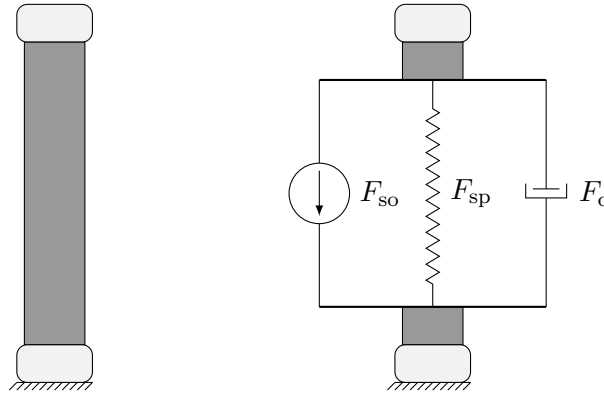


Figure 3.13.: Mechanical interpretation of a PMA as a combination of force source, spring and damper

Since the PMA hysteresis is a given attribute of the PMA, its damping force cannot be influenced. The exerted force can be varied by a variation of Δp , but – since the focus is set to the passive attributes – this should not be of interest for this section. In accordance with (3.34), the spring force F_{sp} is a function of the PMA length and its mean pressure, but only the latter one can be set freely. The stiffness

$$\frac{\partial F_{\text{sp}}(p_{\text{m}}, L)}{\partial L} = -p_{\text{m}} \frac{\partial \mathcal{A}(L)}{\partial L} + \frac{\partial \mathcal{B}(L)}{\partial L} \quad (3.35)$$

for a non-linear spring is defined as the partial derivative of the force with respect to length. For the sake of compactness, the derivatives $\frac{\partial \mathcal{A}}{\partial L}$ and $\frac{\partial \mathcal{B}}{\partial L}$ are provided in the Appendix A.1.

As an example, the stiffness of a Festo DMSP-20-300 is given in Fig. 3.14, with the black lines representing the stiffness of the PMA for constant pressure. The pressure increases in half-bar steps from 0.5 bar (lowest black line) to 6 bar (highest black line).

For a start, it stands out that the upper and lower stiffness limit are varying with the PMA length. While the stiffness is very high at the initial length (300 mm), the stiffness

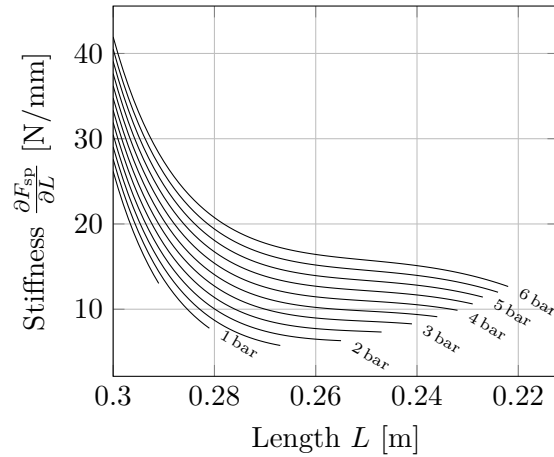


Figure 3.14.: Stiffness of a Festo DMSP-20-300 for different pressures

range is decreasing with increasing contraction. For every length, the stiffness of the PMA can be varied within a certain stiffness range by increasing or decreasing the pressure. Hence, it can be said that the PMA is an actuator with a variable stiffness. Although this statement is true, it gets weakened by the fact that the stiffness range does not provide the possibility to keep the stiffness constant for every length, i.e. the PMA could not behave – even under accurate control – like a linear spring. In cases where not the full contraction of the PMA is needed, the length range of the PMA can be defined as smaller and placed somewhere between the initial length and maximum contraction, in accordance with the stiffness requirements. Especially the area around half contraction provides almost constant stiffness levels, and due to this, keeping or adjusting the PMA stiffness is easier within this area. In this area the PMA behaves almost as a linear spring.

3.7. Conclusion and Future Work

The PMA is defined by the force it exerts for any combination of pressure and length. It is shown that the PMA force consists of a static force and a dynamic force, better known as the PMA hysteresis.

In Section 3.3, it was shown that although many static force models are already existing, their accuracy (see Section 3.3.6) differs significantly. Furthermore, it was demonstrated that a new approach, modeling the static PMA force, is closer to the measured force map than any existing approach. The comparison of different models is facilitated by the introduction of a novel parameter identification methodology, introduced in Section 3.3.5. A disadvantage of all existing models is that they must be adapted to a measured PMA force map. Since measuring the PMA force is challenging and the required measurement setup is rather complex, a knowledge of PMAs is indispensable for using these models.

Due to this, none of these models represents a "plug-and-play" model that could be used directly. In addition, most existing models – although mostly physically motivated – seem to represent the "true" PMA force characteristic only partially and the remaining difference between measured force map and model can be significant. Due to this, it is desirable for future work to study models that describing the PMA force with higher precision entirely via known physical relations and a-priori known geometrical and material parameters.

As shown in Section 3.4.2, there are good approximations available to model the PMA hysteresis. However, it is not clarified yet what the underlying physical principles of the hysteresis are.

Lastly, the ability of PMAs to vary their stiffness was shown in Section 3.6. This feature makes PMAs a perfect candidate to solve problems of modern robotic systems: They provide passive compliance and thus safety on the one hand, and they are able to store potential energy, which can improve the energy efficiency, on the other hand. The following chapter will demonstrate how the variable stiffness of a single PMA can be used to vary the joint co-contraction of antagonistic muscle pairs and finally the stiffness of robotic systems.

4. The PMA-driven Joint under Torque Control

4.1. Introduction

The majority of robots is driven by electrical motors. These drives are commonly used, since they are easy to control and well understood. Nevertheless, they do not provide any compliance and thus little safety. Since electrical motors are rotational actuators, it is not surprising that most robots have only revolute joints. Accordingly, a robot with x DOF mostly has x rotation axis. Since PMAs can only pull linearly, they are often combined as antagonistic pairs, i.e. they can provide a rotation and/or a torque around one axis. This particular antagonistic pair of two muscles will be further denoted as a *PMA-driven joint* and is – by far – the most favored configuration of PMAs in robotic systems. The serial link manipulators [56, 70, 37, 20], the humanoids [19, 18, 66, 58, 4], the animal-like robot [45], and the exoskeleton of [3] are only some examples of robots with PMA-driven joints.

Because of its importance, the PMA-driven joint will be further treated and investigated as an actuator of its own. As well as any other actuator, the PMA-driven joint also has its own characteristics, like its torque and angle range and its bandwidth. The investigation of these characteristics has received only little attention in the literature. Due to this, the following chapter strives to provide a deep analysis of the characteristics PMA-driven joints. With this at hand, the choice whether or not a PMA-driven joint represents a suitable actuator gets simplified. Furthermore, based on the characteristics, a novel interface is proposed that simplifies the use of PMA-driven joints in robotic applications. In addition, the following chapter aims at providing a deeper understanding of PMA-driven joints, i.e. it becomes possible to adapt the PMA-driven joint respectively its torque and angle range (Section 4.3), the bandwidth (Section 4.5), and, via cocontraction, its torsional joint stiffness (Section 4.5) to the requirements of a specific robotic system and its task.

It is important to highlight that some of the findings and methods, presented in the following chapter, have already been published, by the author, in

M. Martens, A. Passon, and I. Boblan. A sensor-less approach of a torque controller for pneumatic muscle actuator driven joints. In *2017 3rd International Conference on Control, Automation and Robotics*, pages 477–482. IEEE, April 2017

M. Martens, T. Seel, and I. Boblan. A decoupling servo pressure controller for pneumatic muscle actuators. In *23rd International Conference on Methods and Models in Automation and Robotics*. IEEE, 2018

M. Martens, T. Seel, J. Zawatzki, and I. Boblan. A novel framework for a systematic integration of pneumatic-muscle-actuator-driven joints into robotic systems via a torque control interface. In *Actuators*, volume 7, page 82. Multidisciplinary Digital Publishing Institute, 2018.

4.2. Overview

A PMA-driven joint is a combination of two PMAs and a pulley with the radius R , which can rotate around a fixed center. The rotation can be initiated by the PMAs, connected to the pulley via a rope or chain. As can be seen in Fig. 4.1, the PMA^+ pulls in a clockwise and the PMA^- in a counter-clockwise direction. Furthermore, the rotation-representing angle φ is defined to be positive for clockwise rotation, while the radius is supposed to be constant.

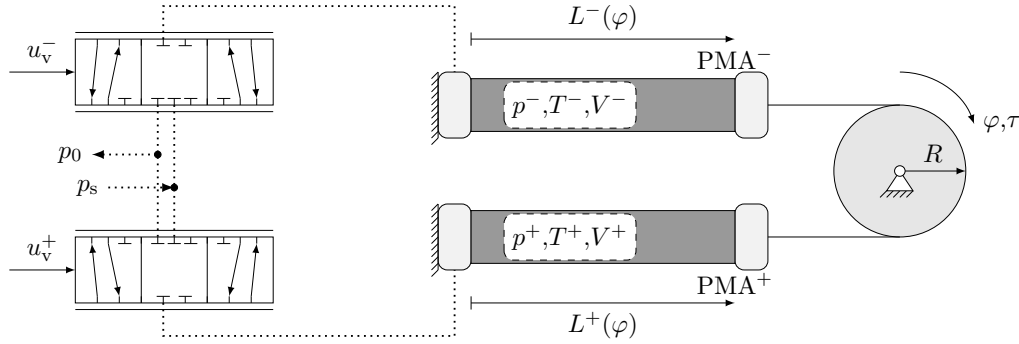


Figure 4.1.: Schematic of a PMA-driven joint

The torque

$$\tau_{\text{PMA}} = R \left[F_{\text{PMA}}^+ - F_{\text{PMA}}^- \right], \quad (4.1)$$

that the PMA-driven joint can exert is defined as the product of the pulley radius and the force difference. Due to the kinematic coupling of the PMA lengths, they are only a function of the pulley angle φ and given as

$$L^+(\varphi) = L_m - R \cdot \varphi \quad \text{and} \quad L^-(\varphi) = L_m + R \cdot \varphi. \quad (4.2)$$

The angle range is symmetric around $\varphi = 0$, which represents the angle where both PMAs are at mean length L_m . The mean length is mostly set to the length of half-contraction, which is the case for all investigations of this thesis due to the fact that this configuration

leads to the widest angle range. Nevertheless, the mean length can be defined differently and an excellent discussion about this particular topic is given in Dirven and McDaid [30].

As depicted in Fig. 4.1, each PMA pressure is controlled by a pneumatic valve. By changing the electrical control signal u_v^\pm , either the supply pressure p_s or the atmospheric pressure p_0 can be connected to the PMA. Due to this, the PMA pressure p^\pm and, as a result, its volume V^\pm and its temperature T^\pm are varying.

The creation of a torque controller for PMA-driven joints is the major goal of this chapter. As depicted in Fig. 4.2, the general structure of the torque controller can be subdivided into a *torque-to-pressure conversion* and two *pressure controllers*, one for each PMA. The force difference between both PMAs defines a joint torque that the PMA-driven joint exerts. Since this torque controller is designed without direct torque feedback, this is called a *sensor-less* approach [75].

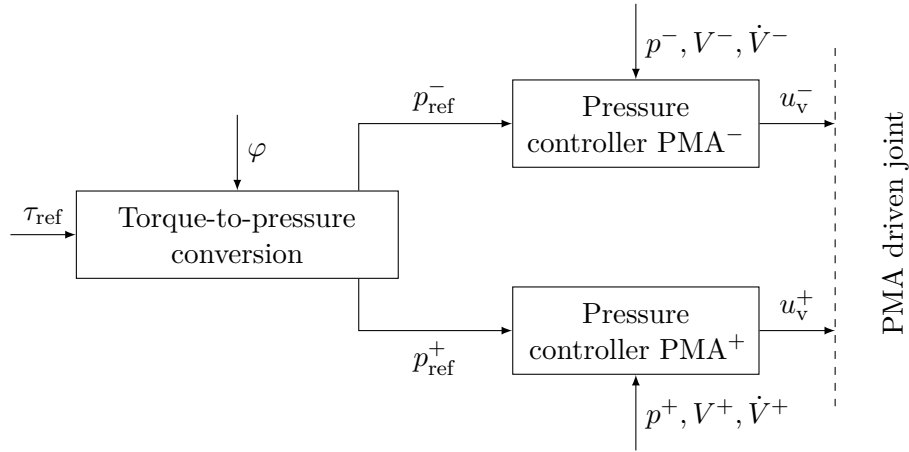


Figure 4.2.: Structure of the sensor-less torque controller for a PMA-driven joint

An advantage of the present torque control structure is that the adjustment of the torque and angle range on the one hand and the adjustment of the bandwidth on the other hand are completely separated. It will be shown in Section 4.3.1 and 4.3.2 that the torque-to-pressure conversion is purely algebraic, i.e. the pressure trajectories p_{ref}^\pm can be calculated directly from a given torque trajectory. Furthermore, it will be demonstrated that only the conversion law limits the torque range that the PMA-driven joint is able to exert. The torque range will be further denoted as the PMA-driven joints *torque characteristic*. In contrast to the torque-to-pressure conversion, the pressure controllers are representing dynamical systems, i.e. only the pressure controller's bandwidth can limit the bandwidth of the torque controller. After developing a gain scheduling pressure controller, without integral action in Section 4.5.3 and with integral action in Section 4.5.4, it will be shown that, once the PMA pressure is under torque control, the closed-loop behavior is fully described by a first-order low pass filter. As a result,

the torque controller itself behaves like a first-order lag filter and its bandwidth can be tuned by the pressure controllers.

4.3. Torque Characteristics

A precise model of the PMA force is essential to control the torque of a PMA-driven joint. According to the previous chapter, the PMA force is dominated by its static component. Therefore, the most precise model, describing the static PMA force, will be used for controlling the torque of a PMA-driven joint. In accordance with Tab. 3.4 (see. Section 3.3.6), the PMA force model with the highest precision is given by (3.22), denoted as the extended static force model. Furthermore, the hysteresis will be treated as a disturbance and, at the beginning, will be neglected for the following controller design.

Going back to (4.1), and substituting (3.22), it can be seen that the torque is a function of both PMA's lengths and their pressures. Once the angle – and due to this the PMA lengths – is given, the torque can only be varied by the PMA pressures. As depicted in Fig. 4.2, it is necessary to translate the torque into two different pressures. The problem that occurs is that the system of equations is not solvable with only one equation. To ensure solvability, the system of equations must be extended by another equation – which comes along with an additional constraint –, and this is done in Section 4.3.1 and 4.3.2. It will be shown that the torque characteristics of the PMA-driven joint depends crucially on the definition of this additional equation.

4.3.1. Torque-to-Pressure Conversion by Force Separation – The FIT Converter

Since the PMA force was accurately defined in the previous chapter, a first approach for solving (4.1) with respect to the pressures p^\pm will be presented in this section. As first published by Martens et al. [50], separating the torque into two forces, and defining that each PMA is only responsible for a torque in one direction, the forces are given through

$$F_{\text{PMA}}^+ = \begin{cases} \frac{\tau}{R} + F_{\text{IT}} & \text{if } \tau \geq 0 \\ F_{\text{IT}} & \text{if } \tau < 0 \end{cases} \quad F_{\text{IT}} \geq 0 \quad \text{and} \quad (4.3)$$

$$F_{\text{PMA}}^- = \begin{cases} F_{\text{IT}} & \text{if } \tau \geq 0 \\ \frac{|\tau|}{R} + F_{\text{IT}} & \text{if } \tau < 0. \end{cases} \quad F_{\text{IT}} \geq 0 \quad (4.4)$$

The force F_{IT} can be interpreted as an initial tension and is giving the name of this torque control approach: the *FIT converter*.

Once the torque is split up into two individual forces, the PMA pressures

$$p^\pm = \frac{\mathcal{B}(L^\pm) - F_{\text{PMA}}^\pm}{\mathcal{A}(L^\pm)}. \quad (4.5)$$

can easily be calculated by inserting the individual PMA length and its force, where the factors \mathcal{A} and \mathcal{B} are defined in (3.32). Following the results of the previous chapter, the static force most precise representation is given by $F_{\text{MartExt}}(p, L)$ (3.31) and due to this it is the chosen force model in (4.5). The resulting torque characteristics of a torque controller with a FIT converter can be seen in Fig. 4.4. An advantage of this approach is that it implicitly fulfills the important constraint $F^\pm \geq 0$ without any further calculations, i.e. the ropes can be kept tight while the PMA-driven joint is in service. A loss of contact to the pulley should be avoided because this would change the system dynamics abruptly, i.e. – at worst – the system could become unstable. By taking $\mathcal{A}(L)$ as a divisor, it is of high interest to clarify whether or not $\mathcal{A}(L)$ becomes zero within a certain PMA length range. According to the corresponding data sheet [32], the PMA contraction is between 0% and 25%. For the sake of safety, and just in case the PMA contraction is not in accurate accordance with the data sheet, the maximum contraction is supposed to be 30%. As an answer to this question, Theorem 1 defines a proper parameter range for an $\mathcal{A}(L)$ without singularities for a PMA contraction between 0% and 30%.

Theorem 1. *Let L represent the length of a Festo PMA and θ_0 its initial fiber angle. For any $\theta_0 \in (0^\circ, 30^\circ)$ and $d_1 \in [-1, 0.1025]$, $\mathcal{A}(L) = \frac{\partial V}{\partial L} + \frac{L_0^2}{4\pi n^2 \cos^2 \theta_0} d_1 \neq 0 \quad \forall L \in [0.7L_0, L_0]$, as defined in (3.32).*

Proof. (Proof by contradiction) Let $L_z \in [0.7L_0, L_0]$ be a zero of $\mathcal{A}(L_z)$, i.e. $\mathcal{A}(L_z) = 0$, $\theta_0 \in (0^\circ, 30^\circ)$ and $d_1 \in [-1, 0.1025]$. Consequently,

$$\begin{aligned} \mathcal{A}(L_z) &= \frac{(L_{\text{Fiber}}^2 - 3L_z^2)}{4\pi n^2} + \frac{L_0^2 d_1}{4\pi n^2 (\cos \theta_0)^2} = 0 \\ &\stackrel{4\pi n^2 > 0}{\iff} L_{\text{Fiber}}^2 - 3L_z^2 + \frac{L_0^2 d_1}{(\cos \theta_0)^2} = 0 \\ &\iff L_{\text{Fiber}}^2 + \frac{L_0^2 d_1}{(\cos \theta_0)^2} = 3L_z^2 \\ &\iff \frac{L_0^2}{(\cos \theta_0)^2} + \frac{L_0^2 d_1}{(\cos \theta_0)^2} = 3L_z^2 \\ &\iff \frac{L_0^2}{(\cos \theta_0)^2} (1 + d_1) = 3L_z^2 \stackrel{L_z > 0}{\implies} L_z = \frac{L_0}{\cos \theta_0} \sqrt{\frac{1 + d_1}{3}} \end{aligned}$$

Since $\sqrt{1+d_1/3}$ and $1/\cos \theta_0$ are continuous, monotonically increasing functions and $1/\cos \theta_0 > 0$ for the given range of θ_0 and d_1 , – as a composition –, $\sqrt{1+d_1/3}/\cos \theta_0$ must be

a continuous and monotonically increasing function, too. While the factor's minimum is zero for $d_1 = -1$, its local supremum is reached for $\theta \rightarrow 30^\circ$ and $d_1 = 0.1025$, i.e. $\sqrt{\frac{1+d_1}{3}}/\cos\theta_0 \rightarrow 0.7$. Due to this, L_z is always in the range of $[0, 0.7L_0)$, i.e. $\mathcal{A}(L_z)$ cannot be zero for either $L \in [0.7L_0, L_0]$, the given range of θ_0 or d_1 . ζ

According to this, $\mathcal{A}(L) \neq 0 \quad \forall L \in [0.7L_0, L_0]$ holds true for all Festo PMAs with $\theta_0 \in (0^\circ, 30^\circ)$ and $d_1 \in [-1, 0.1025]$. \square

4.3.2. Torque-to-Pressure Conversion by Mean Pressure Definition – The PM Converter

In contrast to the FIT converter, (4.1) can also be solved with respect to the pressures p^\pm by the definition of a common mean pressure

$$p_m = \frac{p^+ + p^-}{2}, \quad (4.6)$$

and this is probably the top choice [36, 7, 3, 15, 4]. This mean pressure is typically set to a constant value, but this is risky – as it will be shown in this section –, since the ropes can lose their contact to the pulley, i.e. the dynamics of the system changes abruptly and – at worst – the system becomes unstable.

Due to its dependency on a common mean pressure, this torque-to-pressure converter will be denoted as the *PM converter*. Assuming that the mean pressure is known, the equations (4.1) and (4.6) can be solved with respect to p^+ and p^- , respectively. For example, p^- is found to be

$$p^- = \frac{\frac{\tau}{R} + 2p_m\mathcal{A}(L^+) + \mathcal{B}(L^-) - \mathcal{B}(L^+)}{\mathcal{A}(L^+) + \mathcal{A}(L^-)}. \quad (4.7)$$

By inserting (4.7) back into (4.6), the second pressure

$$p^+ = 2p_m - p^- \quad (4.8)$$

can easily be calculated.

To avoid singularities, it must be clarified whether or not $\mathcal{A}(L^+) + \mathcal{A}(L^-)$ becomes zero. In accordance with the previous section, the maximum PMA contraction is supposed to be 30 % as a measure of safety, and this is slightly above 25 %, which is the maximum contraction of a Festo PMA according to the corresponding data sheet [32].

Theorem 2. *Let $L^\pm \in [0.7L_0, L_0]$ represent the lengths of two PMAs of a PMA-driven joint and let θ_0 be their initial fiber angle. Furthermore, let d_1 be a parameter necessary for the calculation of the extended static PMA force (3.22). If $\mathcal{A}(L^\pm) \neq 0 \quad \forall \theta_0 \in (0^\circ, 30^\circ)$ and $d_1 \in [-1, 0.1025]$, then $\mathcal{A}(L^+) + \mathcal{A}(L^-) \neq 0 \quad \forall \theta_0 \in (0^\circ, 30^\circ)$.*

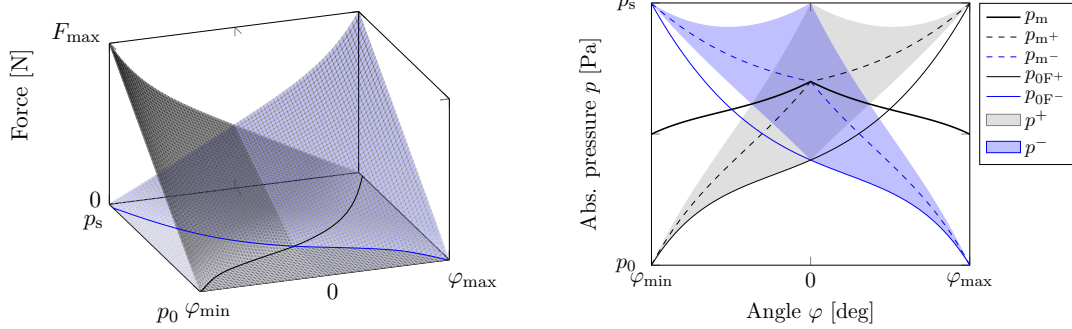
Proof. According to Theorem 1, $\mathcal{A}(L)$ has no zero for $L \in [0.7L_0, L_0]$. Due to this, $\mathcal{A}(L)$ does not change its sign for $L \in [0.7L_0, L_0]$, $d_1 \in [-1, 0.1025]$, and $\theta_0 \in (0^\circ, 30^\circ)$. Furthermore, as a combination of continuous functions, $\mathcal{A}(L)$ is also a continuous function. This implies that $\mathcal{A}(L^+) + \mathcal{A}(L^-)$ must have the same sign as $\mathcal{A}(L)$, so that

$$\mathcal{A}(L^+) + \mathcal{A}(L^-) = 0 \quad \Leftrightarrow \quad \mathcal{A}(L^+) = 0 \quad \wedge \quad \mathcal{A}(L^-) = 0.$$

Consequently, $\mathcal{A}(L^+) + \mathcal{A}(L^-) \neq 0 \quad \forall L^\pm \in [0.7L_0, L_0]$ holds true for all Festo PMAs with $\theta_0 \in (0^\circ, 30^\circ)$ and $d_1 \in [-1, 0.1025]$. \square

Theorem 2 guaranties that $\mathcal{A}(L^+) + \mathcal{A}(L^-) \neq 0$, as long as $L \in [0.7L_0, L_0]$, $\theta_0 \in (0^\circ, 30^\circ)$, and $d_1 \in [-1, 0.1025]$.

A consequence of connecting two PMAs – each able to exert a force – to a shared pulley is that the force map of the first PMA overlaps the force map of the second PMA, as depicted in Fig. 4.3a. As explained in Chapter 3, the PMA force is a function of the PMA pressure and its length. Since both PMAs are connected to a shared pulley, their lengths are defined by the angular position and the radius of the pulley, and only their individual pressures can be chosen independently. The angle range is given by $\varphi \in [\varphi_{\min}, -\varphi_{\max}]$ and is symmetric in case of connecting two equivalent PMAs at half-contraction.



(a) Overlap of two PMA force maps, so that both PMAs are connected at half-contraction. The bottom lines are representing the curve of zero PMA force.

(b) Top view of the left picture; characteristics of the mean pressure p_m for $s_{\text{pmc}} = 0.5$. The black, respectively the blue, area are showing the valid pressure ranges for PMA⁺ and PMA⁻, so that tight ropes can be guaranteed.

Figure 4.3.: Overlap of two PMA force maps; PMA⁺ colored in black, PMA⁻ colored in blue

The black force map in Fig. 4.3a represents the force of PMA⁺, pulling in the positive direction, while the blue force map represents the force of PMA⁻, pulling in the opposite, negative, direction. The blue and black curved diagonals represent the zero-force lines

p_{0F}^+ and p_{0F}^- of the force map of PMA⁺ p_{0F}^+ (black) and PMA⁻ (blue), respectively. The area of $F^+ \geq 0$ in Fig. 4.3b is therefore the upper left curved triangle, and the area of $F^- \geq 0$ the upper right curved triangle. Since PMAs can only pull and not push, the area of – theoretical – pushing is constantly zero.

The mean pressure – supposed to be known but not set to a specific value so far – can be used to fulfill the most important constraint for a PMA-driven joint: the avoidance of loose ropes. Since PMAs can only pull and this is defined to be a positive force, tight ropes can be guaranteed as long as $F^\pm \geq 0$, i.e. the PMA forces stay always positive. Assuming the angle defines a length for both PMAs, keeping their forces positive can be translated easily to keeping their pressures always above their individual pressures of zero force p_{0F}^\pm . It should be noted that, due to the coupling of both PMA pressures with a common mean pressure, keeping one pressure between p_{0F} and the supply pressure, does not imply that the other pressure lies within this pressure range as well. The valid pressure ranges, guaranteeing $F^\pm \geq 0$, can be determined as follows:

- For every angle, the upper individual mean pressure p_m^- (Fig. 4.3b blue dashed line), respectively p_m^+ (Fig. 4.3b black dashed line) is set to

$$p_m^+ = s_{\text{pmc}} p_s + (1 - s_{\text{pmc}}) p_{0F}^+ \quad \text{or} \quad p_m^- = s_{\text{pmc}} p_s + (1 - s_{\text{pmc}}) p_{0F}^-, \quad (4.9)$$

where p_s represents the supply pressure and $s_{\text{pmc}} \in [0,1]$ is a factor for stiffness adjustment, as will be shown in Section 4.4. For example, by defining $s_{\text{pmc}} = 0.5$, the resulting mean pressure would lie in the middle of p_{0F}^\pm and the supply pressure p_s , as shown in Fig. 4.3b.

- The lower individual mean pressure is calculated so that the forces of both PMAs are equal if both PMAs are filled with their individual mean pressure.
- In accordance with (4.6), increasing one pressure always means decreasing the other in equal measure. Due to this, the smallest distance to the upper, respectively, lower pressure boundary always limits the valid pressure range for both PMAs, as represented by the black and the blue area in Fig. 4.3b for $s_{\text{pmc}} = 0.5$.
- Since the angle is supposed to be known, the valid pressure range defines a range of valid force for each PMA. The intersection set of both force ranges is taken as the valid force range for both PMAs, and the valid torque range is given by the product of the force range and the pulley radius.
- The common mean pressure p_m (bold black line) is a result of (4.6).

By defining the mean pressure like this, the torque characteristics of the resulting torque controller with a PM converter can be seen in Fig. 4.4. Finally, it can be said that, as long as the torque stays between its upper and lower limit and the mean pressure is defined like it is described above, the ropes will be kept tight.

4.3.3. A Comparison of Two Torque Characteristics

In Section 4.3.1 and 4.3.2, two different ways are shown of how one torque trajectory can be converted into two pressure trajectories. Since solving (3.31) with respect to the PMA pressures is impossible with only one equation, another equation must be employed so that the algebraic problem becomes solvable. It turned out that the torque characteristic of the maximum torque range that the torque controller is able to provide crucially depends on this additional algebraic constraint. In Fig. 4.4, the resulting torque characteristic for both torque control approaches, one with FIT and one with PM converter, are depicted, respectively.

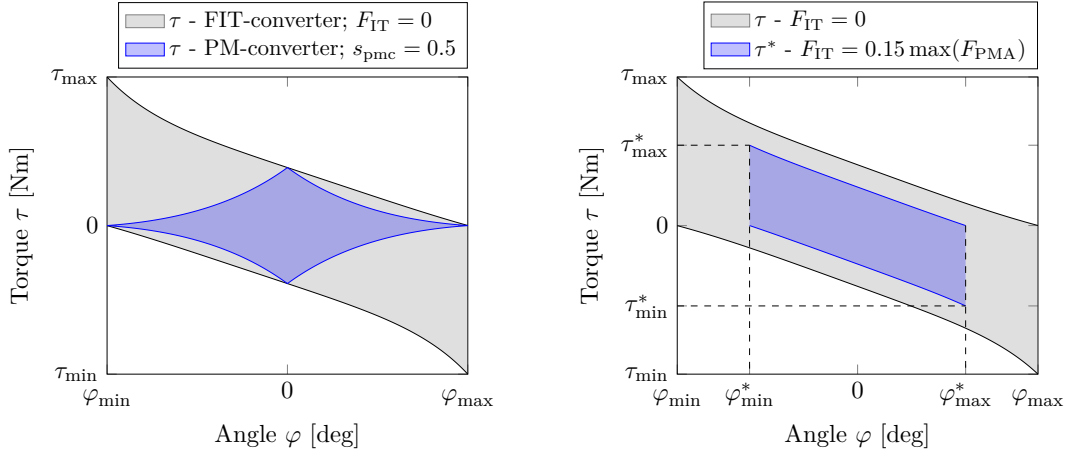
Fig. 4.4a shows a comparison of the maximum torque ranges that can be reached with a FIT converter and $F_{IT} = 0$ – no initial tension – or with a PM converter and $s_{pmc} = 0.5$, respectively. In the beginning, it is conspicuous that the PM-torque characteristic is symmetric around the φ -axis and the FIT-torque characteristic is not. Furthermore, the FIT converter provides the maximum torque at the edges, as can be explained by the natural behavior of the PMAs, while forces are at their maximum only at initial length. While the FIT converter has the ability to exploit the whole work potential of the PMA, the PM converter seems to use most of it as initial tension. In contrast to the FIT converter, the PM converter provides no torque at the edges and the maximum torque in the middle at $\varphi = 0$.

As can be seen in Fig. 4.4, the torque range of the PMA-driven joint can be varied with both the FIT and the PM converter. The remaining PMA forces are used as initial tension, which increases while the torque range decreases and vice versa. Accordingly, the initial tension – joint stiffness – is adjustable with both torque control approaches. Thereby, the initial tension of the FIT converter is adjustable by F_{IT} and the initial tension of the PM converter can be varied by s_{pmc} . Interesting to see is that, while the FIT converter has its maximum torque range without initial tension $F_{IT} = 0$ (see Fig. 4.4b), the torque range of the PM converter is at its maximum for $s_{pmc} = 0.5$ and decreases for $s_{pmc} \rightarrow 0$ and $s_{pmc} \rightarrow 1$ (see Fig. 4.4c and 4.4d). Besides the pure torque range the PMA-driven joint is able to provide, also its joint stiffness can be of interest for robotic applications. As it will be shown in the following Section 4.4, a higher joint stiffness decreases the torque range and vice versa.

4.4. The PMA-driven Joint - An Actuator with Variable Stiffness?

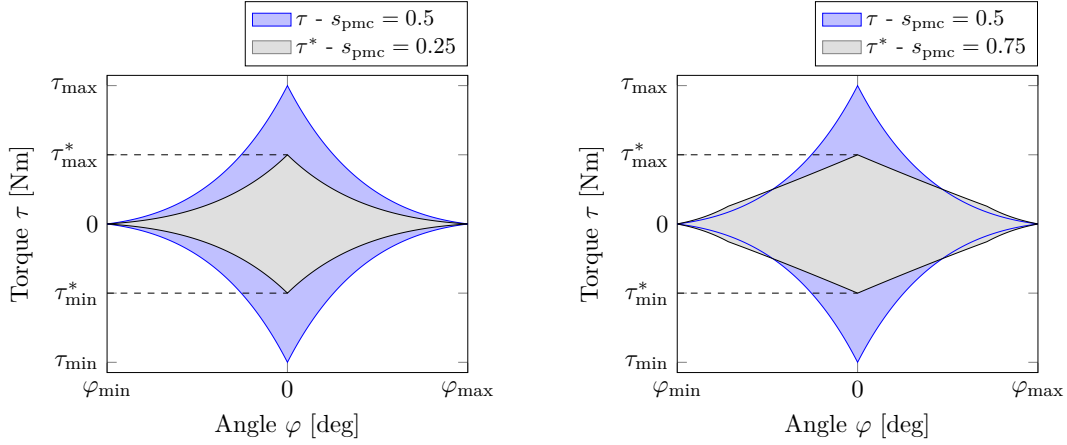
The joint torque of a PMA-driven joint is defined by (4.1). Its torsional spring stiffness

$$\frac{\partial \tau}{\partial \varphi} = R \left[\frac{\partial F^+}{\partial \varphi} - \frac{\partial F^-}{\partial \varphi} \right] = R \left[\frac{\partial F^+}{\partial L^+} \frac{\partial L^+}{\partial \varphi} - \frac{\partial F^-}{\partial L^-} \frac{\partial L^-}{\partial \varphi} \right] \quad (4.10)$$



(a) Maximum torque range; gray: FIT converter and $F_{\text{IT}} = 0$; blue: PM converter and $s_{\text{pmc}} = 0.5$

(b) Torque range FIT converter; gray: $F_{\text{IT}} = 0$; blue: $F_{\text{IT}} = 0.15 \max(F_{\text{PMA}})$



(c) Torque range PM converter; blue: $s_{\text{pmc}} = 0.5$; gray: $s_{\text{pmc}} = 0.25$

(d) Torque range PM converter; blue: $s_{\text{pmc}} = 0.5$; gray: $s_{\text{pmc}} = 0.75$

Figure 4.4.: Torque characteristics of a PMA-driven joint controlled by two different torque control approaches with integrated FIT and PM converters, respectively.

is the partial derivative of the torque with respect to the angle. The derivatives of the PMA lengths, defined in (4.2),

$$\frac{\partial L^+}{\partial \varphi} = -R \quad \text{and} \quad \frac{\partial L^-}{\partial \varphi} = R \quad (4.11)$$

are constant because of the constant pulley radius. Substituting (4.11) back into (4.10), the torsional stiffness

$$\frac{\partial \tau}{\partial \varphi} = -R^2 \left[\frac{\partial F^+}{\partial L^+} + \frac{\partial F^-}{\partial L^-} \right] \quad (4.12)$$

only depends on the stiffness of both PMAs, as described in Section 3.6 (3.35). By substituting this equation into (4.12) and keeping the pressure at mean pressure p_m , the stiffness of the PMA-driven joint

$$\frac{\partial \tau}{\partial \varphi} = -R^2 \left[-p_m^+ \frac{\partial \mathcal{A}^+}{\partial L^+} + \frac{\partial \mathcal{B}^+}{\partial L^+} - p_m^- \frac{\partial \mathcal{A}^-}{\partial L^-} + \frac{\partial \mathcal{B}^-}{\partial L^-} \right] \quad (4.13)$$

can be written in terms of \mathcal{A} and \mathcal{B} (defined in (3.32) and (3.33)). Their derivatives with respect to the PMA lengths, $\frac{\partial \mathcal{A}^\pm}{\partial L^\pm}$ and $\frac{\partial \mathcal{B}^\pm}{\partial L^\pm}$, are equivalent to $\frac{\partial \mathcal{A}(L^\pm)}{\partial L^\pm}$ and $\frac{\partial \mathcal{B}(L^\pm)}{\partial L^\pm}$, respectively. For the sake of clarity, the derivatives are not written explicitly but are provided in the Appendix A.1. As described in Section 4.3.1 and 4.3.2, the definition of the mean pressures p_m^\pm is highly dependent on the conversion from torque to pressure, and the influence of the mean pressure to the joint stiffness will be discussed in the following text.

4.4.1. Stiffness Adjustment with the FIT Converter

The FIT converter translates one torque in two pressures by separating positive and negative torques and then providing the torque with PMA⁺ or PMA⁻. In addition, both PMAs have to exert a common initial force F_{IT} , as defined by (4.5). This force can be interpreted as the initial tension of the PMAs, i.e. only this force defines the stiffness of the PMA-driven joint. Considering that $F^+ = F^- = F_{IT}$, the mean pressures

$$p_m^\pm = \frac{\mathcal{B}^\pm - F_{IT}}{\mathcal{A}^\pm} \quad (4.14)$$

can be calculated directly from (4.5). Due to this, the torsional stiffness (4.13)

$$\frac{\partial \tau}{\partial \varphi}(\varphi, F_{IT}) = -R^2 \left[-\frac{\partial \mathcal{A}^+}{\partial L^+} \cdot \frac{\mathcal{B}^+ - F_{IT}}{\mathcal{A}^+} + \frac{\partial \mathcal{B}^+}{\partial L^+} - \frac{\partial \mathcal{A}^-}{\partial L^-} \cdot \frac{\mathcal{B}^- - F_{IT}}{\mathcal{A}^-} + \frac{\partial \mathcal{B}^-}{\partial L^-} \right] \quad (4.15)$$

becomes adjustable only by a variation of F_{IT} . Fig. 4.5 visualizes the stiffness for an exemplary Festo DMSP-20-300 and a pulley radius of 23.24 mm. The radius is set to the pulley radius of the 1 DOF robot arm, which will be discussed in the next chapter.

Fig. 4.5 proves the hypotheses that the joint stiffness of a PMA-driven joint can be varied via an initial tension F_{IT} . The initial tension is related to the maximum PMA force by percentage. By increasing the initial tension, also the joint stiffness gets increased, but the angle of the PMA-driven joint gets smaller. Furthermore the joint stiffness of the PMA-driven joint can be increased – independently of its initial tension – by

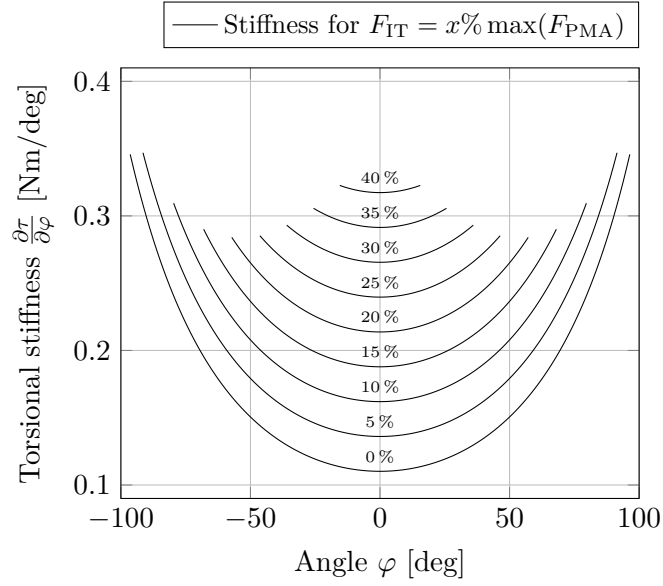


Figure 4.5.: Stiffness of the PMA-driven joint with FIT converter for an exemplary Festo DMSP-20-300 and a pulley radius of 23.24 mm

rotating away from the center position at 0° . The general shape of the joint stiffness over the joint angle is close to parabola shape with the chosen FIT converter approach.

4.4.2. Stiffness Adjustment with the PM Converter

Like the FIT converter, the PM converter also translates one torque into two PMA pressures. Since only the passive attributes of the PMA-driven joint are of interest for this section, the torque in (4.7) can be set to $\tau = 0$. The negative mean pressure

$$p_m^- = \frac{2p_m \mathcal{A}^+ + \mathcal{B}^- - \mathcal{B}^+}{\mathcal{A}^+ + \mathcal{A}^-} \quad (4.16)$$

of PMA⁻ as well as the positive mean pressure of PMA⁺ – from (4.8) –

$$p_m^+ = \frac{2p_m \mathcal{A}^- + \mathcal{B}^+ - \mathcal{B}^-}{\mathcal{A}^+ + \mathcal{A}^-} \quad (4.17)$$

are only functions of their individual lengths and a common mean pressure p_m . By going back to (4.13) and substituting p_m^\pm by (4.16) and (4.17), the torsional stiffness

$$\frac{\partial \tau}{\partial \varphi}(\varphi, p_m) = -R^2 \left[-\frac{\partial \mathcal{A}^+}{\partial L^+} \cdot \frac{2p_m \mathcal{A}^- + \mathcal{B}^+ - \mathcal{B}^-}{\mathcal{A}^+ + \mathcal{A}^-} + \frac{\partial \mathcal{B}^+}{\partial L^+} - \frac{\partial \mathcal{A}^-}{\partial L^-} \cdot \frac{2p_m \mathcal{A}^+ + \mathcal{B}^- - \mathcal{B}^+}{\mathcal{A}^+ + \mathcal{A}^-} + \frac{\partial \mathcal{B}^-}{\partial L^-} \right] \quad (4.18)$$

becomes adjustable via the common mean pressure of both PMAs. Furthermore, in accordance with Section 4.3.2 (4.9), the mean pressure can be changed by the factor

$s_{\text{pmc}} \in [0,1]$. As a result of varying s_{pmc} , not only the torque range varies (see Fig. 4.4) but also the joint stiffness of the PMA-driven joint changes, as can be seen in Fig. 4.6 for an exemplary Festo DMSP-20-300 and a pulley radius of 23.24 mm.

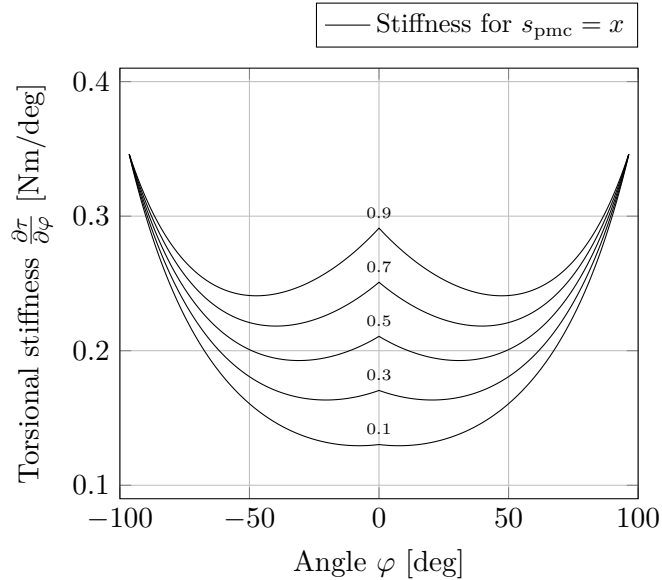


Figure 4.6.: Stiffness of the PMA-driven joint with PM-converter for an exemplary Festo DMSP-20-300 and a pulley radius of 23.24 mm

Fig. 4.6 shows the joint stiffness of a PMA-driven joint with PM converter. In contrast to the joint stiffness of a PMA-driven joint with FIT converter, the angle range is not dependent on the chosen joint stiffness. It can be seen that for different values of s_{pmc} that the angle range stays constant. The general shape of the joint stiffness over the joint angle is again very parabola-like but with a peak at the center position at 0° . Furthermore, the range of joint stiffness is almost the same as for the PMA-driven joint with FIT converter.

4.5. Pneumatic Pressure Control Inside Time-varying Volumes

Controlling the torque of a PMA-driven joint consists of two steps: Firstly, the torque is converted into two related pressures. This was done in the previous sections of this chapter. Secondly, one has to make sure that the desired pressure is reached inside both PMAs, i.e the torque-control task is translated into a pressure-control task. Due to this, two different gain scheduling pressure controllers for time-varying volumes – like PMAs – are designed in the following section. Within the next chapters, it will turn out that two different variants of a pressure controller are desirable for PMA-driven robots. On the

one hand, the task of positioning a PMA-driven robot, or making it follow a given angle trajectory, requires an underlying pressure controller with high bandwidth. Since the pressure controller is mostly embedded as an inner controller in a cascade-structured position controller, an integrator within the inner cascade is typically not necessary. On the other hand, a second group of applications, like the rehabilitation robot discussed in Chapter 7, are using the pressure controller in its pure form and have a demand for an exact pressure trajectory, i.e. integral action becomes essential.

The following pressure controller design can be subdivided into the following steps: After the valve function is canceled out by its inverse function in Section 4.5.1, the remaining system dynamics (2.1) is linearized in Section 4.5.2 to enable a linear controller design. By taking the linearized system dynamics as a base, a gain scheduling pressure controller design is carried out in Section 4.5.3 and Section 4.5.4 to handle the non-linear pressure dynamics properly. Finally, it will be shown that the closed pressure control loop behaves like a first-order low pass filter, thus its cut-off frequency defines the bandwidth of the pressure controllers. Since the torque-to-pressure conversion is purely static, the dynamics of the torque controller must be equal to the dynamics of the pressure controllers. Thus, the bandwidth of the torque controller equals the bandwidth of the pressure controllers.

4.5.1. The Mass Flow as Virtual System Input

Taking the mass flow as the virtual system input of (2.1) is common practice in the field of pneumatic pressure control [36, 7, 43] because it simplifies the pressure controller design significantly [51]. Since the mass flow (2.2) shaped by the pneumatic valve is a switching system yet purely algebraic, it can be canceled out by inversion. As a result, the pressure controller outputs a mass flow which must be transformed to a sonic conductance signal by the inverse mass flow

$$C = \begin{cases} \frac{\dot{m}}{\rho_0 p_s} \sqrt{\frac{T}{T_0}} & 0 \leq p < b p_s \wedge \dot{m} \geq 0 \\ \frac{\dot{m}}{\rho_0 p_s} \sqrt{\frac{T}{T_0}} \left[1 - \left(\frac{p-b}{1-b} \right)^2 \right]^{-\frac{1}{2}} & b p_s \leq p \leq p_s - p_\varepsilon \wedge \dot{m} \geq 0 \\ \frac{\dot{m}}{\rho_0 p} \sqrt{\frac{T}{T_0}} \left[1 - \left(\frac{p_0-b}{1-b} \right)^2 \right]^{-\frac{1}{2}} & p_0 + p_\varepsilon \leq p \leq \frac{p_0}{b} \wedge \dot{m} < 0 \\ \frac{\dot{m}}{\rho_0 p} \sqrt{\frac{T}{T_0}} & \frac{p_0}{b} < p \wedge \dot{m} < 0. \end{cases} \quad (4.19)$$

To avoid singularities, the pressure is limited to $p_0 + p_\varepsilon$ and $p_s - p_\varepsilon$, where the pressure gap is set to $p_\varepsilon = 0.1$ Pa.

Since the sonic conductance $C(x_v)$, as depicted in Fig. 2.1, is a monotonically increasing function of x_v , numerical inversion is straightforward, and the dependency $x_v(C) = u_v(C)$ can be calculated easily.

4.5.2. A Linear Interpretation of the System Dynamics

According to (2.1), the pressure dynamic is non-linear, so that it is not surprising that most pressure control approaches are non-linear control approaches, e.g. the exact linearization used in [36] or the sliding-mode pressure controller used in [8]. Nevertheless, other control approaches, like a linear [51] or a gain scheduling pressure controller [52], are suitable to solve the control problem with excellent results, too. Due to this, the system dynamics (2.1) will be re-formulated, so that a linear approximation becomes suitable.

At first, the latter summand $\frac{\chi}{V}p\dot{V}$ in (2.1) can be interpreted as a disturbance. By choosing the mass flow

$$\dot{m} = \hat{\dot{m}} + \underbrace{\frac{1}{R_{\text{gas}}T}}_{=:G_d(s)} \cdot p\dot{V}, \quad (4.20)$$

the disturbance can be compensated and $\hat{\dot{m}}$ becomes the new virtual input mass flow. By choosing the mass flow like this, it should be noted that – in case many time-varying volumes are sharing a kinematic structure –, each volume gets decoupled pneumatically from every other volume, so that a separated and local pressure control design for each volume is facilitated.

Through approximating the volume inside the time-varying volume by a constant volume $V = \bar{V}$ and supposing the temperature is constant at ambient temperature $T = T_a = T_0$, the new plant dynamics G_p is described as the linear time-invariant system

$$G_p(s) = \frac{p}{\dot{m}} = \frac{\chi R_{\text{gas}} T_a}{\bar{V}} \frac{1}{s}. \quad (4.21)$$

The continuous plant dynamic (4.21) is sampled with a sampling frequency of $T_s^{-1} = f_s$. Using a zero-order hold discretization, the z-transform of the plant is given as

$$H_p(z) = \frac{\chi R_{\text{gas}} T_a}{\bar{V}} \frac{T_s}{(z-1)} =: \frac{B_p}{A_p}, \quad (4.22)$$

which has only an integrating pole at $z = 1$.

4.5.3. Gain Scheduling Pressure Controller

Although non-linear control approaches might represent a suitable choice for controlling the non-linear pressure dynamics of a time-varying volume with maximum bandwidth, these control approaches are weak in fulfilling other control goals like noise reduction or a guarantee of robustness. From this perspective, the presented – basically linear – two-degree-of-freedom controller is superior because, besides the desired bandwidth and stability, other requirements like e.g. the suppression of isolated frequencies can be

directly included in the controller design. The influence of a time-varying volume on the pressure can be handled by this controller in two different ways: Firstly, in case the volume and its time derivative is measurable, the controller can be designed for different but constant volumes, and the controller gains can be interpolated in real time, i.e. the controller adapts its gains in dependency of the volume. Secondly, in case the volume is not measurable and can only be approximated by a constant volume, the controller can be designed for a constant volume and the influence of the time-varying volume must be handled by the robustness of the controller. As will be shown in the following chapters, the pressure control inside PMAs belongs to the first group, because the PMA volume is only dependent on its length (see (3.4)) and is therefore usually measurable.

Following the polynomial, pole-placement controller design procedure explained in Åström and Wittenmark [10], a so-called RST digital pressure controller with two degrees of freedom can be designed for a linear pressure control problem. Since (2.1) is only linear for a constant volume, the linear RST control approach is extended in the following way: Multiple RST controllers are designed for different volumes within a pre-defined and valid volume range, and their coefficients are interpolated linearly in real time with respect to the measured volume. In other words, the linear controller adapts its parameters with respect to the time-varying volume and balances its influence on the pressure. Furthermore, the controller is extended by a disturbance cancellation $H_d(z)$, which is the z-transform of $G_d(s)$ from (4.20), as proposed in [51]. The whole control structure is schematically depicted in Fig. 4.7. In order to determine the time-derivative of the volume \dot{V} without amplification of measurement noise, an algebraic derivative estimation algorithm, as presented by Zehetner et al. [82], is applied to the measured volume.

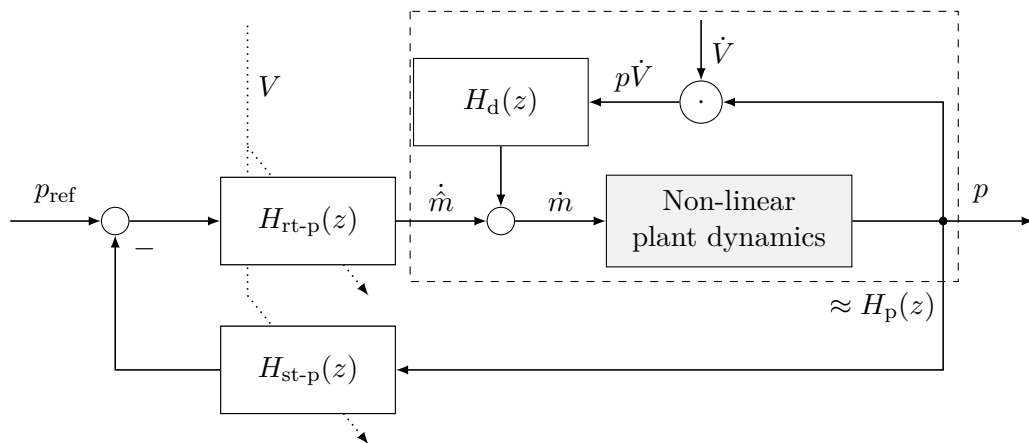


Figure 4.7.: Gain scheduling pressure controller with two degrees of freedom and disturbance cancellation

In accordance to the notation of Åström and Wittenmark [10], also the pressure controller

polynomials are denoted by $S_p(z)$, $T_p(z)$ and $R_p(z)$. Furthermore, the pressure controller

$$\dot{m} = \frac{T_p(z)}{R_p(z)} \left(p_{\text{ref}} - \frac{S_p(z)}{T_p(z)} p \right) \quad (4.23)$$

consists of two discrete-time transfer functions

$$H_{\text{rt-p}}(z) := T_p(z)/R_p(z) \text{ and} \quad (4.24)$$

$$H_{\text{st-p}}(z) := S_p(z)/T_p(z), \quad (4.25)$$

$$(4.26)$$

respectively. The plant transfer function is represented by B_p/A_p (see (4.22)) and the closed-loop dynamics is represented by

$$H_{\text{clp}} = \frac{p}{p_{\text{ref}}} = \frac{B_p T_p}{A_p R_p + B_p S_p}. \quad (4.27)$$

Like it can be seen in (4.27), the given closed-loop dynamics can now be shaped by the controller polynomials $S_p(z)$, $T_p(z)$ and $R_p(z)$. The poles of the closed loop can be defined by placing the zeros of the denominator of (4.27) and the resulting definition of

$$A_{\text{clp}} := A_p R_p + B_p S_p \quad (4.28)$$

, the characteristic polynomial of the closed loop. Since the closed-loop dynamics can only be influenced by the controller, the controller polynomials $S_p(z)$ and $R_p(z)$ must be determined from the desired closed-loop behavior and are the result of the controller design procedure.

Starting with the controller design, the first information needed is the degree of the characteristic polynomial, i.e. the number of poles one has to define. In general the degree of A_{clp} is $\max(\deg(A_p R_p), \deg(B_p S_p))$. Due to causality, it is $\deg(B_p) \leq \deg(A_p)$ for the plant and $\deg(S_p) \leq \deg(R_p)$ for the controller polynomials. In accordance to Åström and Wittenmark [10] it is common to chose $\deg(S_p) = \deg(R_p) = \deg(T_p)$ in case the computation is small compared to the sampling time. Furthermore, if $\deg(A_p) = n$, the minimum-degree solution of the control problem corresponds to $\deg(S_p) = n - 1 < \deg(A_p)$. In summary, the characteristic polynomial of the closed loop is at least of order $n + (n - 1)$, but can be higher in case the controller has to fulfill additional requirements that are commonly expressed as additional zeros of the controller polynomials.

In contrast to other control approaches, the chosen RST control approach enables an easy integration of additional control requirements like e.g. frequency suppression at isolated frequencies. This can be done by adding additional zeros $s_{d,i}$ $i \in \mathbb{N}$ to the controller polynomial $S_p(z)$ [10]. The additional zeros of $S_p(z)$ will be represented in

the following text by the polynomial

$$S_{\text{dp}}(z) = \prod_i (z - s_{\text{d},i}) \quad i \in \mathbb{N}. \quad (4.29)$$

Accordingly, the degree of the closed-loop characteristic polynomial, can be calculated as

$$\deg(A_{\text{clp}}(z)) = 2 \deg(A_{\text{p}}(z)) - 1 + \deg(S_{\text{dp}}(z)). \quad (4.30)$$

Once the closed-loop characteristic polynomial is defined the polynomials $S_{\text{p}}(z)$ and $R_{\text{p}}(z)$ are calculated by solving the Diophantine equation (4.28) with respect to the given characteristic polynomial A_{clp} . The stability of the closed pressure loop is ensured if all poles are placed inside the unit circle ([10] p. 79, Theorem 3.1). Besides pure stability, it is possible to fulfill additional requirements by distributing the poles accordingly inside the unit circle.

Now the controller polynomials $S_{\text{p}}(z)$ and $R_{\text{p}}(z)$ are determined, at next $T_{\text{p}}(z)$ can be exploited to improve the general controller performance. As a consequence of the chosen two-degrees-of-freedom control structure, the closed loop poles can be subdivided into so-called *observer poles* and so-called *closed-loop poles*, and only the latter ones are defining the visible dynamics of the closed control loop. The observer poles can be easily canceled out by defining the zeros of the third controller polynomial $T_{\text{p}}(z)$. As a result of the equal order of $S_{\text{p}}(z), T_{\text{p}}(z)$ and $R_{\text{p}}(z)$, the present closed-loop pressure dynamics is defined by only one pole and the remaining $\deg(A_{\text{clp}}) - 1$ poles are all observer poles. Finally, the closed-loop polynomial

$$A_{\text{clp}}(z) = (z - P_{\text{c}}) \cdot \prod_{i=1}^{\deg(A_{\text{clp}})-1} (z - P_{\text{o},i}) \quad (4.31)$$

only consist of a first order polynomial with one zero at

$$P_{\text{c}} = e^{-2\pi T_{\text{s}} f_{\text{bw}}} \quad (4.32)$$

and multiple zeros at $P_{\text{o},i}$. Moreover, only the choice of P_{c} defines the bandwidth f_{bw} of the closed pressure control loop, with respect to the given sample time T_{s} , at which the continuous system is sampled.

Since only one pole defines the closed loop dynamics,

$$H_{\text{clp}} = \frac{1 - P_{\text{c}}}{z - P_{\text{c}}} \quad (4.33)$$

represents the transfer function of the closed pressure control loop.

4.5.4. Gain Scheduling Pressure Controller with Integral Action and Anti-windup

Since every application defines its own requirements, there is no general pressure controller that fulfills all requirements at once. While a pressure controller used e.g. for the positioning of a PMA-driven robot is mostly embedded in an overlying position control loop, and there is thus almost no integral action required, a precise pressure controller can be desirable in case the pressure controller is used in its pure form. As will be shown in Chapter 7, the rehabilitation robot represents a system with the demand on pressure controller with integral action. Due to this, the gain scheduling RST-digital controller of the previous section will be extended by integral action in this section. Furthermore, the controller

$$\dot{m} = \frac{T_p(z)}{A_w(z)} \left(p_{\text{ref}} - \frac{S_p(z)}{T_p(z)} p + \frac{A_w(z) - R_p(z)}{T_p(z)} \dot{m}_{\text{sat}} \right) \quad (4.34)$$

is extended by a gain scheduling anti-windup mechanism, as depicted in Fig. 4.8. The discrete time transfer functions are defined as

$$H_{\text{taw-p}}(z) := T_p(z)/A_w(z), \quad (4.35)$$

$$H_{\text{st-p}}(z) := S_p(z)/T_p(z) \text{ and} \quad (4.36)$$

$$H_{\text{aw-p}}(z) := A_w(z) - R_p(z)/T_p(z), \quad (4.37)$$

$$(4.38)$$

respectively. The saturated mass flow

$$\dot{m}_{\text{sat}} = \dot{m}(u_{\text{sat}}, p) - \dot{m}_{\text{d}} \quad (4.39)$$

is calculated from the saturated opening width of the valve slide and the mass flow necessary to compensate the influence of a varying volume on the pressure.

According to the minimum degree condition [10], the degree $\deg(A_w(z))$ is set to $\deg(R_p(z)) = \deg(S_p(z)) = \deg(T_p(z))$. Furthermore, the zeros of $A_w(z)$ must be placed inside the unit circle to guarantee stability of the closed pressure loop.

4.5.5. The Sensitivity to Modeling Errors of the Closed Pressure Control Loop

Like most controllers, also the pressure controller discussed in this chapter is designed on the base of a nominal model that only approximates the physical dependencies. In other words, an absolute correct model describing real world problems without assumptions, simplifications and without remaining modeling errors commonly does not exist but is mostly sufficient for designing a controller that fulfills all requirements. Nevertheless, one should be aware of the uncertainty every controller has to deal with and due to this

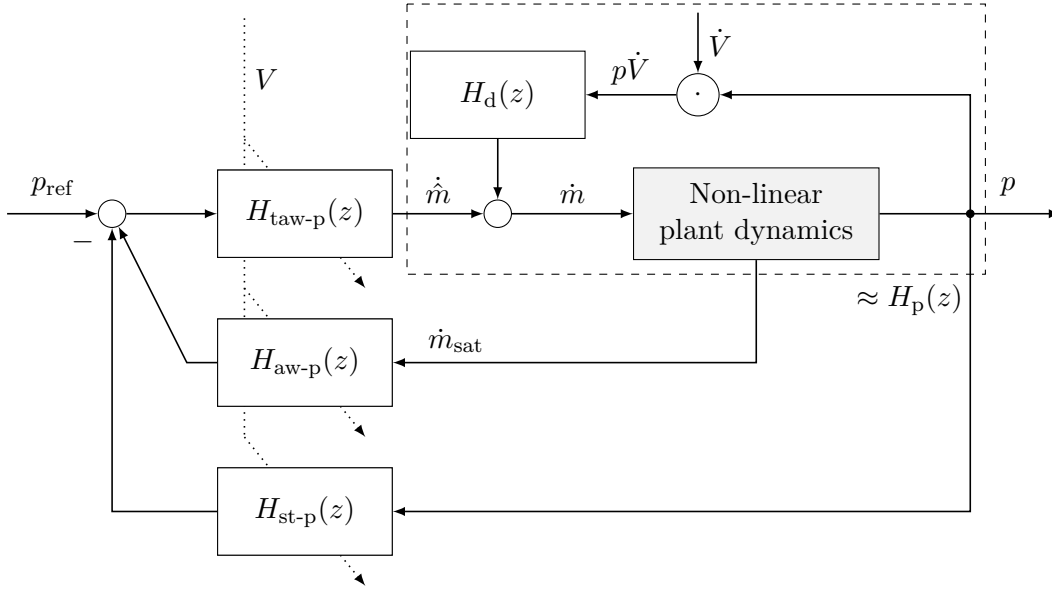


Figure 4.8.: Pressure controller with with integrator and anti-windup mechanism

it is common practice to check the closed control loop against its sensitivity to modeling errors during the design phase.

Besides amplitude and phase margin, the sensitivity function

$$\mathcal{S}_p = \frac{A_p R_p}{A_p R_p + B_p S_p} = \frac{1}{1 + \frac{B_p S_p}{A_p R_p}} \quad (4.40)$$

of the closed pressure control loop gives also a good measure of its sensitivity to modeling errors [10]. The inverse of its absolute value

$$\left| \frac{1}{\mathcal{S}_p(e^{i\omega})} \right| = \left| 1 + \frac{B_p(e^{i\omega}) S_p(e^{i\omega})}{A_p(e^{i\omega}) R_p(e^{i\omega})} \right| \quad (4.41)$$

represents the distance of the nyquist curve of the open loop to the critical point -1 for different angular frequencies ω . Since the robustness of the closed loop decreases with decreasing distance to the critical point -1 , i.e. its stability margin, the sensitivity provides information about the robustness of the closed loop. Based on their experience and as a rule of thumb, Åström and Wittenmark [10] (p.184 ff) are recommending to keep the distance of the nyquist curve of the open loop $|\mathcal{S}_p(e^{i\omega})| < 2 \forall \omega \geq 0$ to ensure a reasonable robustness against modeling errors. Accordingly, the nyquist curve of the open loop has at least a distance of $1/2$ to the critical point -1 . In the following, this rule of thumb is taken as the starting point for every pressure controller design and the robustness to modeling errors is checked by the analysis of the sensitivity function.

4.5.6. Bandwidth of the Torque Controller

As already noted, the torque controller consists of a purely algebraic torque-to-pressure conversion and two pressure controllers. Since only the pressure controllers are dynamical systems with a given bandwidth, the whole torque controller must have the same bandwidth as the pressure controllers. Due to this, the torque control loop can also be described as

$$H_{\text{cl-}\tau} = \frac{1 - P_c}{z - P_c}, \quad (4.42)$$

a first-order lag filter. As a result, the torque controlled PMA-driven joint can be treated as torque source with limited bandwidth.

4.6. Conclusion and Future Work

In this chapter, the characteristics of a PMA-driven joint under torque control were discussed in detail. As the most important result, it is shown that once the PMA-driven joint is torque-controlled, it is fully described by a static torque characteristic – the maximum torque range for every angle – and its bandwidth. Due to this, their integration into robotic systems and overlying controller designs is simplified because all characteristics of the PMAs, as well as the non-linear pressure dynamics, are handled by the torque controller internally. As a result, the PMA-driven joint can be treated as a torque source with a given bandwidth.

Besides its ability to control the joint torque, the torque controller enables a simultaneous variation of the torsional joint stiffness. This feature makes the PMA-driven joint a promising actuator for making robots safer – due to an increased compliance –, more animal- or human-like – since human beings and animals are adapting to changing tasks via a variation of body stiffness –, and lastly, more energy efficient. As an example, the energy efficiency of tasks like walking can be increased by exploiting the compliance of PMA-driven joints in a way that potential energy is stored and emitted periodically.

In future, it would be of interest to investigate how the torque characteristics and the joint stiffness can be shaped and adapted to a certain task, by a variation of the pulley radius on the one hand and by connecting both PMAs not only at mean but at any other combination of initial lengths on the other hand. Furthermore, this can be extended to PMA-driven joints with different PMAs, as discussed in Dirven and McDaid [30].

5. Pose Control of a Robot with 1 DOF and a PMA-driven Joint

In this section, an angular position controller for an exemplary robot with one degree of freedom will be designed. The controller design will follow a strictly arranged procedure of

1. defining the control task (Sec. 5.2),
2. designing the torque controller for every PMA-driven joint in accordance with the requirements of the control task (Sec. 5.3), and
3. designing the motion controller in accordance with the requirements of the control task (Sec. 5.4).

This procedure is independent of the degrees of freedom and applicable to every robot with PMA-driven joints, as will be demonstrated in this chapter for a 1 DOF and in the next chapter for a 2 DOF robot.

Since the 1 DOF robot of this chapter represents the simplest robot, a couple of effects will be reviewed in addition to the given control task. Firstly, the influence of the chosen torque controller with PM or FIT converter will be investigated. It will be shown that both torque controller variants are leading to slightly different results with respect to the tracking error. Secondly, the influence of a hysteresis compensation will be investigated, where the hysteresis model developed in Sec. 3.4.2 will be employed.

For the following chapter, it must be mentioned that the terms *motion controller*, *angle controller*, and *pose controller* are used synonymously. Furthermore, some of the results were already published by the author in

M. Martens, T. Seel, J. Zawatzki, and I. Boblan. A novel framework for a systematic integration of pneumatic-muscle-actuator-driven joints into robotic systems via a torque control interface. In *Actuators*, volume 7, page 82. Multidisciplinary Digital Publishing Institute, 2018 .

5.1. A System Description

The 1 DOF robot arm depicted in Fig. 5.1 is actuated by a PMA-driven joint. It consists of two Festo DMSP-20-300 that are connected to a pulley with radius $R = 23.24$ mm. The pressure inside both PMAs is controlled with a Festo MPYE-5-1/8-LF-010-B proportional servo valve. The available supply pressure is $p_s = 6$ bar. While the inner PMA pressure is measured with two Festo SPTE-P10R-S4-V-2.5K pressure sensors, the pulley angle is measured with a *KMA 210* angle sensor (NXP Semiconductors N.V., Eindhoven, The Netherlands). A load mass of 1.25 kg emulates a second robot link, extending the number of degrees of freedom, or a load that the robot could pick up and place somewhere else, respectively. The target control platform is a MicroDAQ E2000 (Embedded Solutions, Ropczyce, Poland), which can be programmed via a MATLAB (R2015b, The MathWorks, Inc., Natick, MA, USA) Simulink toolbox.

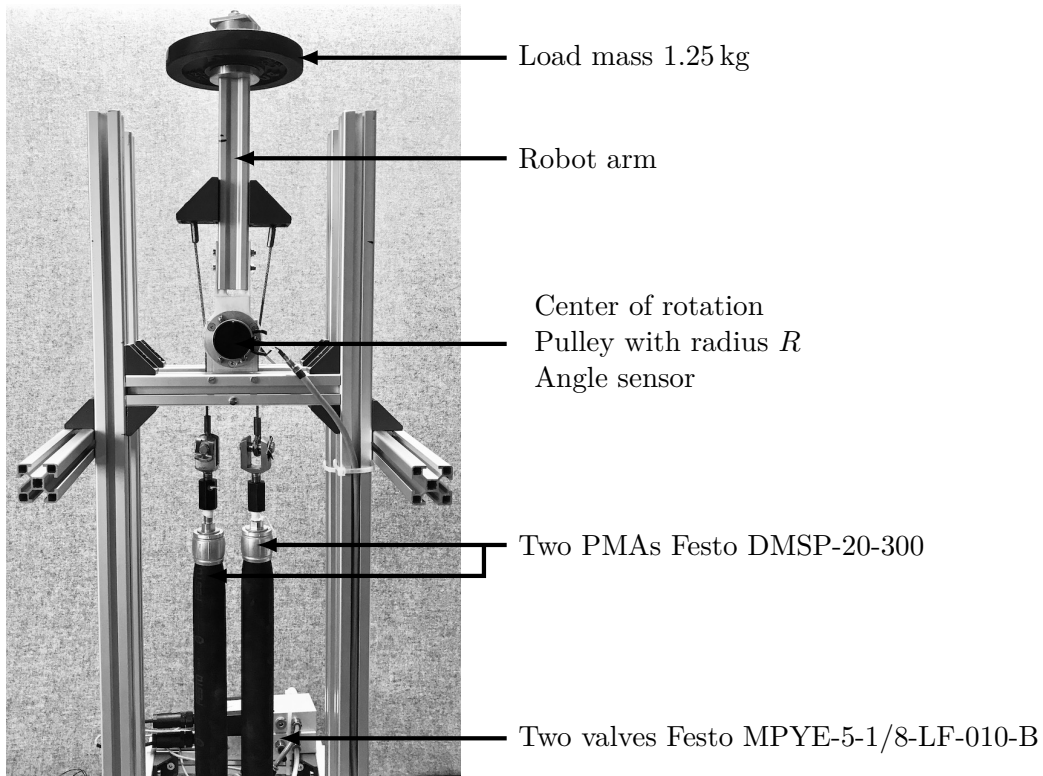


Figure 5.1.: Robot arm with PMA-driven joint and 1-DOF

As can be found in (2.19), the inverse dynamics describing the 1 DOF robotic arm, depicted in Fig. 5.1 in an upright position, is given by

$$\tau = \frac{mgl_s}{\omega_0^2} \left[\ddot{\varphi} + 2\delta\dot{\varphi} - \omega_0^2 \sin \varphi \right], \quad (5.1)$$

where φ represents the joint angle, τ the joint torque, m the mass of the only one link, and l_s the arm length. The eigenfrequency ω_0 as well as the damping factor δ were determined as $\omega_0 = 6.1995 \text{ s}^{-1}$ and $\delta = 0.025439 \text{ s}^{-1}$ by analyzing the oscillation of the robotic arm around the stable equilibrium in the hanging position. Furthermore, the arm mass with additional load mass is $m = 1.672 \text{ kg}$, and the distance from the center of rotation to the arm center of mass is $l_s = 246.1 \text{ mm}$. The acceleration due to gravity g is 9.81 ms^{-2} .

5.2. Definition of the Reference Angle Trajectory and Discussion of its Feasibility

Before an angular position controller can be designed for the present robot arm, it must be clarified what task the robot has to fulfill. For this particular robot – due to the lack of a real use case –, the artificial control goal is formulated as follows: The robot plus its additional load should follow the trajectory defined in Fig. 5.2a. Due to this, the robot rotates at $\pm 40^\circ$ around the upright position. Furthermore, this angle trajectory defines an angular velocity (Fig. 5.2b) and an angular acceleration trajectory. These trajectories were all calculated with the *tpoly* function from the *Robotics Toolbox* [27, 25, 26], an open source toolbox for MATLAB by Peter Corke. The angle φ_d in Fig. 5.2a is provided in degrees. All calculations use the angle $\varphi = \pi/180 \cdot \varphi_d$.

Since the angle as well as its first and second time-derivative are known, the required torque can be calculated from the robots inverse dynamics (5.3). The required torque can be seen in Fig. 5.2c and its time derivative is given in Fig. 5.2d.

The information provided by Fig. 5.3 defines the requirements the torque-controlled PMA-driven joint has to fulfill. Firstly, the torque for every angle of the desired angle trajectory (Fig. 5.2c) describes the absolute torque value for every position, and this can only be provided by the PMA-driven joint as long as the torque is inside the valid torque range defined by its torque characteristics, as shown in Fig. 4.4. For this robot, the maximum torque of 3.0258 Nm must be provided at $\pm 40^\circ$ and gets smaller towards the upright position, where it becomes zero.

Secondly, the maximum of the time derivative of the torque defines the minimum bandwidth that the torque controller has to have. The maximum torque time derivative in Fig. 5.2d is 11.35 Nm/s at 21.6 s . Since the time derivative is similar to an angular velocity, the related "torque" frequency is calculated as $11.35/2\pi = 1.81 \text{ Hz}$. This frequency is not equal to the torque controller bandwidth but defines the required torque frequency range for the specific trajectory and the related task of the robot. Since the torque controller behaves like a first-order lag filter, the requirement of a loss-free signal transmission can be guaranteed by setting the controller cut-off frequency at least one decade higher, i.e. the required controller cut-off frequency is set to 18.1 Hz .

Lastly, the angular velocity $\dot{\varphi}_d$ (Fig. 5.2b) provides similar information about the required frequency range of the position controller. The maximum absolute angular

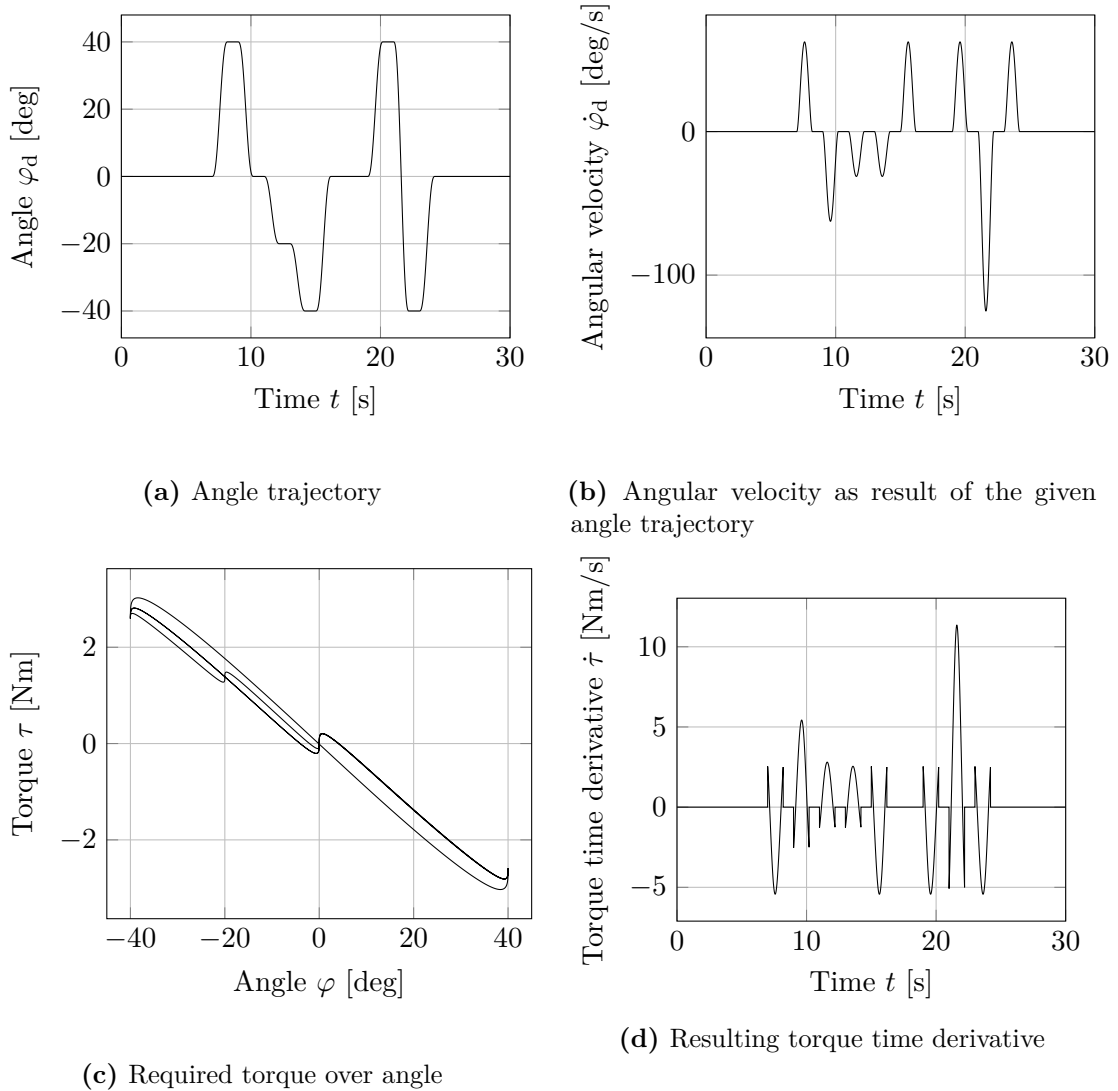


Figure 5.2.: Desired angle trajectory the 1 DOF robot should follow

velocity is -125 deg/s at 21.6 s (see Fig. 5.2b). By changing the measuring unit from degree to radian, the maximum angular velocity becomes -2.18 rad/s. The related frequency is 0.35 Hz. For this controller, the cut-off frequency should be also set at least one decade higher, i.e. it should be at least 3.5 Hz.

With this information at hand, the torque controller for the PMA-driven joint will be designed in Sec. 5.3 and included into a motion controller design in Sec. 5.4.

5.3. Inner Torque Control Loop

In accordance with Sec. 5.1, the present robot arm is actuated by two Festo DMSP-20-300. By combining them with a pulley with a radius of $R = 23.24$ mm and a supply pressure of $p_s = 6$ bar, the angle range is limited to $\pm 97^\circ$, i.e. it includes the desired angle trajectory of $\pm 40^\circ$, defined in the previous Sec. 5.2. Furthermore, both PMAs are connected at half contraction. This configuration is defined by a specific overlay of their respective force maps and shapes the torque range at which the PMA-driven joint is able to exert. As can be seen in Fig. 5.3 (black dashed line), the maximum torque of about 15 Nm is right in the middle for the PM torque control approach, while it is at the edges of the FIT torque control approach. It must be noted that the FIT converter is used with an initial force of $F_{IT} = 0.15 \max(F_{PMA})$. This value is chosen through experimental testing.

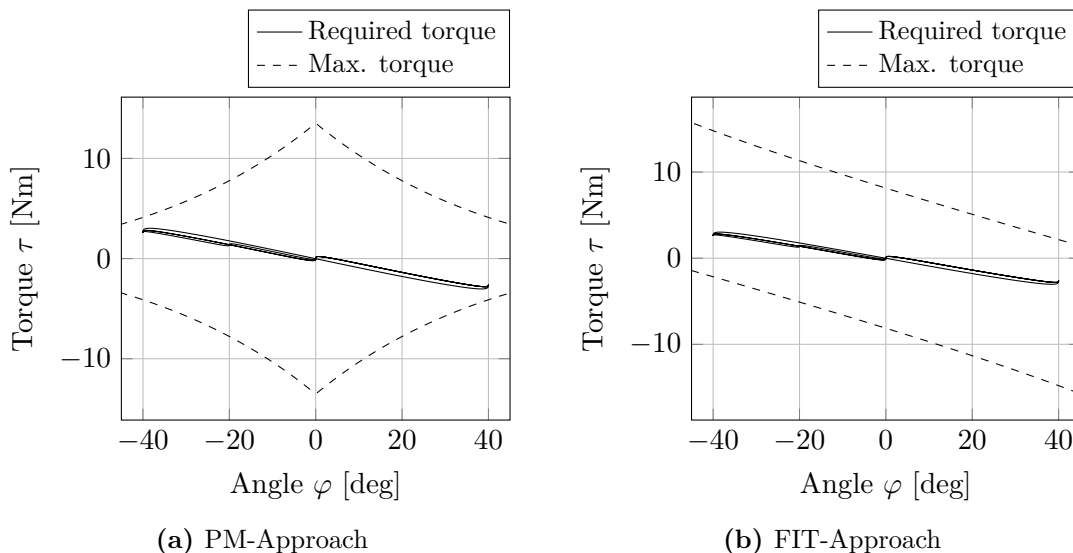


Figure 5.3.: Torque characteristic of the 1-DOF robot

The black line in Fig. 5.3 represents the torque that is needed to follow the desired angle trajectory defined in Sec. 5.2 and is the same as shown in Fig. 5.2c. Due to this, the chosen PMA-driven joint – two Festo DMSP-20-300 and a pulley with radius of $R = 23.24$ mm – and its configuration – both PMAs connected at half contraction – provides enough torque to make the robot follow the desired trajectory. Furthermore, the choice of the torque converter, PM or FIT, is of no importance, since the desired torque trajectory is inside both torque ranges.

As depicted in Fig. 4.2, the torque controller consists of two similar pressure controllers and an algebraic torque-to-pressure conversion. In accordance with Sec. 4.5.6, the bandwidth of the torque controller only depends on the bandwidth of its pressure

controllers, i.e. only by tuning the pressure controllers, the required torque control bandwidth of 18.1 Hz can be reached.

Since positioning the robot does not require a precise but a fast pressure controller, it is designed as a gain scheduling pressure controller without integral action, as described in Sec. 4.5.3. The pressure controller design is carried out by setting the controller pole to 20 Hz $>$ 18.1 Hz. The closed-loop pressure dynamics can be described in the discrete-time domain by the first-order lag filter

$$H_{\text{cl-p}} = \frac{1 - 0.8819}{z - 0.8819}, \quad (5.2)$$

where the pole is calculated as $P_c = e^{-2\pi T_s 20\text{Hz}} = 0.8819$ (see (4.32) from Sec. 4.5.3) for the chosen sampling frequency of 1 kHz. Furthermore, the observer poles are placed at 40 Hz, 48 Hz, 56 Hz, 64 Hz, 72 Hz, 80 Hz, and 88 Hz. Due to the occurrence of disturbances at isolated frequencies, the further pressure controller design is carried out by canceling the influence of measurement noise. Beside signals at the Nyquist frequency, signals with frequencies of 101.5 Hz, 203.67 Hz, 272 Hz, 305.67 Hz, and 408 Hz also get suppressed by the controller, as frequency folding occurs otherwise. Since the pressure controller should adapt to the time-varying PMA volume, the controller design is repeated for 10 different volumes, which are chosen equidistantly within $\bar{V} \in [V(L_0), V(0.7L_0)]$. Since multiple pressure controllers are designed for different volumes following the same requirements, the closed-loop dynamics $H_{\text{cl-p}}$ as well as the closed-loop sensitivity \mathcal{S}_p (see Sec. 4.5.5) are equivalent for every controller-volume pair. Due to this, Fig. 5.4 is representative for the whole gain scheduling pressure controller. The sensitivity fulfills $\mathcal{S}_p \leq 1.4$, and therefore, the closed loop can be considered reasonable robust [10].

To prove the functionality of the torque controller, the robot arm is fixed in an upright position and screwed to a force sensor $KD40s \pm 2kN$ (ME-Meßsysteme GmbH, Hennigsdorf). The measured force signal is amplified by a *GSV-1A* measurement amplifier (ME-Meßsysteme GmbH, Hennigsdorf) and multiplied with a lever arm of 200 mm, so that the exerted torque of the PMA-driven joint in this position becomes measurable. This position represents the center of the angle range, i.e. $\varphi = 0$, and both PMAs are at their mean length of 260.6 mm. The whole measurement setup can be seen in Fig. 5.5a.

During the measurement, the PMA-driven joint was following a sine torque trajectory with an amplitude of 5 Nm and frequencies of 0.5 Hz, 1 Hz, 2 Hz, 5 Hz, 10 Hz and 20 Hz. All amplitudes of the exerted torque, as well as the reference of 5 Nm, are depicted in Fig. 5.5b. The black line shows the measured torque amplitude of a torque controller with a FIT converter and an initial force of 15 % of the maximum PMA force, while the blue line shows the torque amplitude of a torque controller with a PM converter and $s_{\text{pmc}} = 0.5$.

At first, it might seem surprising that both control approaches have a cut-off frequency of about 10 Hz, which is slightly below the desired cut-off frequency. However, it turned

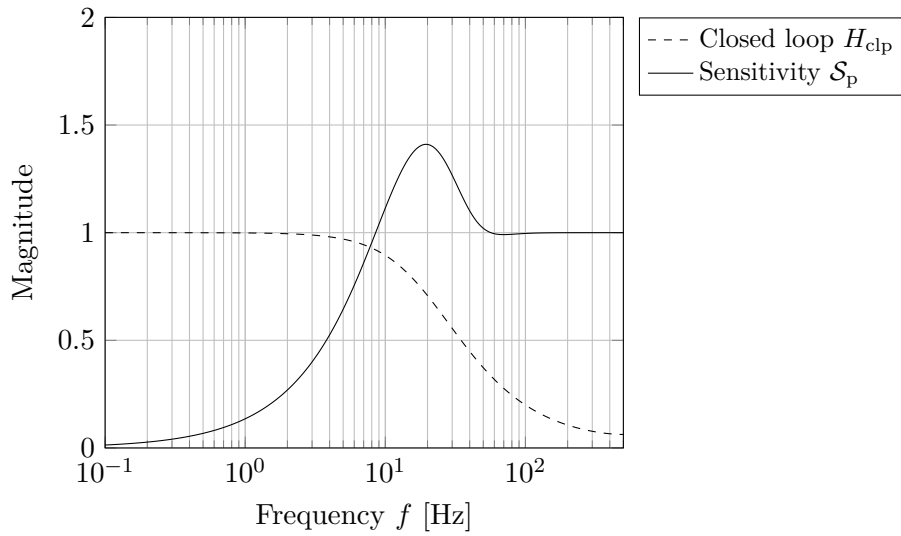
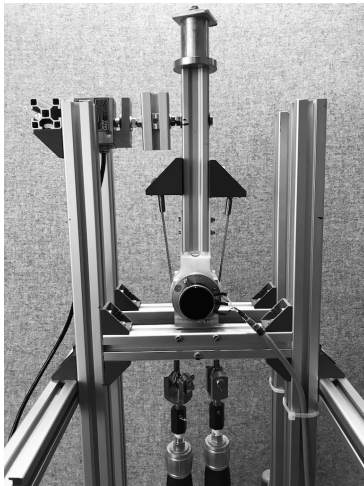
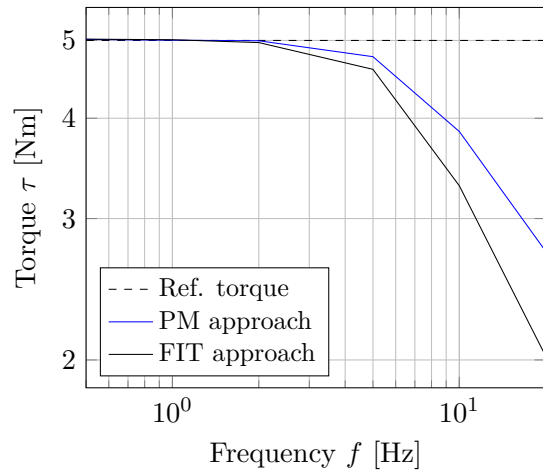


Figure 5.4.: Robot with 1 DOF - Magnitude of the closed pressure loop H_{clp} and its sensitivity S_p



(a) Torque measurement setup. The robot arm is fixed in an upright position and screwed to a force sensor.



(b) Torque amplitude of a sinus torque trajectory the PMA-driven joint exerts for different frequencies

Figure 5.5.: Torque measurement setup and measured torque data for different frequencies

out by measurement that this cut-off frequency corresponds with the bandwidth of the pressure controllers. Furthermore, the bandwidth of the pressure controller is mostly limited by the deflation process. Nevertheless, as Fig. 5.5b shows, both torque controllers can guarantee a loss-free torque signal transmission of up to 2 Hz, so that the

requirement of a nearly loss-free torque transmission of 1.81 Hz, defined in Section 5.2, is fulfilled.

In addition, it can be seen that the cut-off frequency of the PM controller is slightly higher in comparison with the FIT controller. A reasonable explanation for this can be found in the way that the pressure trajectories are generated: Depending on whether the torque is positive or negative, the FIT controller only varies one pressure, while the other one is kept constant. In contrast to this, the PM controller always varies both pressures at the same time for exerting a given torque trajectory.

In conclusion, it can be stated that both torque controllers have a sufficiently high bandwidth, i.e. treating them as pure torque sources is justified for the following motion controller design.

5.4. Outer Angular Position Controller

The equation of motion of the present 1 DOF robot

$$\ddot{\varphi} = \frac{\omega_0^2}{mgl_s} \left[\tau - \left(2\delta \frac{mgl_s}{\omega_0^2} \dot{\varphi} - mgl_s \sin \varphi \right) \right], \quad (5.3)$$

represents its dynamics, i.e. the evolution of φ and $\dot{\varphi}$ over time, and can be used for deriving the state-space model. Thereby the vector $(\varphi, \dot{\varphi})^T$ represents the state of the robot and the control torque τ represents the system input.

By defining the system output as $y = \varphi$, all state variables

$$\varphi = y \quad (5.4)$$

$$\dot{\varphi} = \dot{y} \quad (5.5)$$

as well as the input

$$\tau = \frac{mgl_s}{\omega_0^2} \left(\ddot{y} + 2\delta \dot{y} - \omega_0^2 \sin y \right) \quad (5.6)$$

are defined only by the chosen output and its time derivatives. Likewise, it can be said that the system is differentially flat and the output φ is one flat output of the system [2] (p.209, Def. 27).

Due to the flat system characteristic, the control torque is chosen to

$$\tau_{\text{ref}} = \underbrace{\frac{mgl_s}{\omega_0^2} \left(\ddot{\varphi}_{\text{ref}} + 2\delta \dot{\varphi}_{\text{ref}} - \omega_0^2 \sin \varphi_{\text{ref}} \right)}_{=:\tau_{\text{ff}}} + \underbrace{\frac{mgl_s}{\omega_0^2} f(e_\varphi, \dot{e}_\varphi)}_{=:\tau_{\text{fb}}} \quad e_\varphi = \varphi - \varphi_{\text{ref}} \quad (5.7)$$

which can be subdivided into a feedforward controller τ_{ff} – represented by the inverted equation of motion – and a feedback controller τ_{fb} stabilizing the system. The control structure is shown in Fig. 5.6.

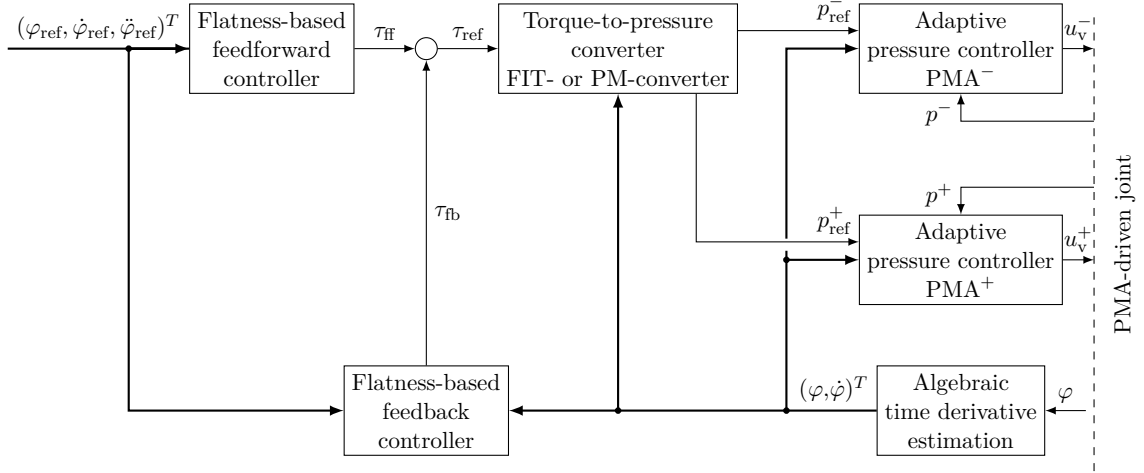


Figure 5.6.: Flatness-based control architecture to stabilize the angle of a 1 DOF robot with PMA-driven joint

By setting $\tau = \tau_{\text{ref}}$ in Eq. (5.6), the controller (5.7) yields an error dynamics of the controlled system as

$$\ddot{e}_\varphi + 2\delta\dot{e}_\varphi - \omega_0^2 \cos \varphi_{\text{ref}} e_\varphi - f(e_\varphi, \dot{e}_\varphi) = 0, \quad (5.8)$$

which can be stabilized by

$$f(e_\varphi, \dot{e}_\varphi) = -\omega_0^2 \cos \varphi_{\text{ref}} e_\varphi - K_p e_\varphi - K_d \dot{e}_\varphi - K_i \int e_\varphi dt. \quad (5.9)$$

By inserting (5.9) into (5.8), the error dynamics of the closed control loop

$$\ddot{e}_\varphi + (2\delta + K_d)\dot{e}_\varphi + K_p e_\varphi + K_i \int e_\varphi dt = 0 \quad (5.10)$$

is a differential equation of third order. By transforming the resulting error dynamics to the frequency domain, the poles of the characteristic polynomial

$$s^3 + (2\delta + K_d)s^2 + K_p s + K_i = 0 \quad (5.11)$$

can be placed arbitrarily through a variation of the controller gains K_p , K_i , and K_d . Next, the characteristic equation is separated into one conjugate-complex pole pair and a third pole on the real axis. For the sake of stability, the real part of all three poles is kept strictly negative. Stability as well as further requirements can be specified by defining a desired error dynamics

$$(s^2 + 2\delta_{12}s + \omega_{12}^2)(s + \omega_3) = 0, \quad (5.12)$$

to which the original error dynamics (5.11) can be transformed by comparing the co-efficients of (5.11) and (5.12). The resulting controller gains are

$$\begin{aligned} K_d &= 2\delta_{12} + \omega_3 - 2\delta \\ K_p &= \omega_{12}^2 + 2\delta_{12}\omega_3 \\ K_i &= \omega_{12}^2\omega_3. \end{aligned}$$

Through iterative hardware-in-the-loop testing, the parameters of the desired error dynamics were finally set to $\omega_{12} = 10.2041 \text{ s}^{-1}$, $\delta_{12} = 1.0204 \text{ s}^{-1}$, and $\omega_3 = 10.2041 \text{ s}^{-1}$. Accordingly, the bandwidth of the closed angle control loop is set to 1.62 Hz. For higher frequencies, the controller gets closer to the edge of stability and its robustness gets poorer. Due to this, the chosen controller bandwidth is a trade-off between controller speed on the one hand and robustness on the other hand.

The occurrence of instability, caused by too high controller gain, is well known and according to Lynch and Park [47], this is constituted by "practical issues such as actuator saturation, undesired rapid torque changes (chattering) or vibrations of the structure due to unmodeled flexibility in the joints and links" ([47], p.424).

5.5. Experimental Investigation of the Trajectory Following Behavior

The presented cascade-structured angle controller is tested by experimental investigation of its ability to follow the angle trajectory defined in Section 5.2. The chosen flatness-based controller always needs, in addition to the reference angle, its first and second time derivatives. Therefore, the reference trajectory is calculated so that it guarantees a continuous time evolution of the angle, the angular velocity, and the angular acceleration. Fig. 5.7 shows the defined reference angle trajectory and the tracking behavior of the presented angle controllers. While Fig. 5.7a shows the angle tracking behavior with an underlying joint torque controller with a PM converter, Fig. 5.7b shows the angle tracking performance with the same flatness-based angle controller, but with a FIT converter. While $s_{\text{pmc}} = 0.5$ for the PM converter (see Section 4.3.2), the initial force of the FIT converter is set to $F_{\text{IT}} = 0.15 \max(F_{\text{PMA}})$ by experimental testing.

On the left of Fig. 5.7, the trajectory as well as the system angle are almost identical, and this is independent of the chosen torque controller. The error e_φ is almost the same for both torque control approaches and only minor differences can be noticed. While the maximum error is at about 4° , the error seems to be generally a little rougher for the FIT torque controller than for the torque controller with a PM converter. In other words, the PM controller reacts a little bit faster such that control errors can be counteracted a little better in comparison to the FIT controller. This correlates with the slightly higher bandwidth of the PM torque controller (see Fig. 5.5). Nevertheless, both

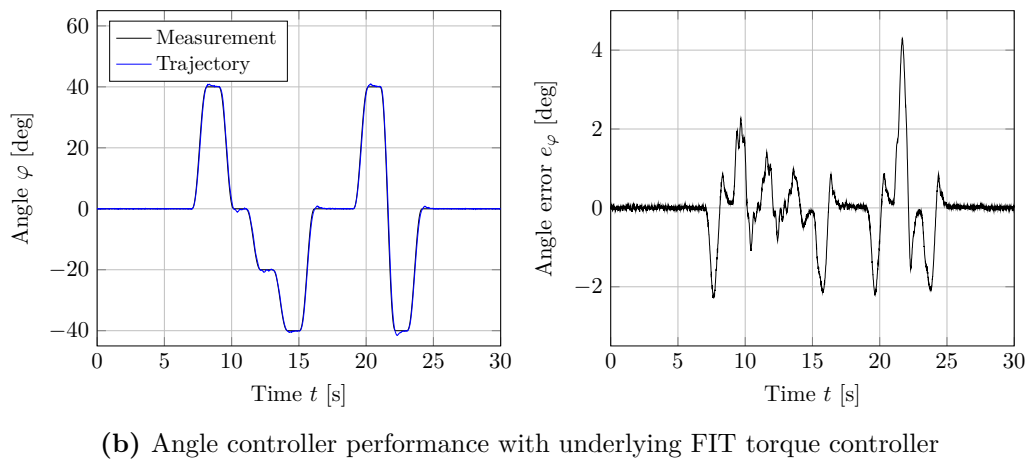
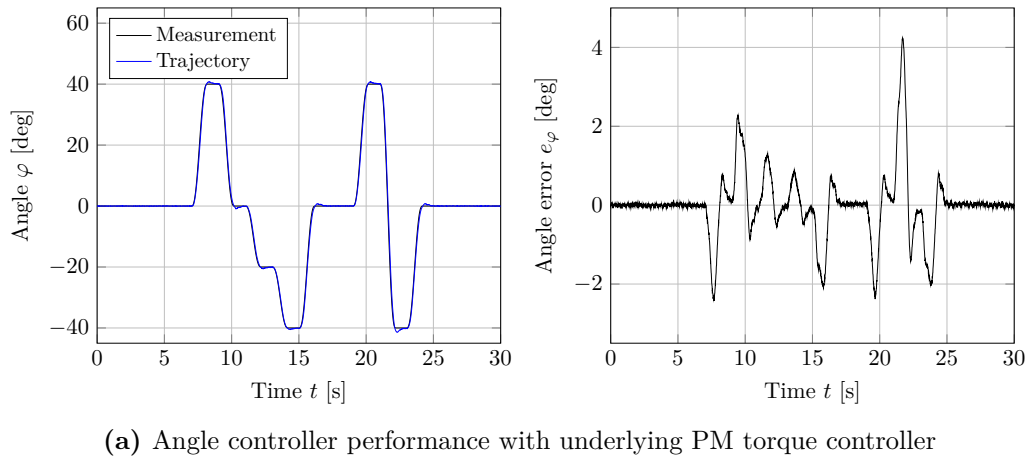


Figure 5.7.: Angle controlled, 1 DOF robot arm is following a given angle trajectory

torque control approaches lead to excellent results. Furthermore, the motion controller is designed almost without knowledge of the PMA-driven joint or the pressure controllers. Due to this, both torque controllers are masking the challenging characteristics of a PMA-driven joint, i.e. they are behaving as a simple interface for the present overlying motion controller. This simplifies the controller design enormously and fills the gap between PMAs on the one hand and robotics on the other hand.

5.6. Experimental Investigation of the Influence of Hysteresis Compensation

In Section 3.4.2, it is demonstrated that the hysteresis of the PMA can be modeled by the Maxwell-Slip model. Furthermore, it is shown in Section 3.5 that the model-based

force prediction gets significantly improved by taking not only the PMA static but also its hysteresis force into account.

In accordance with (4.1), the force difference of the PMA hysteresis forces (3.26) defines a hysteresis torque as

$$\tau_{\text{Hyst}} = R \left[F_{\text{Hyst}}^+ - F_{\text{Hyst}}^- \right], \quad (5.13)$$

which is treated as disturbance acting on the plant. In this section, the hysteresis will be compensated by additional feedforward control, and the reference torque

$$\hat{\tau}_{\text{ref}} = \tau_{\text{ref}} - \tau_{\text{Hyst}} \quad (5.14)$$

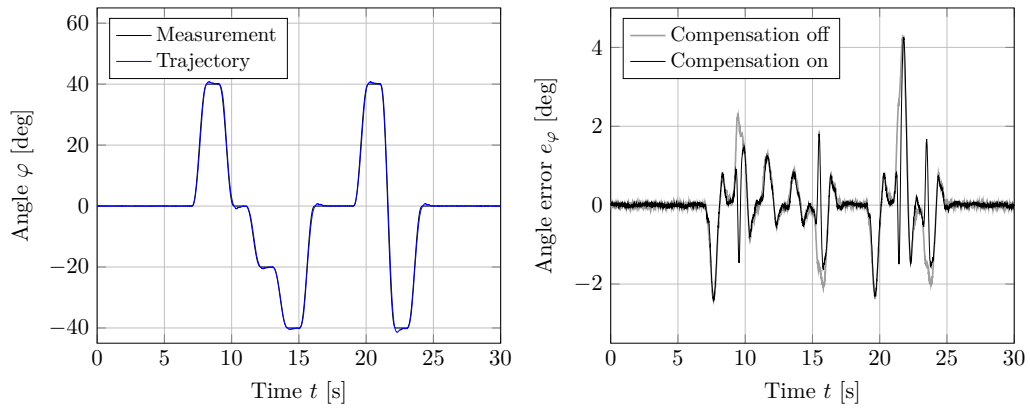
is extended by the hysteresis torque with opposite sign. In Fig. 5.8, the desired angle trajectory is once again shown in black. The blue line represents the real angle of the robot, while it follows the given trajectory. In contrast to the previous section, the controller (5.7) is replaced by (5.14). On the right side, the error e_φ is depicted respectively in black, with hysteresis compensation, and in gray, without.

As demonstrated in Section 3.5, the PMA force can be modeled more precisely with a hysteresis than without it. Nevertheless, the improvement of the angle tracking error is hardly significant. Especially the maximum error at 21.6 s remains almost unaffected. The most significant improvement of the hysteresis compensation can be found at 9 s in the right graph of Fig. 5.8a, where the angle error is reduced by approximately one degree. At last, it can be seen that the error plot is slightly smoother with hysteresis compensation, especially in the rest positions, where the error is almost zero.

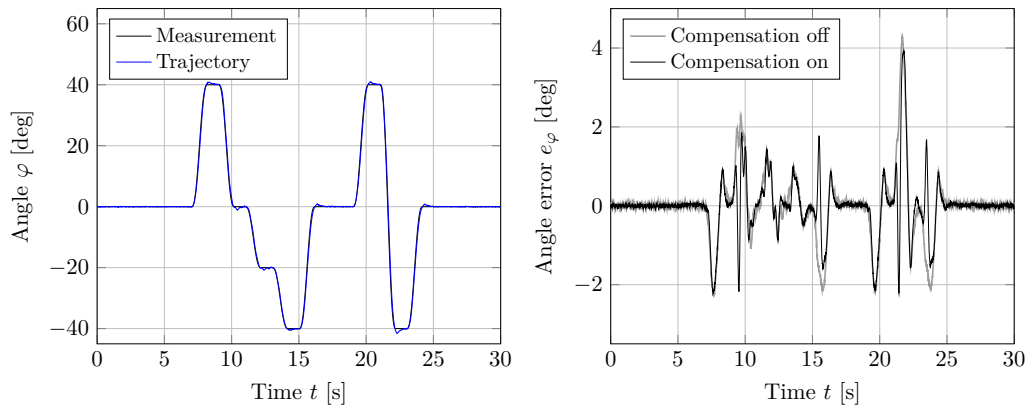
5.7. Conclusion

Since PMAs are highly non-linear, they have a rather bad reputation and are often excluded in the decision process of finding suitable actuators for different robotic applications. To simplify their application to robotic systems in this chapter, an exemplary 1 DOF robot with PMA-driven joint was controlled by a flatness-based motion controller, designed without taking into account the characteristics of the PMA-driven joint but treating it as a pure torque source. Ignoring most of the characteristics of the PMA-driven joint is enabled because they are hidden behind a torque control interface that handles their challenging characteristics internally. The advantage of this torque-control-interface structure is emphasized by the excellent tracking behavior that was obtained in the experiment. Since the present robot has only one degree of freedom, the question remains if the same control structure is suitable for a multi-dimensional robot. The answer will be given in the next chapter, where a 2 DOF robot with PMA-driven joints will be controlled in an equal manner.

As a further result of this chapter, it can be stated that the tracking performance is mostly unaffected by the chosen torque controller, regardless of whether a PM or



(a) Angle controller performance with underlying PM-approach torque controller, with and without additional hysteresis compensation



(b) Angle controller performance with underlying FIT-approach torque controller, with and without additional hysteresis compensation

Figure 5.8.: Influence of a hysteresis torque compensation to the angle tracking performance of a 1 DOF robot with PMA-driven joint

FIT converter was used. A hysteresis compensation does not improve the tracking performance significantly either. Due to this, a compensation of hysteresis will be renounced for the following chapter.

6. Pose Control of a Robot with 2 DOF and PMA-driven Joints

In the previous chapter, it has been demonstrated that the pose of a robot with one DOF and PMA-driven joint can be controlled precisely with an overlying flatness-based position controller and an underlying torque controller. Furthermore, the overlying motion controller is directly connected to the PMA-driven joints via a torque control interface like it is described in Section 4. Due to this, the PMA-driven joint can be treated as a pure torque source with limited bandwidth.

On the one hand, the 1 DOF robot of the previous chapter represents a good example to investigate the PMA-driven joint itself and its performance within a position controller. On the other hand, a robot with only one DOF does not provide the complexity of a multi-dimensional robot. Hence, it cannot be clarified how a torque controlled PMA-driven joint performs in higher-dimensional robotic systems. Due to this, a planar robot with two DOF and two PMA-driven joints will be investigated in this chapter. Similar to the controller for the 1 DOF robot, every torque of the PMA-driven joints within this controller design will be controlled separately, and only the overlying motion controller will be designed as a global – multiple-input-multiple-output (MIMO) – controller.

In accordance with the procedure introduced at the very beginning of Chapter 5, the requirements for both – joint torque and position – will be defined in Section 6.3 for the present robot by a desired control task that the robot should fulfill. Afterwards, both joint torques will be controlled by individual torque controllers in Section 6.4. In the end, the robot will be controlled by a MIMO backstepping controller in Section 6.5, which is extended by a disturbance torque observer to make the robot follow the desired joint angle trajectories precisely. In Section 6.8, the dynamical system and thus the controller is extended by a time-delayed torque signal. This improves the robustness in cases in which the cut-off frequency is too low for being neglected.

6.1. A System Description

The planar robot depicted in Fig. 6.1 has two degrees of freedom, hence it is a combination of two rigid links that are connected by two revolute joints. While the first joint – the base joint – connects the fixed surrounding – the base – and the first link, the second

joint – the elbow joint – connects the first and the second link right in the middle of the robot. Although it is not present yet, in future it is planned to add an end effector at the free end – the tip – of the robot, so that the manipulation of objects becomes possible. Due to this, the positioning of the robot and the positioning the tip of the robot will be used synonymously within this chapter.

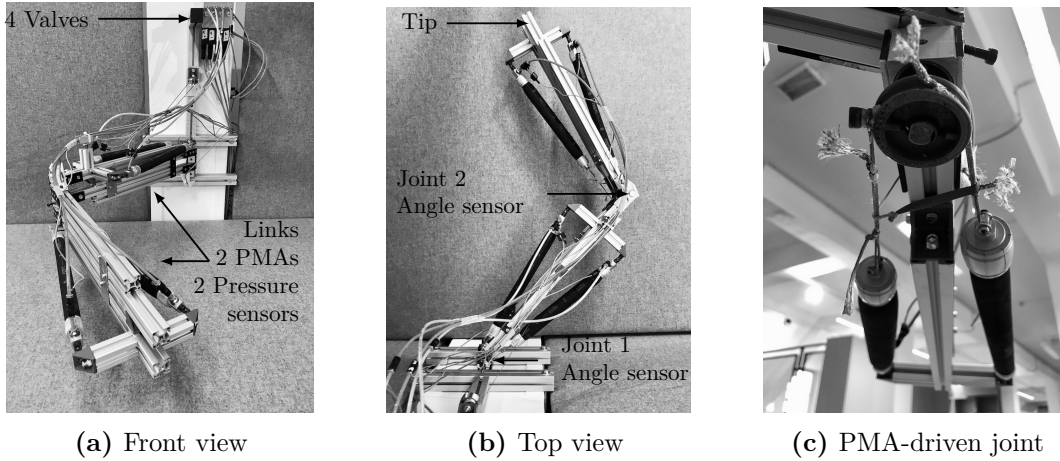


Figure 6.1.: Planar robot with 2 DOF and PMA-driven joints

Both links are actuated by a PMA-driven joint that can rotate the next link around the previous joint. Thereby, both PMA-driven joints are driven by the same PMA type, a Festo DMSP-20-353, that is connected to the pulley at half-contraction. In contrast to the 1 DOF robot of the previous chapter, the PMA-driven joints of the present 2 DOF robot are constructed in a way that keeps the pulley (see Fig. 6.1c) fixed to the previous link while the actuated link rotates around it. Accordingly, the first pulley is coupled rigidly to the non-moving base and the second pulley is fixed to the first link.

Since controlling the robot's position requires feedback signals of the PMA pressures and joint angles, the robot is equipped with four Festo SPTE-P10R-S4-V-2.5K pressure sensors – one for each PMA – and off-the-shelf potentiometers for both joint angles. The chosen valves are Festo MPYE-5-1/8-LF-010-B. The real-time target platform is a *Speedgoat Baseline real-time target machine* (Speedgoat GmbH, Liebfeld, Switzerland), which is programmed by a MATLAB (R2015b, The MathWorks, Inc., Natick, MA, USA) Simulink toolbox.

6.2. Model

The 2 DOF robot, as explained in Section 2.2.3, is defined by its equation of motion

$$\frac{d}{dt} \begin{pmatrix} \varphi \\ \dot{\varphi} \end{pmatrix} = \begin{pmatrix} \dot{\varphi} \\ M^{-1}(\varphi) [\tau - h(\varphi, \dot{\varphi})] \end{pmatrix}, \quad (6.1)$$

Table 6.1.: Constant parameters for the 2 DOF robot extracted from CAD data by Johannes Zawatzki (Research assistant at the Beuth Hochschule für Technik Berlin)

Link i	m_i	l_i	l_{s_i}	$\Theta_i^{(S_i)}$
1	3.6 kg	0.637 m	0.265 m	0.181 564 kgm ²
2	3.6 kg	0.637 m	0.265 m	0.181 564 kgm ²

where the state $(\varphi, \dot{\varphi})^T \in \mathbb{R}^4$, with $\varphi = (\varphi_1, \varphi_2)^T$ and $\dot{\varphi} = (\dot{\varphi}_1, \dot{\varphi}_2)^T$, is defined by all joint angles and angular velocities. The joint torque vector $\tau \in \mathbb{R}^2$ represents the system input. Furthermore, the inertia-representing mass matrix

$$M(\varphi) = \begin{pmatrix} \Theta_1^{(S_1)} + \Theta_2^{(S_2)} + m_1 l_{s_1}^2 + m_2 (l_1^2 + l_{s_2}^2 + 2l_1 l_{s_2} \cos \varphi_2) & \Theta_2^{(S_2)} + m_2 (l_{s_2}^2 + l_1 l_{s_2} \cos \varphi_2) \\ \Theta_2^{(S_2)} + m_2 (l_{s_2}^2 + l_1 l_{s_2} \cos \varphi_2) & \Theta_2^{(S_2)} + m_2 l_{s_2}^2 \end{pmatrix} \quad (6.2)$$

with $M(\varphi) \in \mathbb{R}^{2 \times 2}$ is symmetric, positive definite and invertible, and

$$h(\varphi, \dot{\varphi}) = \begin{pmatrix} -m_2 l_1 l_{s_1} \sin \varphi_2 [\dot{\varphi}_2 (\dot{\varphi}_1 + \dot{\varphi}_2) + \dot{\varphi}_1 \dot{\varphi}_2] \\ m_2 l_1 l_{s_1} \dot{\varphi}_1^2 \sin \varphi_2 \end{pmatrix} \quad (6.3)$$

with $h(\varphi, \dot{\varphi}) \in \mathbb{R}^{2 \times 1}$ lumps together all centrifugal and Coriolis effects [47]. Since the robot only moves in a plane that is perpendicular to gravity, h is free of any influence of gravity.

The robot is further defined by a set of constant parameters, like the link masses $m_{1,2}$, the link lengths $l_{1,2}$, the position of each link center of gravity $S_{1,2}$ defined by the distance from the previous joint l_{s_1, s_2} , and the inertia $\Theta_{1,2}^{(S_{1,2})}$ with respect to the center of gravity of link one or two, respectively. The present robot was designed by Johannes Zawatzki at the Beuth Hochschule für Technik Berlin with *Inventor* (Autodesk GmbH, München), a computer aided design (CAD) program made for product development. Furthermore, Johannes Zawatzki extracted all constant parameters, as can be found in Tab. 6.1, from the CAD model of the robot.

6.3. Definition of the Desired Angle Trajectory and Discussion of its Feasibility

In accordance with the 1 DOF robot from the previous chapter, the control task for the 2 DOF robot is also defined arbitrarily, since the 2 DOF robot is a first prototype and more a case study than a task-fulfilling robot. The angle trajectories, defined by the fictitious control task, are taken as a reference to measure the performance of the controller. As an exemplary task, the robot should follow a given angle trajectory, like it is given in Fig. 6.2a. In detail, joint 2 rotates from 0° to -70° , and from -70° to 70° , while joint angle 1 is kept constant at 0° . Afterwards, only joint 1 rotates from

0° to -70° , while joint 2 is kept constant at 70° . In the end, both joints are rotating simultaneously back to their initial position of 0° via detours.

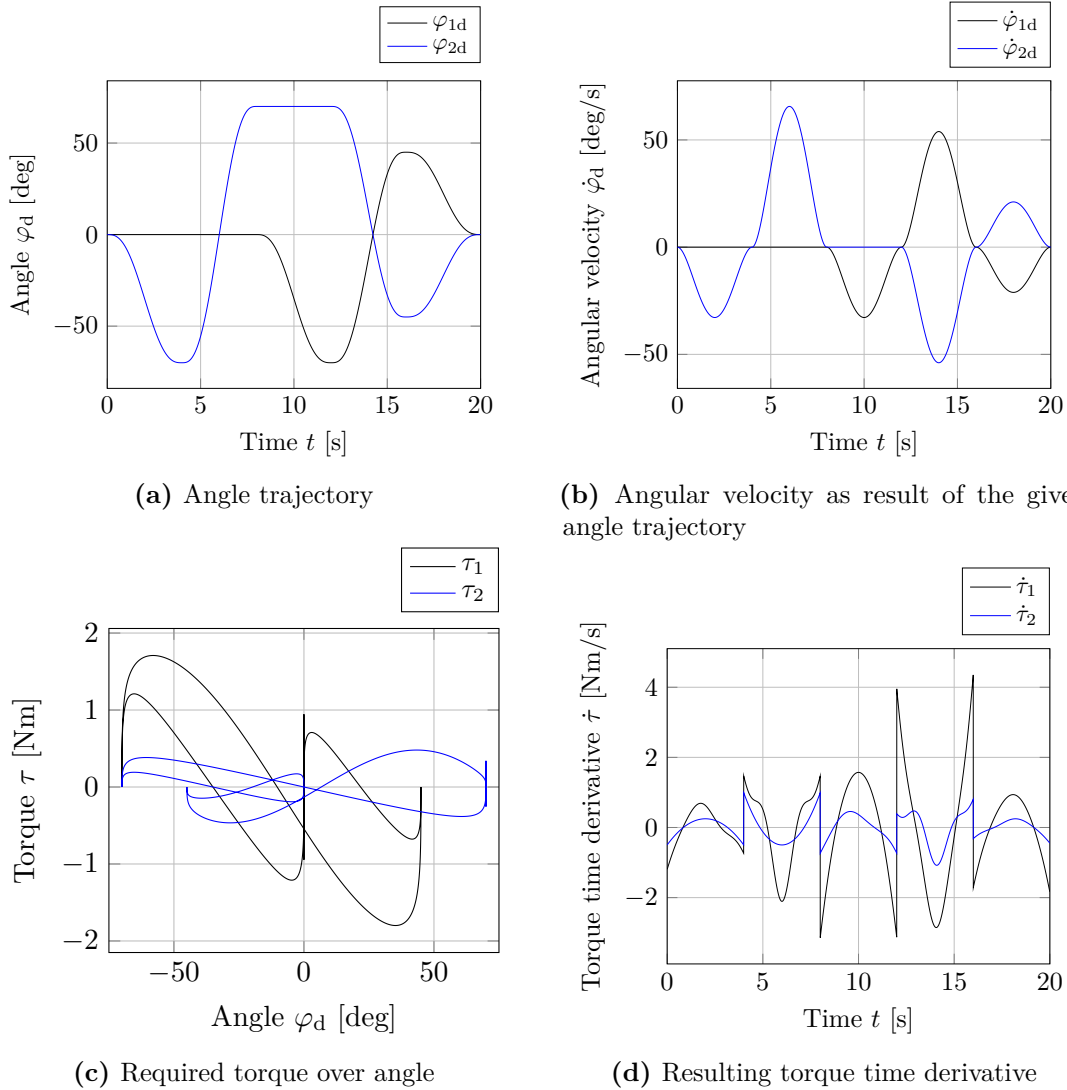


Figure 6.2.: Desired angle trajectory the 2 DOF robot should follow

As can be seen, the control task is defined in the joint space of the robot. However, this is no loss of generality because a path defined in xy -coordinates can be easily transformed to φ -coordinates by the inverse kinematics of the robot – in case of a 2 DOF robot –, as in Lynch and Park [47] (p.219 ff). It must be mentioned that this transformation is not unique but depends on the decision whether the elbow joint should be on the left or right side.

The given control task crucially defines the requirements for both the underlying joint torque controllers and the overlying position controller. In the sense of a bottom-up

approach, the requirements for the torque controller will be identified with the joint torque for every joint angle – a result of the inverse dynamics – Fig. 6.2c and the first time derivative of the given torque trajectory 6.2d. At first, the static torque the PMA-driven joint has to provide for every joint angle, is given in Fig. 6.2c. While the black curve represents the base joint torque τ_1 , the blue line defines the elbow joint torque τ_2 . Thereby, the maximum torque of the elbow joint is only 0.48 Nm, and the maximum joint torque of the base joint is 1.71 Nm and is always higher than the elbow joint torque. This is quite reasonable, since the base joint always carries the load of both links. As a result, it can be stated that the PMA-driven base joint must provide higher torques than the second – the elbow – PMA-driven joint.

In contrast to the static torque analysis, Fig. 6.2d gives an information about the required bandwidth of the torque controller. In accordance with the previous chapter, the time derivative of the torque will be treated as the "torque angular frequency", i.e. the maximum torque frequency that can be calculated by a division of 2π from Fig. 6.2d. Furthermore, torques with frequencies up to the maximum frequency should be transmitted without losses, and this is guaranteed if the cut-off frequency of the torque controllers is at least one decade higher. Due to this, the minimum required torque controller bandwidth is 7 Hz for the base and 1.6 Hz for the elbow joint, respectively.

Since the requirements for the underlying torque controller are identified, the focus is now set to the requirements for the overlying joint angle controller which makes the robot reach a desired pose or follow a desired angle trajectory. The requirement for this controller can be identified as the desired angular velocity, as depicted in Fig. 6.2b. In accordance with the torque controller bandwidth, the maximum angular velocity is calculated as its related frequency and multiplied by 10, so that the given angle trajectory can pass without losses. As a result, the cut-off frequency of the base joint angle controller has to be at least 1.5 Hz and greater or equal than 1.8 Hz for the elbow joint, to fulfill the required control task.

6.4. Design of the Inner Torque Controller

In accordance with the requirements defined in the previous section, the torque controller has to provide a certain torque to be able to follow the given path. Motivated by the tracking performance of the 1 DOF robot from the previous chapter, the torque controller with a PM converter ($s_{\text{pmc}} = 0.5$) is chosen for both PMA-driven joints of the present robot. Fig. 6.3 shows the maximum torque range (black dashed lines) of a PMA-driven joint, with two DMSP-20-353 connected at half-contraction and a pulley radius of 16 mm. The black line in Fig. 6.3 shows the required joint torque of the base joint, and the blue line the required torque of the elbow joint.

As shown, the static characteristic of the chosen PMA-driven joint with a PM converter is able to provide enough torque and has, in addition, a reasonable torque reserve to handle non-modeled system behavior and uncertainties.

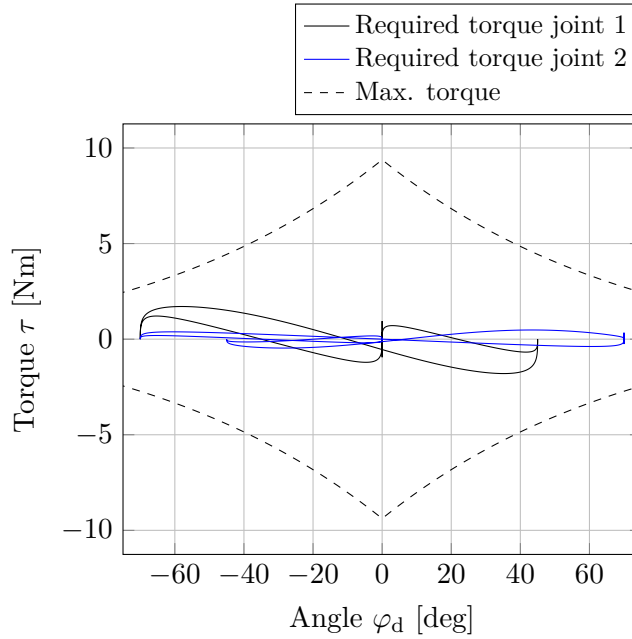


Figure 6.3.: Required torque to follow the desired trajectory for joint 1 and 2, respectively

Besides their static characteristics, the PMA-driven joints have to follow their individual trajectory up to a given frequency without losses to guarantee a perfect tracking behavior. The maximum bandwidth was identified as 7 Hz beforehand. For the sake of safety, the cut-off frequency of the gain scheduling pressure controller is set to 16 Hz, so that the closed pressure loop – theoretically – behaves like the first-order lag filter

$$H_{cl-\tau} = \frac{1 - 0.8819}{z - 0.8819}. \quad (6.4)$$

It should be mentioned that this cut-off frequency is not reached by the real system, as it will be explained later in this chapter.

6.5. Pose Control

Both PMA-driven joints of the robot are now torque controlled and, since the bandwidth is sufficiently high, will be treated – at first – as pure torque sources. To make the robot follow the desired path, an overlying position controller is needed. The robot's equation of motion (6.1) is a non-linear MIMO system and motivates the design of a non-linear controller. The chosen controller for this chapter is a higher-order *backstepping controller*, as explained in Khalil and Grizzle [42]. It should be mentioned that the chosen backstepping control approach is an arbitrary choice, and it is very likely that another, non-linear, control approach like a model-predictive or sliding-mode controller,

could lead to good results, too. Although not implemented in this thesis, this could be included in future work.

6.5.1. Backstepping Controller without Time-delayed Torque Signals

As mentioned before, the bandwidth of the torque controller is set to 16 Hz and therefore, as a first approach, the PMA-driven joints are treated as pure torque sources, i.e. the torques can be taken as the direct system input. For the sake of a good trajectory tracking, the equation of motion (6.1) is slightly reformulated to

$$\frac{d}{dt} \begin{pmatrix} x_\varphi \\ \dot{x}_\varphi \end{pmatrix} = \frac{d}{dt} \begin{pmatrix} e_\varphi \\ \dot{e}_\varphi \end{pmatrix} = \begin{pmatrix} \dot{e}_\varphi \\ M^{-1}(\varphi) [\tau - h(\varphi, \dot{\varphi})] - \ddot{\varphi}_d \end{pmatrix} = \begin{pmatrix} \mathbf{f}_1(e_\varphi) + \mathbf{h}_1(e_\varphi)\dot{e}_\varphi \\ \mathbf{f}_2(e_\varphi, \dot{e}_\varphi) + \mathbf{h}_2(e_\varphi, \dot{e}_\varphi)\tau \end{pmatrix}, \quad (6.5)$$

with a tracking error $e_\varphi = (e_{\varphi 1}, e_{\varphi 2})^T = \varphi - \varphi_d \in \mathbb{R}^{2 \times 1}$, its time derivative $\dot{e}_\varphi = \dot{\varphi} - \dot{\varphi}_d \in \mathbb{R}^{2 \times 1}$, and the new system state $x_\varphi = (e_\varphi, \dot{e}_\varphi)^T \in \mathbb{R}^{4 \times 1}$. The reformulation of the system dynamics enables a stabilization of the angle error instead of the angle, i.e. the error converges to zero although the reference angle is varying. The system (6.5) has a strict feedback form [2], i.e.

$$\mathbf{f}_1(e_\varphi) = (0, 0)^T \quad (6.6)$$

$$\mathbf{h}_1(e_\varphi) = \mathbf{I}_2 \quad (6.7)$$

$$\mathbf{f}_2(e_\varphi, \dot{e}_\varphi) = -M^{-1}h - \ddot{\varphi}_d \quad (6.8)$$

$$\mathbf{h}_2(e_\varphi, \dot{e}_\varphi) = M^{-1}, \quad (6.9)$$

whereby a backstepping controller design becomes applicable [42]. The backstepping controller design follows in two steps: Firstly, only the first sub-system of (6.5) is stabilized by

$$\mathbf{f}_1(e_\varphi) + \mathbf{h}_1(e_\varphi)\dot{e}_\varphi = \dot{e}_\varphi \stackrel{!}{=} -e_\varphi =: \alpha(e_\varphi), \quad (6.10)$$

where the controller $\alpha(e_\varphi) := -e_\varphi$ enables a stabilization of the first sub-system in accordance to Lyapunov's stability theorem ([42], p. 114, Theorem 4.1). The Lyapunov function is

$$\mathcal{V}_1(e_\varphi) = e_\varphi^T \begin{pmatrix} k_{v1} & 0 \\ 0 & k_{v2} \end{pmatrix} e_\varphi = k_{v1}e_{\varphi 1}^2 + k_{v2}e_{\varphi 2}^2 \quad k_{v1,2} \in \mathbb{R}^+ \setminus \{0\} \quad (6.11)$$

and is $> 0 \forall e_\varphi \neq 0$. Furthermore, its time derivative

$$\dot{\mathcal{V}}_1 = \frac{\partial \mathcal{V}_1}{\partial e_\varphi} \dot{e}_\varphi \quad (6.12)$$

$$= \begin{pmatrix} 2k_{v1}e_{\varphi 1} & 2k_{v2}e_{\varphi 2} \end{pmatrix} \begin{pmatrix} -e_{\varphi 1} \\ -e_{\varphi 2} \end{pmatrix} \quad (6.13)$$

$$= -(2k_{v1}e_{\varphi 1}^2 + 2k_{v2}e_{\varphi 2}^2) < 0 \quad \forall e_\varphi \neq 0 \quad (6.14)$$

is negative definite. Consequently, (6.10) stabilizes the first sub-system [42, 38]. Secondly, in accordance with Khalil and Grizzle [42] (p. 589 ff), the controller is designed as follows

$$\tau = \mathbf{h}_2^{-1} \left(\frac{\partial \alpha}{\partial e_\varphi} (\mathbf{f}_1 + \mathbf{h}_1 \dot{e}_\varphi) - \left(\frac{\partial \mathcal{V}_1}{\partial e_\varphi} \mathbf{h}_1 \right)^T - \begin{pmatrix} k_1 & 0 \\ 0 & k_2 \end{pmatrix} [\dot{e}_\varphi - \alpha] - \mathbf{f}_2 \right) \quad k_1, k_2 \in \mathbb{R}^+ \setminus \{0\}. \quad (6.15)$$

By inserting \mathbf{f}_1 , \mathbf{f}_2 , \mathbf{h}_1 , \mathbf{h}_2 , α , $\frac{\partial \alpha}{\partial e_\varphi}$ and $\frac{\partial \mathcal{V}_1}{\partial e_\varphi}$, the controller is

$$\tau = M \left(-\dot{e}_\varphi - \begin{pmatrix} 2k_{v1}e_{\varphi 1} \\ 2k_{v2}e_{\varphi 2} \end{pmatrix} - \begin{pmatrix} k_1 & 0 \\ 0 & k_2 \end{pmatrix} [\dot{e}_\varphi + e_\varphi] - M^{-1}h + \ddot{\varphi}_d \right). \quad (6.16)$$

This controller is able to stabilize the angle error, i.e. the controlled system is able to follow a time-varying joint angle trajectory. Accordingly, the stability of the whole system in the sense of Lyapunov is ensured. Furthermore, the Lyapunov function of the closed loop is [42]

$$\mathcal{V}_2(e_\varphi, \dot{e}_\varphi) = e_\varphi^T \begin{pmatrix} k_{v1} & 0 \\ 0 & k_{v2} \end{pmatrix} e_\varphi + \frac{1}{2} (\dot{e}_\varphi + e_\varphi)^2. \quad (6.17)$$

6.5.2. Disturbance Torque Observer

The backstepping controller (6.16) stabilizes the error dynamics but does not provide any integral action. Due to this, the error will not vanish completely in case of an occurrence of input disturbances. To counteract quasi-static input disturbances and to improve the tracking accuracy, the controller is extended by a disturbance torque observer, which is motivated by the disturbance torque observer of Schindele and Aschemann [62] for a 1 DOF system.

The estimation of the disturbance torque gets enabled by extending the error dynamics

$$\frac{d}{dt} \begin{pmatrix} x_\varphi \\ \dot{x}_\varphi \end{pmatrix} = \frac{d}{dt} \begin{pmatrix} e_\varphi \\ \dot{e}_\varphi \end{pmatrix} = \begin{pmatrix} \dot{e}_\varphi \\ M^{-1}(\varphi) [(\tau - \tau_u) - h(\varphi, \dot{\varphi})] - \ddot{\varphi}_d \end{pmatrix} \quad (6.18)$$

, as previously seen in (6.5), through a torque $\tau_u \in \mathbb{R}^{2 \times 1}$ disturbing the input signal τ .

In accordance to the ideas of Schindele and Aschemann [62], it is assumed that the estimated disturbance torque $\hat{\tau}_u$ behaves in accordance with the dynamical system

$$\hat{\tau}_u = Kx_\varphi + \psi \quad (6.19)$$

$$\dot{\psi} = \Phi(x_\varphi, \hat{\tau}_u, \tau), \quad (6.20)$$

with $K = k \begin{pmatrix} I_2 & M(\varphi) \end{pmatrix} \in \mathbb{R}^{2 \times 4}$ and $k \in \mathbb{R}$. $\psi \in \mathbb{R}^{2 \times 1}$ represents the state of the dynamical system. Furthermore, it is assumed that the disturbance torque is quasi-static, i.e. $\tau_u = \text{const.}$. Due to this, the estimation error

$$\dot{e}_\tau = \dot{\tau}_u - \dot{\hat{\tau}}_u \xrightarrow{\tau_u = \text{const.}} \dot{e}_\tau = -\dot{\hat{\tau}}_u \quad (6.21)$$

is only defined by the evolution of $\hat{\tau}_u$.

The major goal of the disturbance torque observer is the estimation of the disturbance torque, i.e. $e_\tau = 0$, especially at steady state. Due to this, it can be useful to investigate the time-derivative of the torque error at steady state, i.e. $\dot{e}_\tau = 0$. The error dynamics at steady state is

$$0 = -\dot{\hat{\tau}}_u \quad (6.22)$$

$$0 = -\dot{K}x_\varphi - K\dot{x}_\varphi - \Phi(x_\varphi, \hat{\tau}_u, \tau) \quad (6.23)$$

$$0 = -k\dot{M}\dot{e}_\varphi - k\dot{e}_\varphi - kM \left(M^{-1} [(\tau - \hat{\tau}_u) - h] - \ddot{\varphi}_d \right) - \Phi(x_\varphi, \hat{\tau}_u, \tau). \quad (6.24)$$

By re-arranging this equation the calculation of

$$\Phi(x_\varphi, \hat{\tau}_u, \tau) = -k\dot{M}\dot{e}_\varphi - k\dot{e}_\varphi - kM \left(M^{-1} [(\tau - \hat{\tau}_u) - h] - \ddot{\varphi}_d \right) \quad (6.25)$$

becomes possible. As a result, the observers (6.19) or (6.20) are fully determined, and the error dynamics is

$$\dot{e}_\tau = -\dot{K}x_\varphi - K\dot{x}_\varphi - \Phi(x_\varphi, \hat{\tau}_u, \tau) \quad (6.26)$$

$$\begin{aligned} &= -k\dot{M}\dot{e}_\varphi - k\dot{e}_\varphi - kM \left(M^{-1} [(\tau - \tau_u) - h] - \ddot{\varphi}_d \right) \\ &\quad + k\dot{M}\dot{e}_\varphi + k\dot{e}_\varphi + kM \left(M^{-1} [(\tau - \hat{\tau}_u) - h] + \ddot{\varphi}_d \right) \end{aligned} \quad (6.27)$$

$$= -k(\tau - \tau_u) + k(\tau - \hat{\tau}_u) \quad (6.28)$$

$$= k(\tau_u - \hat{\tau}_u) \quad (6.29)$$

$$= ke_\tau, \quad (6.30)$$

where the time derivative of the mass matrix is given as

$$\dot{M} = \begin{pmatrix} -2m_2l_1l_{s2}\dot{\varphi}_2 \sin \varphi_2 & -m_2l_1l_{s2}\dot{\varphi}_2 \sin \varphi_2 \\ m_2l_1l_{s2}\dot{\varphi}_2 \sin \varphi_2 & 0 \end{pmatrix}. \quad (6.31)$$

The error dynamics and thus the observers are asymptotically stable for $k < 0$. Due to its stability, the estimated disturbance torque can be added to the controller torque in a feed-forward manner without destabilizing the closed loop dynamics. Since this compensates quasi-static input disturbances like parameter deviations or Coulomb friction, the controlled system will act mostly independent of such disturbances, and the tracking error is decreasing.

6.6. Experimental Investigation of the Pose Controller

The arbitrarily chosen control task is defined in Section 6.3. Furthermore, both joints of the 2 DOF robot are torque-controlled, as described in Section 6.4. It is shown that both joint torque controllers provide a reasonable torque range to fulfill the control task successfully. In addition, their bandwidth is sufficiently high.

The backstepping pose controller without a torque disturbance observer designed in the previous section, is tuned so that the error dynamics of the base and elbow joints are corresponding to a second-order low pass filter. The cut-off frequencies are chosen as $f_{co1} = 1.8$ Hz respectively $f_{co2} = 2$ Hz. The damping is set to $d_1 = 0.48$ for the base and $d_2 = 0.4$ for the elbow joint. The resulting controller gains are $k_1 = 11.38$, $k_2 = 9.97$, $k_{v1} = 77.41$, and $k_{v2} = 89.01$. Only for controllers with disturbance torque compensation the observer gain is set to $k = -0.63$ by experimental testing.

The trajectory tracking performance of the 2 DOF robot, in combination with the presented backstepping controller without an additional disturbance observer, is shown in Fig. 6.4 as black lines. The blue lines are representing the same backstepping controller but with the extension of the presented torque disturbance observer. For the sake of clarity, the measured trajectories for joint 1 and 2 are depicted separately in Fig. 6.4a and 6.4b, respectively.

Before the measurement data can be interpreted correctly, it must be noted that the base joint pulley was not completely fixed during all measurements but loose to some extent. Since the controller design is carried by the assumption of a fixed base pulley, the system sometimes gets close to its stability margin when the pulley starts moving relatively. Furthermore, measuring and compensating the effects of the relative moving base pulley is not possible with reasonable effort, so that this drawback must be accepted. Nevertheless, the measurement results are demonstrating that the chosen backstepping controller represents a suitable solution to make the present robot fulfill the control task successfully. Starting with the backstepping controller without a torque disturbance compensation (black lines), it stands out that the error is smaller than 3° for the base joint and smaller than 8° for the elbow joint, respectively. This can be seen in the angle error plot Fig. 6.4a and 6.4b. This error is further decreased by adding the estimated disturbance torque to the control torque signal with an opposite sign. The effect of the disturbance torque compensation can be seen especially in the time ranges around 0 s, 30 s, and 45 s, where the error is significantly smaller with compensation. During these

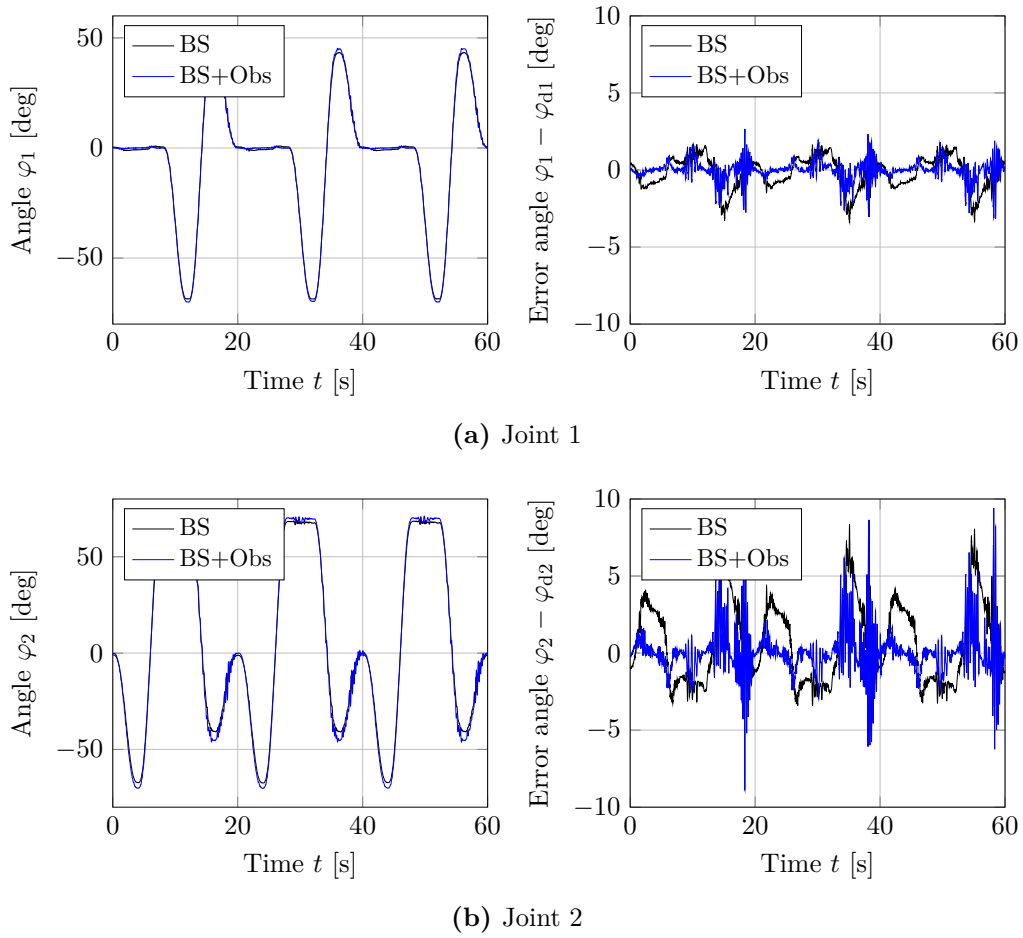


Figure 6.4.: Backstepping controller tracking performance with and without additional disturbance torque observer

time spans, the base pulley was standing still. The disturbance of the blue curve at 18 s, 38 s, and 58 s can be explained by a visible jittering of the base joint pulley around its axis that occurs particularly at these times. Interesting to see is that link 2 is affected more by the loose base pulley than link 1, but this can be explained by the unfavorable lever ratio.

6.7. An Interim Conclusion

In general, the chosen backstepping control approach leads to promising results. The robot follows the desired trajectory with high accuracy. Furthermore, it is shown that, if perfect trajectory tracking or accurate position control is required, model uncertainties as well as other input disturbances can be compensated by adding a torque disturbance

compensation. Thereby, the disturbance can be estimated through a disturbance torque observer.

While running the tests of the backstepping controller, two major problems were occurring frequently: Firstly, the loose base joint pulley seemed to destabilize the system, which is reasonable since the base joint pulley is the major support location for the whole robot and must be fixed for a proper power transmission. Since the loose pulley could not be fixed and a compensation through feedback signals was not possible either – the jittering is hardly measurable with reasonable effort –, this problem must be accepted for this thesis.

Secondly, the robot sometimes got close to the edge of stability while the base joint pulley was standing still. By simulation it could be seen that, in case the bandwidth of the first order lag filter delaying the input torque signals is too low, this caused unstable system behavior. In accordance with Section 4.5.6, the torque control bandwidth equals the pressure controller bandwidth of the PMAs. By measuring the pressure frequency response of a single PMA, it was shown that, although theoretically set to 16 Hz, the real pressure controller cut-off frequency was only at 4 Hz. Thereby, the deflation of the PMA especially limited the bandwidth of the pressure controller. Due to this, the dynamics of the closed torque control loop was not negligible any more but had to be included into a proper motion controller design. To overcome this problem, the next section will provide a backstepping controller for a robot with time-delayed torque inputs.

6.8. Pose Control with Time-delayed Torque Inputs

As mentioned above, the cut-off frequency of the torque controller with which both PMA-driven joints are controlled is much lower than expected and thus non-negligible. Due to this, the system dynamics (6.1) is extended in this section by a first-order lag filter, i.e. the input torque signals are getting delayed.

6.8.1. Backstepping Controller

In accordance with Section 4.5.6, the torque signal, calculated by the motion controller, is not directly transmitted by the PMA-driven joint but transmitted with a delay of a first-order low pass filter with a given bandwidth. Depending on the bandwidth and the dynamics of the robot, the time delay can be either neglected or must be taken into account. In case the bandwidth of the torque controller is too low, the dynamics of the

robotic system (6.1) must be extended to

$$\frac{d}{dt} \begin{pmatrix} \tilde{x}_\varphi \end{pmatrix} = \frac{d}{dt} \begin{pmatrix} e_\varphi \\ \dot{e}_\varphi \\ \tau \end{pmatrix} = \begin{pmatrix} M^{-1}(\varphi) [\tau - h(\varphi, \dot{\varphi})] - \ddot{\varphi}_d \\ \frac{1}{T_\tau} \mathbf{I}_2 (\tau_c - \tau) \end{pmatrix} = \begin{pmatrix} \tilde{\mathbf{f}}_1(x_\varphi) + \tilde{\mathbf{h}}_1(x_\varphi) \tau \\ \tilde{\mathbf{f}}_2(x_\varphi, \tau) + \tilde{\mathbf{h}}_2(x_\varphi, \tau) \tau_c \end{pmatrix}, \quad (6.32)$$

where the torque driving the robot τ and the control torque τ_c are no longer equivalent. The time constant T_τ represents the bandwidth of the torque controllers with which both PMA-driven joints are controlled. The new state $(\tilde{x}_\varphi) \in \mathbb{R}^{6 \times 1}$ is a composition of the state of the system without time-delayed torque signals from (6.1) and the torque vector τ . Furthermore, the factors $\tilde{\mathbf{f}}_1 \in \mathbb{R}^{4 \times 1}$, $\tilde{\mathbf{h}}_1 \in \mathbb{R}^{4 \times 2}$, $\tilde{\mathbf{f}}_2 \in \mathbb{R}^{2 \times 1}$, and $\tilde{\mathbf{h}}_2 \in \mathbb{R}^{2 \times 2}$ are defined as

$$\tilde{\mathbf{f}}_1 = \begin{pmatrix} \mathbf{f}_1 + \mathbf{h}_1 \dot{e}_\varphi \\ \mathbf{f}_2 \end{pmatrix} \quad (6.33)$$

$$\tilde{\mathbf{h}}_1 = \begin{pmatrix} \mathbf{0}_2 \\ \mathbf{h}_2 \end{pmatrix} \tau \quad (6.34)$$

$$\tilde{\mathbf{f}}_2 = -\frac{1}{T_\tau} \mathbf{I}_2 \tau \quad (6.35)$$

$$\tilde{\mathbf{h}}_2 = \frac{1}{T_\tau} \mathbf{I}_2. \quad (6.36)$$

Since the new system dynamics (6.32) is only an extension of (6.1), the backstepping controller (6.16) can be re-used as the base for the design of a backstepping controller for the extended system with time-delayed torques. By defining the control torque from (6.16) as

$$\tilde{\alpha}(x_\varphi) := \tau = M \left(-\dot{e}_\varphi - \begin{pmatrix} 2k_{v1}e_{\varphi 1} \\ 2k_{v2}e_{\varphi 2} \end{pmatrix} - \begin{pmatrix} k_1 & 0 \\ 0 & k_2 \end{pmatrix} [\dot{e}_\varphi + e_\varphi] - M^{-1}h + \ddot{\varphi}_d \right), \quad (6.37)$$

the controller for the extended system is [42] (p. 603)

$$\tau_c = \tilde{\mathbf{h}}_2^{-1} \left(\frac{\partial \tilde{\alpha}}{\partial x_\varphi} (\tilde{\mathbf{f}}_1 + \tilde{\mathbf{h}}_1 \tau) - \left(\frac{\partial \mathcal{V}_2}{\partial x_\varphi} \tilde{\mathbf{h}}_1 \right)^T - \begin{pmatrix} k_3 & 0 \\ 0 & k_4 \end{pmatrix} [\tau - \tilde{\alpha}] - \tilde{\mathbf{f}}_2 \right), \quad (6.38)$$

where the Lyapunov function \mathcal{V}_2 is taken from (6.17). Its derivative, with respect to the state x_φ , is given as

$$\frac{\partial \mathcal{V}_2}{\partial x_\varphi} = \begin{pmatrix} \frac{\partial \mathcal{V}_2}{\partial e_{\varphi 1}} & \frac{\partial \mathcal{V}_2}{\partial e_{\varphi 2}} & \frac{\partial \mathcal{V}_2}{\partial \dot{e}_{\varphi 1}} & \frac{\partial \mathcal{V}_2}{\partial \dot{e}_{\varphi 2}} \end{pmatrix} \quad (6.39)$$

$$= \left((2k_{v1} + 1)e_{\varphi 1} + \dot{e}_{\varphi 1} \quad (2k_{v2} + 1)e_{\varphi 2} + \dot{e}_{\varphi 2} \quad e_{\varphi 1} + \dot{e}_{\varphi 1} \quad e_{\varphi 2} + \dot{e}_{\varphi 2} \right). \quad (6.40)$$

The derivative of $\tilde{\alpha}(x_\varphi)$ Eq. (6.37), with respect to x_φ , is

$$\frac{\partial \tilde{\alpha}}{\partial x_\varphi} = \begin{pmatrix} \frac{\partial \tilde{\alpha}_1}{\partial e_{\varphi 1}} & \frac{\partial \tilde{\alpha}_1}{\partial e_{\varphi 2}} & \frac{\partial \tilde{\alpha}_1}{\partial \dot{e}_{\varphi 1}} & \frac{\partial \tilde{\alpha}_1}{\partial \dot{e}_{\varphi 2}} \\ \frac{\partial \tilde{\alpha}_2}{\partial e_{\varphi 1}} & \frac{\partial \tilde{\alpha}_2}{\partial e_{\varphi 2}} & \frac{\partial \tilde{\alpha}_2}{\partial \dot{e}_{\varphi 1}} & \frac{\partial \tilde{\alpha}_2}{\partial \dot{e}_{\varphi 2}} \end{pmatrix}. \quad (6.41)$$

For the sake of clarity, the derivatives of $\frac{\partial \tilde{\alpha}}{\partial x_\varphi}$ are provided in the Appendix A.2.

6.8.2. Disturbance Torque Observer

In accordance with the backstepping controller for the system without time-delayed torque signals, the backstepping controller for the extended system dynamics – due to a lack of integral action – does not have the ability to compensate input disturbances acting on the input torque τ . To match the desired pose or angle trajectory precisely, the backstepping controller for the system with time-delayed torque signals will be extended by a torque disturbance observer. The disturbed system is given as

$$\frac{d}{dt} \begin{pmatrix} \tilde{x}_\varphi \\ \tau \end{pmatrix} = \frac{d}{dt} \begin{pmatrix} e_\varphi \\ \dot{e}_\varphi \\ \tau \end{pmatrix} = \begin{pmatrix} M^{-1}(\varphi) [(\tau - \tau_u) - h(\varphi, \dot{\varphi})] - \ddot{\varphi}_d \\ \frac{1}{T_\tau} \mathbf{I}_2 (\tau_c - \tau) \end{pmatrix}, \quad (6.42)$$

where τ_u still represents all input disturbances. As an approach, it is expected that the disturbance torque behaves in accordance with

$$\hat{\tau}_u = K \tilde{x}_\varphi + \psi \quad (6.43)$$

$$\dot{\psi} = \Phi(\tilde{x}_\varphi, \hat{\tau}_u, \tau_c), \quad (6.44)$$

where $K = k \begin{pmatrix} \mathbf{I}_2 & M & \mathbf{0}_2 \end{pmatrix} \in \mathbb{R}^{2 \times 6}$, $k \in \mathbb{R}$. By assuming the disturbance torque is constant, the error dynamics is

$$\dot{e}_\tau = -\dot{\hat{\tau}}_u = 0, \quad (6.45)$$

which becomes zero for a steady state. The function

$$\Phi(\tilde{x}_\varphi, \hat{\tau}_u, \tau_c) = -k \dot{M} \dot{e}_\varphi - k \dot{e}_\varphi - k M \left(M^{-1} [(\tau - \hat{\tau}_u) - h] - \ddot{\varphi}_d \right) \quad (6.46)$$

can be directly determined from this equation. By substituting $\Phi(\tilde{x}_\varphi, \hat{\tau}_u, \tau_c)$ back to the error dynamics, consequently, the error dynamics is

$$\dot{e}_\tau = -\dot{K}x_\varphi - K\dot{x}_\varphi - \Phi(x_\varphi, \hat{\tau}_u, \tau_c) \quad (6.47)$$

$$\begin{aligned} &= -k\dot{M}\dot{e}_\varphi - k\dot{e}_\varphi - kM \left(M^{-1} [(\tau - \tau_u) - h] - \ddot{\varphi}_d \right) \\ &\quad + k\dot{M}\dot{e}_\varphi + k\dot{e}_\varphi + kM \left(M^{-1} [(\tau - \hat{\tau}_u) - h] + \ddot{\varphi}_d \right) \end{aligned} \quad (6.48)$$

$$= -k(\tau - \tau_u) + k(\tau - \hat{\tau}_u) \quad (6.49)$$

$$= k(\tau_u - \hat{\tau}_u) \quad (6.50)$$

$$= ke_\tau. \quad (6.51)$$

As can be seen, the error dynamics is asymptotically stable for $k < 0$.

As a recommendation for the implementation of this disturbance torque observer, it must be said that the torque τ can be measured indirectly by measuring the PMA pressures and lengths, passing this measured data into Eq. (4.1). Due to this, no additional torque sensor is needed and the amount of required sensors remains the same as for the backstepping controller without time-delayed torque signals.

6.9. Experimental Investigation of the Pose Controller with Time-delayed Torque Signals

In this section, the performance of the presented backstepping controller for a 2 DOF robot with PMA-driven joints and time-delayed torque inputs is tested. By taking the desired control task defined in Section 6.3 as a measure, the tracking performance of the controller can be evaluated with the graphs provided in Fig. 6.5.

For all measurements, the controller gains of the backstepping controller are set to $k_1 = k_3 = 11.71$, $k_2 = k_4 = 13.31$, $k_{v1} = 114.27$, and $k_{v2} = 138.39$, and the observer gain is set to $k = -0.63$ by experimental testing, which is the same value as in Section 6.6 determined by experimental testing. As already mentioned, the pressure controller bandwidth was determined as 4 Hz by measurement, i.e. the time constant is $T_\tau = 0.0398$ s.

In the beginning, it can be seen in Fig. 6.5 that the novel backstepping controller is able to make the robot follow the desired trajectory with only small deviations. The maximum tracking error for the base joint is about 3° (black line in Fig. 6.5a) and about 8° for the elbow joint (black line in Fig. 6.5b). In case the controller is extended with an additional, observer based, disturbance torque compensation, the tracking error can be further reduced. This is demonstrated by the blue lines in Fig. 6.5a, respectively Fig. 6.5b. The lines are generally closer to the desired trajectory as long as the base pulley is standing still. As a result of the loose pulley at the base joint, the system still gets very close to the edge of stability sometimes, i.e. the robot starts to

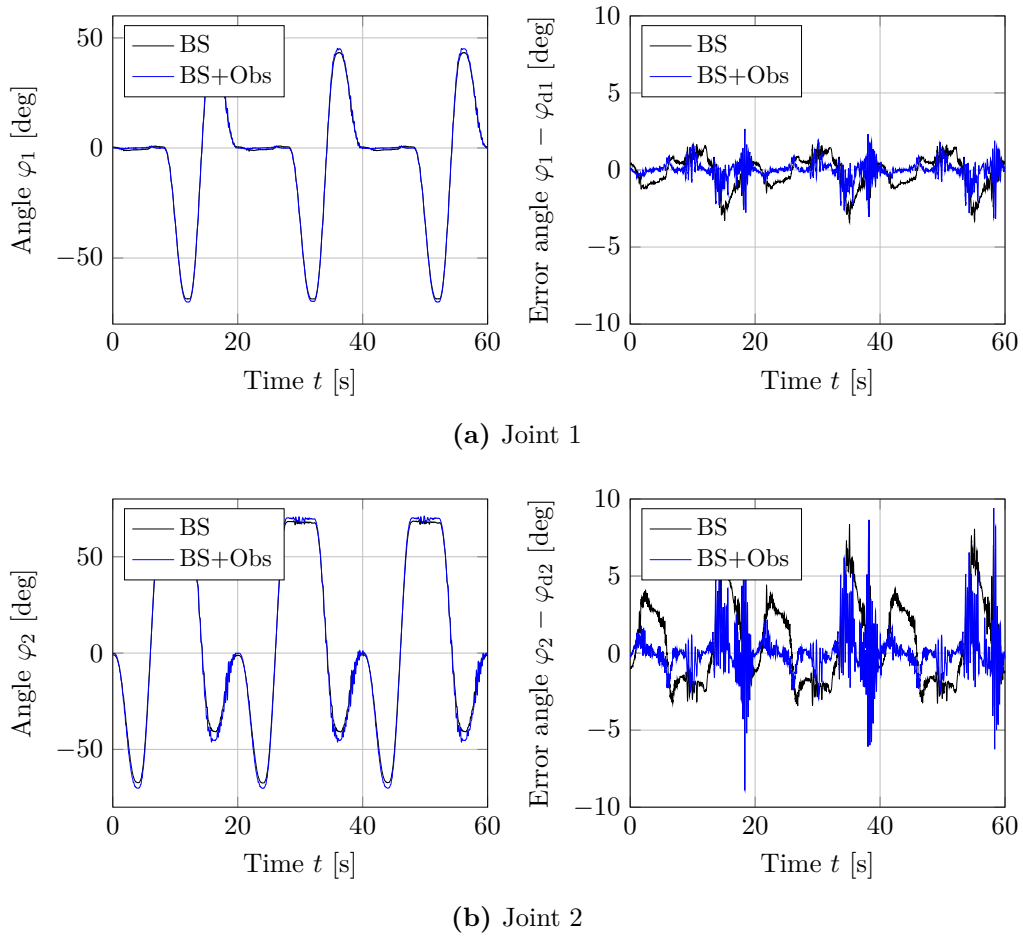


Figure 6.5.: Tracking performance of a backstepping controller for time-delayed torque signals with and without additional disturbance torque observer

shake and accordingly, the tracking error increases significantly within short time spans. Nevertheless, the system does not run into instability due to an insufficient bandwidth of the torque controller anymore. Moreover, the visible robustness of the controller, taking the time delay of the torque signals into account, is superior in comparison to the controller designed for a direct feed-through of the torque input signals.

6.10. Conclusion

In this section a planar 2 DOF robot with PMA-driven joints was controlled successfully. Thereby, the non-linearity of both PMA-driven joints was compensated by an individual joint torque control interface, as discussed in Chapter 4. Especially for the PMA-driven joints under torque control, the methodology in Section 6.4 demonstrates

how PMA-driven joints can be analyzed with respect to their suitability for a given task.

The overlying motion or pose controller design was carried out in accordance with a backstepping controller design. Since this controller does not provide any integral action, it is not able to compensate load disturbances like model uncertainties or friction. To overcome this problem, the backstepping controller was extended with a disturbance torque observer, i.e. the estimated torque could be compensated by adding the estimated torque with opposite sign.

As it was demonstrated in experiments, the bandwidth of the torque controller was lower than theoretically expected. For this particular system, the torque controller cut-off frequency was 4 Hz instead of the theoretically expected 16 Hz. This was critical because, for a first pose controller, the torque was treated as non-delayed input signal. Although this approach was valid in case the bandwidth was high enough, it did not represent the system properly for torque controllers with a low bandwidth. Due to this, a pose controller for systems with time-delayed torque input signals was presented additionally.

As the major result of this chapter, it can be said that, independent of whether or not the robot with PMA-driven joints has one or multiple degrees of freedom, it can be controlled by controlling the torque of every joint individually. Thereby, the design of the overlying motion controller design gets simplified significantly. Since the torque controllers are handling all non-linearity, the PMA-driven joints are losing their deterrent characteristic. Due to this, an integration of PMA-driven joints into robotic systems is facilitated, even without the necessity to study PMAs, PMA-driven joints and pneumatic pressure dynamics.

7. Controlled Active Motion (CAM) Control of the Rehabilitation Robot PMA-CAMOPED

7.1. Introduction

The motivation for driving robots with PMAs is constituted by their light weight, high power-to-weight ratio and their passive compliance. From this perspective it is not surprising that PMAs were also integrated into robotic systems that are made for rehabilitation or assistance of injured, weak or diseased people. The exoskeletons presented in [22, 11, 73, 59, 57] and the devices made for ankle and knee joint rehabilitation presented in [43, 69, 29] demonstrate how PMAs can be integrated in rehabilitation systems. While the design and the construction of all these systems differ significantly – in dependency of the body part they are designed for – the control problem is mostly formulated as follows: The affected limbs or body parts of the patient should be moved periodically along a path as it is done by physical therapists in conventional therapy. During that motion the patients are moved passively, .i.e. they do not have to work with their own muscles. This is called continuous passive motion (CPM) therapy.

A PMA-driven system that is able to realize a CPM for both arms is the exoskeleton of Balasubramanian et al. [11], where an iterative learning controller improves the tracking behavior of the controller from motion cycle to motion cycle. The PMA-driven knee and ankle rehabilitation robot presented by Knestel et al. [43] is controlled by a backstepping position controller and also enables a CPM. Although the design and the control strategy is different for the rehabilitation devices of Thanh and Phuc [69] and Deaconescu and Deaconescu [29], both also provide a CPM of the knee joint, respectively, and are driven by PMAs.

Although robot-assisted CPM therapy seems reasonable for many injuries, the controlled active motion (CAM) therapy is preferred, for example, in case of a knee cruciate ligament rupture [77]. In contrast to the CPM, the patient has to move his leg actively but shares the effort with the robot to which the patient is coupled. The level of assistance or resistance can be chosen by the therapist according to the patient's individual constitution. It has been shown by Von Lübken et al. [77] that patients, after a therapy with CAM, achieved better results within a reproduction test of the knee joint angle proprioception [39] which represents an indicator of the healing progress.

Many CAM devices for knee rehabilitation – purely passive or even active systems – are already available as products. PMAs would be particularly well-suited for such systems due to their inherently compliant dynamics and their capability to provide both variable resistance and, by co-contraction of pneumatic muscle pairs, variable stiffness. Despite these advantages, an active system for CAM therapy that is driven by PMAs has not been developed yet. The current chapter of this dissertation aims to fill this gap and to give an experimental proof of concept. The passive CAM device CAMOped (OPED GmbH, Oberlindern) was redesigned, where the mechanical brake of the original system was replaced by a PMA-driven joint (see Fig. 7.1) [68]. This holds the advantage that the resistance – or the support – can be varied in real time during the motion.

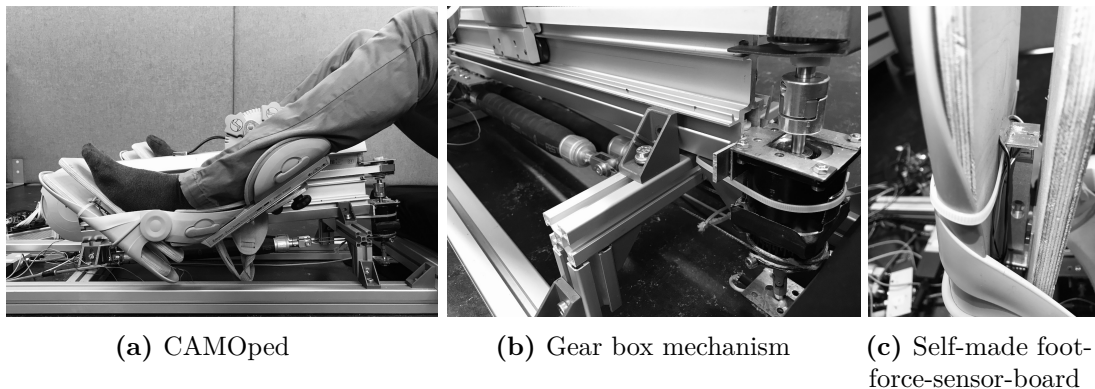


Figure 7.1.: Reconstructed CAMOped with PMA-driven joint

For the following chapter, it must be mentioned that the findings were to some extent already published by the author in

M. Martens, J. Zawatzki, T. Seel, and I. Boblan. A pneumatic-muscle-actuator-driven knee rehabilitation device for CAM therapy. In *41st International Engineering in Medicine and Biology Conference*. IEEE, 2019 .

7.2. A System Description

The original CAMOped is a device made for CAM therapy and is recommended for training after the ruptured cruciate ligament has been fixed by surgery. The CAMOped is purely passive and the resistance can be varied via a mechanical brake, i.e. the patient has to push against the friction of the brake with their left respectively right leg. In [68], the passive CAMOped was reconstructed as an active system, as shown in Fig.7.1. The mechanical brake was replaced by a combination of a PMA-driven joint and a gear box (see Fig. 7.1b; gear ratio 10:1; $\eta = 10$). Due to this, the resistance becomes adjustable via the torque of the PMA-driven joint that counteracts the movement of the patient. In contrast to the original CAMOped, the resistance can now be varied

– e.g. in dependency of the knee angle – while the device is in service. Furthermore, the patient can even get assistance during the training by the reconstructed CAMOPed because the PMA-driven joint is able to exert a torque in both directions, clockwise and counter-clockwise.

The CAMOPed has two boards onto which the feet can placed. Pushing alternately with the left respectively the right foot, the resulting leg movement resembles cycling. According to Fig. 7.2, the foot forces denoted by F_{fl} for the left and F_{fr} for the right foot, respectively, are defining a torque τ_h that the patient exerts on the CAMOPed. The

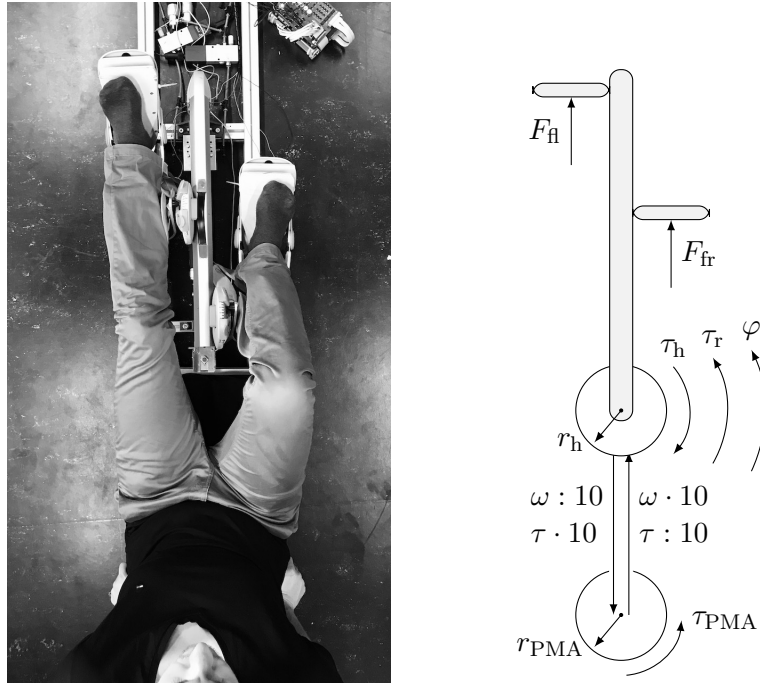


Figure 7.2.: Free-cut of the re-constructed CAMOPed

pulley, connected to the foot boards via a toothed belt, has a radius of $r_h = 20$ mm. Via a gear box (gear ratio 1:10; $\eta = 10$), the upper pulley is connected to a second pulley that is a part of a PMA-driven joint. This second pulley has a radius of $r_{PMA} = 25$ mm. To adjust the CAMOPed to the patient's leg length, the foot board's relative position on the toothed belt can be changed. As a result of the leg length of two different test patients at the Beuth Hochschule für Technik Berlin, the most comfortable foot plate position on the toothed belt is achieved with an angle range of $\varphi \in [-41^\circ, 41^\circ]$, measured at the pulley of the PMA-driven joint. This correlates with a foot displacement range of $[-143.12, 143.12]$ mm. Both PMAs of the PMA-driven joint are Festo DMSP-20-353. Furthermore, the PMAs are connected to their pulley at half-contraction, so that the angle range is at its maximum. At $\varphi = 0$, both legs are in the same mid-position and both PMAs are at half-contraction. By pushing with the right foot, the upper pulley is rotated in the positive; by pushing with the left foot, the pulley is rotated in the

negative direction. As mentioned in Chap. 3, the PMA maximum contraction is about 25 % of its initial length. Due to this, the maximum contraction of a DMSP-20-353 is about 88.25 mm. The maximum force is about 1.5 kN \approx 150 kg load mass. To adapt the benchmarks of the PMA-driven joint to ranges more useful for knee joint rehabilitation, a gear box has been integrated between the PMA-driven joint and the patient. While the geared contraction is increased to 88.25 cm, the resulting maximum force is reduced to \approx 150 N \approx 15 kg.

The friction torque τ_r sums up all the friction of the mechanical transmission line – ropes, pulleys, and a gear box – and is supposed to behave like a Coulomb friction. Due to this, the friction can be described by $\tau_r = |\tau_r| \text{sign}(\dot{\varphi})$. The absolute value of the friction torque is determined as $|\tau_r| = 2.6 \text{ Nm}$ by pushing one foot plate and measuring the foot contact force multiplied with the pulley radius r_h . Since the friction counteracts with the torque of the patient, positive friction is defined to be positive in the opposite direction of the patients torque τ_h .

In accordance with the previous chapter, the pressure within both PMAs is controlled with a Festo MPYE-5-1/8-LF-010-B proportional servo valve. While the inner PMA pressure is measured with two Festo SPTE-P10R-S4-V-2.5K pressure sensors, the pulley angle is measured by an off-the-shelf potentiometer. In addition, foot contact forces up to $20 \text{ kg} \cdot 9.81 \text{ m/s}^2 \hat{=} 196.2 \text{ N}$ can be measured with two self-made foot-force-sensor boards (see Fig.7.1c). All sensors and both valves are connected to the target control platform, a MicroDAQ E2000 (Embedded Solutions, ul. Rzeszowska 74b, 39-100 Ropczyce, Poland) which can be programmed with a MATLAB (R2015b, The MathWorks, Inc., Natick, MA, USA) Simulink toolbox.

7.3. Design of a CAM Controller

The original passive CAMoped is reconstructed as an active system, actuated by a PMA-driven joint. Although a CPM could be implemented with this system, a controller for a CAM will be designed in this thesis, i.e. the foot load can be varied while the CAMoped is in service. Furthermore, the CAMoped could also support the patient during the training because a PMA-driven joint is able to exert a torque in both directions.

For this particular device, it is important to use the full work potential of the PMAs. In addition, the maximum frequency of cyclic stepping is expected to be rather low – smaller than 2 Hz – during rehabilitation training. Due to this, the application's demand of a high torque is the most critical, i.e. the torque controller will be designed as a "FIT torque controller" as described in Sec. 4.3.1. This approach enables the full exploitation of the PMAs work potential. Nevertheless, using the PMA only for exerting a force comes along with no initial tension, which is a very theoretical case. Due to uncertainties of the construction and the PMA force model, the initial tension for the CAMoped

controller is set to $F_{IT} = 0.05 \cdot \max(F_{PMA}) = 0.05 \cdot F_{PMA}(\max(p), \min(L)) = 76.58 \text{ N}$ for the PMA DMSP-20-353. The resulting torque range is depicted in Fig. 7.3.

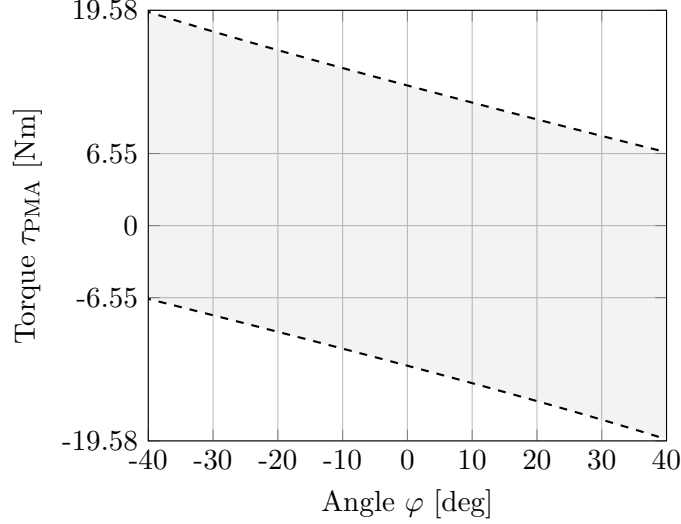


Figure 7.3.: Torque range CAMOPed controller for two DMSP-20-353 connected at half contraction

Both PMAs are connected to the pulley at half-contraction and the resulting torque range is depicted in Fig. 7.3. While a torque of 6.55 Nm can be exerted by the PMA-driven joint in both directions, the maximum torque of 19.58 Nm can only be exerted at the edges. Due to the gear ratio $\eta = 10$ and the CAMOPed's pulley radius $r_h = 20 \text{ mm}$, the related angle-independent foot force range is $[-32.75, 32.75] \text{ N}$, while the maximum angle-dependent foot force range is limited to $[-97.9, 97.9] \text{ N}$. In other words, the maximum angle-dependent foot load is about 10 kg, while a foot load of about 3.3 kg can be guaranteed for every position.

In contrast to the pressure controller used for position control, the torque controller for the CAMOPed will not represent the inner pre-controller but will be used in its pure form. Due to this, the pressure controller will not be used as an inner controller, so that the requirement of a precise pressure control gets emphasized. In accordance to Sec. 4.5.4, the adaptive pressure controller (4.34) provides integral action due to its integrating pole at $z = 1$ and an anti-windup mechanism.

While the control bandwidth of the pressure controller is set to $f_{bw} = 10 \text{ Hz}$ (see Eq. (4.32)), the observer poles are placed at 20 Hz, 26 Hz, 32 Hz, 38 Hz, and 44 Hz. Due to frequency folding, the controller is designed so that frequencies of 142 Hz, 285 Hz, and 428 Hz are ignored by the controller. The poles of the anti-windup polynomial are all set to 80 Hz. The sampling frequency of the controller is chosen as 1 kHz. In accordance with Sec. 4.5.3, the resulting closed-loop pressure dynamics can be described by the

first-order lag filter

$$H_{\text{clp}} = \frac{1 - 0.9391}{z - 0.9391}. \quad (7.1)$$

Furthermore, the closed loop sensitivity is smaller than $|\mathcal{S}| \leq 1.8 < 2$, i.e. the closed pressure loop has a reasonable robustness. In Fig. 7.4, both the magnitude and the sensitivity of the closed pressure loop are depicted. Since the pressure controller schedules

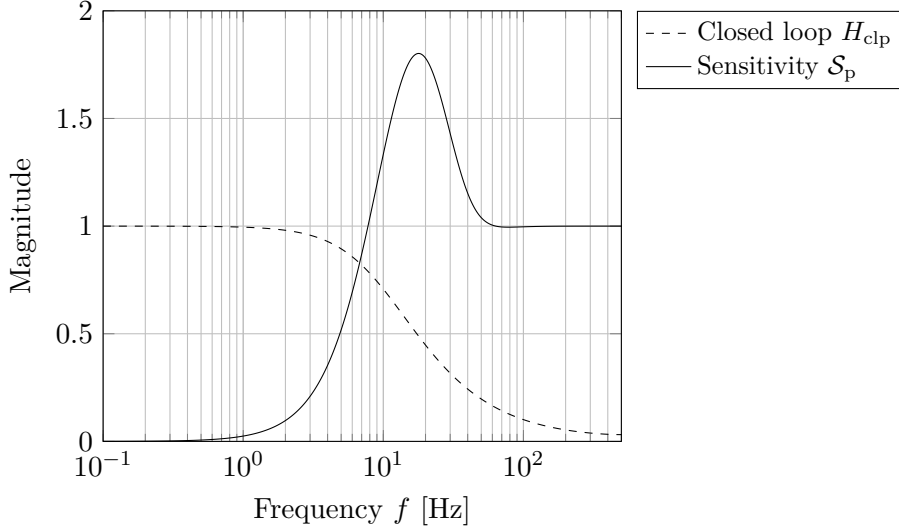


Figure 7.4.: Magnitude of the closed pressure loop H_{clp} and its sensitivity \mathcal{S}_p

its gains in dependency of the PMA volume, and therefore multiple linear pressure controllers for different volumes exist, it should be noted that the plot depicted in Fig. 7.4 looks exactly the same for every pair of the controller and the PMA volume for which it is designed. Due to this, the robustness of the pressure controller can be investigated independently of the volume.

As demonstrated in Chapter 3, the PMA force can be measured and modeled very precisely. Due to this, the torque could be controlled without torque feedback. Nevertheless, an additional torque feedback signal, calculated from the foot-force sensor signals, stabilizes the output torque and counteracts disturbances or other uncertainties. The chosen controller is a proportional controller, as depicted in Fig. 7.5. The controller gain – determined by experiment – is chosen as $k_p = 3.4$. Furthermore, the measured friction torque τ_r is compensated by a feed-forward control.

As a result of the additional proportional feedback, the pole p_c is shifted to $\hat{p}_c = p_c(k_p + 1) - k_p = 0.732$, i.e. the closed loop remains stable.

As will be shown, the torque controller depicted in Fig. 7.5 is able to control the torque of a PMA-driven joint very precisely. Nevertheless, it must be clarified how the reference torque τ_{ref} should be defined. In a CAM therapy, it is quite common that the patient is advised to move their affected joint periodically from a lower to a higher joint angle limit

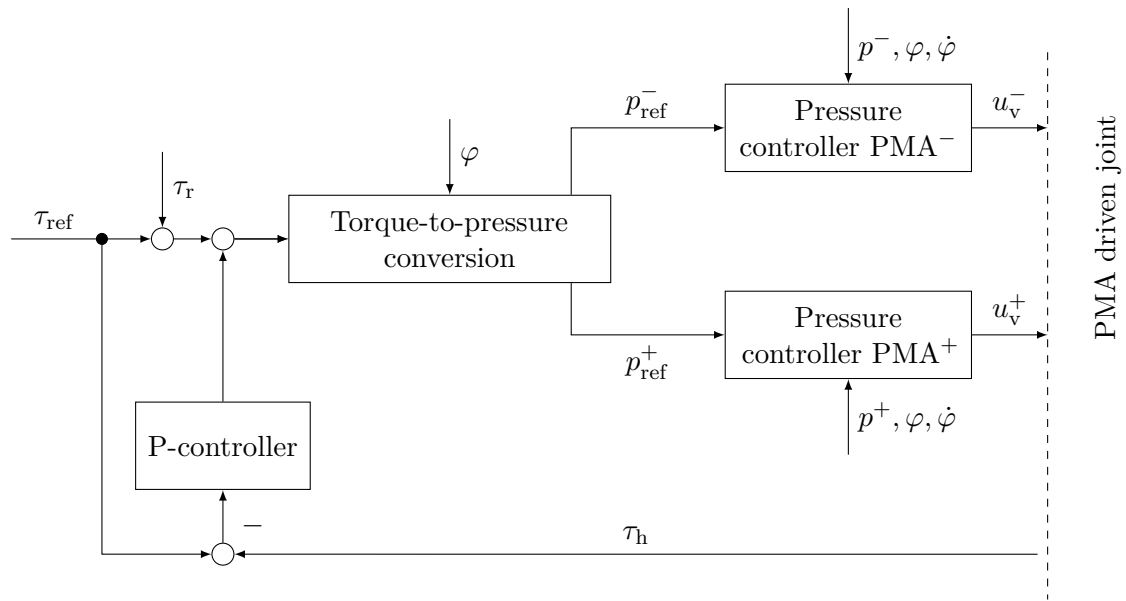


Figure 7.5.: CAM controller CAMOPed

and vice versa. Since the CAMOPed is made for knee rehabilitation, this means that the patient stretches their left respectively right leg. In accordance with this requirement, the torque reference trajectory is defined as follows: While pushing with one foot on the footplate – i.e. the leg is stretching –, the foot load on this foot follows a predefined load trajectory while the load on the other foot is ignored. The load trajectory can be varied or held constant depending on the knee angle. Since the foot plates are paired with the PMA-driven joint, the load trajectory defines a torque trajectory for the PMA-driven joint. By pushing with the right foot, the pulley of the PMA-driven joint is rotated in counter-clockwise direction until the angle reaches the upper limit of 41° . By definition (see Fig 7.2), it should be noted that keeping the load on the right foot positive is equivalent to keeping the torque of the PMA-driven joint negative and vice versa. At 39° , the controller switches the reference signal from the right to the left foot, i.e. the left foot load is now following a predefined load trajectory while the load on the right foot is ignored. At the same time, the reference torque of the PMA-driven joint switches its sign from negative to positive. In this position, the left leg is almost fully compressed. While stretching the left leg, the foot load for the left foot is kept on the load trajectory until an angle of -39° is exceeded. At this point, the controller switches back to the right foot, i.e. the next round can be started. In the end, it should be noted that not only resistance but also assistance can be provided by the reconstructed CAMOPed with PMA-driven joint. This can be done very easily by changing the sign of the given reference torque.

7.4. Experimental Results

The controller, implemented as described in the previous section, is tested in the following scenario: While the subject is training with the CAMOPed, the torque of the PMA-driven joint is set – from low to high – to 0.1 Nm, 2 Nm, 4 Nm, 6 Nm, 8 Nm, 10 Nm, 12 Nm, 16 Nm and 20 Nm. Each torque value is kept constant for two cycles. During the test, the torque is measured via the foot forces multiplied with the pulley radius of the upper pulley. The result can be seen in Fig. 7.6a. It should be noted that the torques are corresponding to a foot load of 0.5 N, 10 N, 20 N, 30 N, 40 N, 50 N, 60 N, 80 N and 100 N, respectively.

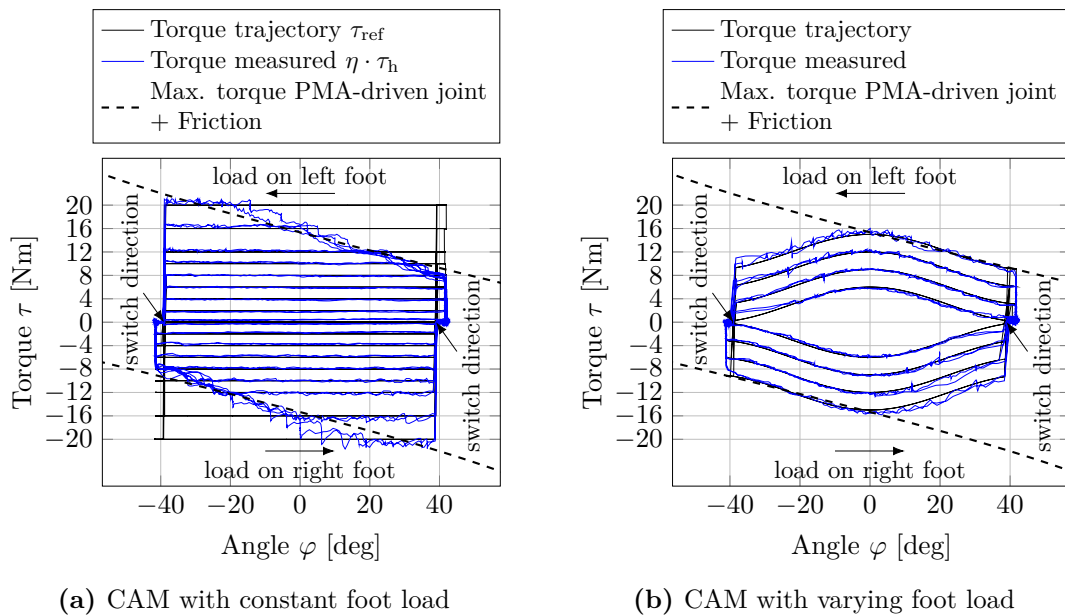


Figure 7.6.: Torque over pulley angle during two different exemplary rehabilitation exercises using the CAMOPed with PMA-driven joint

While the black lines in Fig. 7.6 are defining the reference torque, the blue lines are representing the measured torque, the test subject exerts on the CAMOPed. Furthermore, a positive torque belongs to a load on the left foot and a negative torque causes a load force on the right foot. This becomes clearer, by going back to the CAMOPed free-cut (see Fig. 7.2), where it can be seen that e.g. a positive torque of the PMA-driven joint counteracts the pushing of the left foot.

As can be seen, the measured torque almost equals the reference torque. For a complete matching, a controller with integral action would be necessary, but integral action should be avoided in robots that are in direct contact with human users. Furthermore, the measured torque is noisier for higher values. This is due to the increasing effort with which the subject has to push against the footplate and due to muscular fatigue.

The black dashed lines are defining the upper respectively the lower torque limit. It must be noted that these limits are not only defined by the PMA-driven joint like it can be found in Fig. 7.3, but are the result of the torque the PMA-driven joint can exert and the friction torque of the CAMOped that also counteracts the patients torque.

While Fig. 7.6a shows that the new redesigned CAMOped is able to provide the same functionality as the original system, Fig. 7.6b shows their difference. In contrast to the original CAMOped, the redesigned PMA-driven system has the ability to vary the resistance while the device is in service. The resistance curve can thus be designed freely i.e. it can be adapted to the patient's needs.

7.5. Conclusion

In this chapter a cascaded controller for a PMA-driven CAMOped has been presented and tested. The PMA-driven joint was controlled by a torque controller, i.e. the PMA-driven joint was able to support or counteract the patients movement in accordance to a given torque trajectory. It was demonstrated experimentally that the presented control approach keeps the torque perfectly constant up to 20 Nm – this corresponds to a foot load of 100 N – with only slight deviations from the original, constant torque trajectory. Furthermore, it was demonstrated that the proposed torque controller is able to follow a variable torque trajectory, which can be designed according to the patient's needs.

In contrast to previous PMA-driven rehabilitation devices, the controller enables CAM rather than CPM therapy. The novel device represents a promising rehabilitation tool for injuries like a rupture of the knee cruciate ligament, for which the CAM therapy is considered superior. Future research will aim at finding suitable torque trajectories for rehabilitation and evaluating the system in patient studies.

8. General Conclusion and Outlook

This thesis was concerned with the analysis of PMAs, PMA-driven joints and their application in robotic systems. Before this thesis much attention was set on single, particular robotic systems with PMA-driven joints, but a general discussion of PMA-driven joints was widely missing. Moreover, it was mostly unclear how the task of the robot is related to the characteristics of PMA-driven joints. Within the previous chapters a detailed discussion of PMAs, PMA-driven joints and their application in three different robotic systems was given. The main findings will be provided during the following sections, where each of the three different main topics is discussed individually.

8.1. General Conclusion on Modeling PMAs

As controlling the torque of a PMA-driven joint without the knowledge of the exerted force of a single PMA is impossible, Chapter 3 investigated the PMA force of a single PMA. The PMA force can be subdivided into a static and a dynamic force, but the former dominates the PMA force by far. Although the PMA force was already investigated by other researchers before this thesis, there was neither a consensus about how to measure the PMA force correctly nor which model approximates the static force in the best possible way. A discussion about a superior modeling approach describing the dynamic PMA force was already provided by Aschemann and Schindele [9].

As a contribution of this dissertation to the overall discussion, a measure of quality suitable for all existing static PMA force models was defined in Chapter 3, i.e. a comparison of different models was facilitated. To guarantee the comparability of all models, their free non-measurable parameters were determined by the same minimization of the least square error between a measured and a model-based PMA force map. In addition, it was shown that, in contrast to the findings of Minh et al. [54], the measured PMA force is mostly independent of the chosen measurement setup. Hence, the measured PMA force was approximately the same for the isobaric and isometric measurement setup, i.e. the influence of the measurement setup to the PMA force map can be mostly neglected.

After comparing most existing PMA static force models, a novel approach with higher accuracy was introduced in Chapter 3. The quality of this new approach was further improved by an extension, and the error of this new, extended model for a Festo DMSP-20-300 was only 1.92 %.

Finally, and based on the new extended model, the PMA was investigated with respect to its mechanical spring stiffness. It was shown that the stiffness of the PMA can be varied by its inner pressure and additionally depends on the PMA length. Furthermore, the stiffness range of a PMA was quantified; hence, the PMA stiffness can be included in the future not only qualitatively but quantitatively. Due to this, the attribute of passive compliance of PMAs becomes clearer, and especially the ability to store potential energy should be included in future PMA-driven robots.

8.2. General Conclusion on the Torque Control Interface for PMA-driven Joints

One of the main goals of this thesis was to provide a new torque control interface for PMA-driven joints. The proposed interface represents a general concept of analyzing and integrating PMA-driven joints into robotic systems. A simplification of the integration of PMA-driven joints into robotic systems is desirable, because only with a simple interface, the usability can be further improved. As a result the novel, user-friendly interface promotes the decision to actuate new robotic systems with PMA-driven joints and hopefully enables an increased application of PMA-driven joints in future robotic systems. As a consequence, PMA-driven joints are becoming more accessible, i.e. without the need for extensive study of PMAs and pneumatic dynamics. This is because the most challenging characteristics of the PMA-driven joint are handled internally by the torque controller. As a result of the advantageous attributes of PMAs, like their high power-to-weight ratio and their ability to store potential energy, new or even existing robotic systems can be made safer and more energy-efficient by actuating them with PMA-driven joints.

Before this thesis, PMA-driven joints were exclusively integrated into a few first robot prototypes. Although most publications about robots with PMA-driven joints showed that special robots with PMA-driven joints can fulfill their desired control tasks, the focus was primarily set to the overlying motion controller design. In the meantime, the pre-conditions – the attributes of the PMA-driven joints – making a successful controller design feasible were discussed mostly at the edge or completely ignored. Due to this, it is often hard to understand how to achieve the same results with another robotic system or PMA-driven joints with different PMAs and radius.

In combination with the torque control interface for PMA-driven joints developed in Chapter 4, the PMA-driven joint is fully characterized only by its static torque characteristic and its bandwidth. This is all the information that an engineer needs to know for deciding whether or not a PMA-driven joint is suitable to drive a particular robot. Once the PMA-driven joint is torque controlled, it becomes a plug-and-play-like actuator, i.e. the focus of the robotics engineer can be set to the overlying controller design. The simplified handling of torque-controlled PMA-driven joints was demonstrated in Chapter 5, 6, and 7, where torque-controlled PMA-driven joints were integrated into a

1 DOF and a 2 DOF planar robot by following the same steps. Accordingly, it can be said that the concept of a torque-controlled PMA-driven joint is not only valid for one particular robot but represents a general concept of how to control a robot successfully.

As discussed in Chapter 4, PMA-driven joints are not only able to exert a joint torque but are able to vary the joint stiffness by co-contracting simultaneously. This additional degree of freedom is used in this thesis to ensure tight ropes for every angle. Nevertheless, the mean pressure – i.e. the co-contraction – is set to a fixed value for every angle but could be varied to adjust the joint stiffness depending on a changing task or environment. The implementation of such a variation of joint stiffness via co-contraction should be included in future research. Motivated by the efficiency and adaptability of human beings and animals, a co-contraction controller could improve future robotic systems.

8.3. General Conclusion on Robotic Systems with PMA-driven joints

In contrast to their promising attributes, to date, PMA-driven joints are only rarely in use for driving robotic systems. A likely reason for this is, that a broad discussion of their dynamics and characteristics as well as a handy instruction of how to integrate PMA-driven joints into robotic systems with respect to their requirements was missing before this thesis. As a result of the torque control interface, as proposed in Chapter 4, the PMA-driven joint can now be integrated into robotic systems in a plug-and-play-like fashion.

The simplicity and generality of this concept of combining a PMA-driven joint with a torque control interface was demonstrated by the three different exemplary robots controlled in this thesis. On the one hand, the 1 DOF and 2 DOF robot of Chapters 5 and 6 were demonstrating that making a robot with PMA-driven joints follow a given trajectory was possible with only a few degrees of deviation. Accordingly it can be said that PMA-driven joints are suitable for a broad range of positioning and pose-trajectory control tasks like they are highly relevant for production and in industrial environments. As a by-product of driving the robot with PMA-driven joints, the safety for humans can be increased as well as the potential of solving task with higher energy efficiency gets enabled.

On the other hand, the rehabilitation robot PMA-CAMOPED of Chapter 7 has shown how to provide a pre-defined resistance torque with a PMA-driven joint, enabling a CAM therapy. This exemplary robotic system demonstrates that, also for rehabilitation robots PMA-driven joints can be a proper choice of actuators.

By taking a closer look to the controller design of Chapter 5, 6 and 7 it stands out, that for all three robots the controller design was simplified enormously, by the use of torque-controlled PMA-driven joints. More precisely, the control problem was reduced to the pure tracking control respectively resistance torque controller design. The PMA

and pressure dynamics were handled by the torque controller of each joint. This leads to the conclusion that the torque controller decouples the problem of controlling the dynamics of the PMA-driven joint and controlling the robot dynamics. Due to this, the approach of controlling the torques decentralized by an underlying torque controller seems to provide a promising adaptivity and scalability in the sense that this control architecture can be applied to many other robotic systems in future.

8.4. Future Research

There are several aspects that should be included in future research. Firstly, it would be desirable to determine a PMA force model that has no need for adaption through some free parameters and, hence, no need for their identification. It is remarkable that, although all existing models describing the PMA force are physically motivated, none of these models, including the introduced models in Chapter 3, seem to describe the true physical behavior of the PMA directly based on a-priori known physical quantities. With such a model, the necessity of measuring the PMA force map would vanish and the effort to use PMAs would be significantly reduced. Secondly, it would be of interest if the parameters of the same model with a different PMA type would be correlated, i.e. the force map of a new PMA could be determined from interpolating other parameters that were already determined by minimization. This would simplify the applicability of PMAs enormously because measuring a PMA force map goes along with high effort and a mostly complex measurement setup. In case the parameters are correlated, some parameters of particular PMAs could be provided by the data sheet. Additionally, in case a new PMA with another length or diameter would be integrated to a new robotic system, the procedure of measuring the PMA force could be skipped.

Like it has been discussed in the previous chapters, PMA-driven joints are a very promising technology for making future robots safer and more energy-efficient. Their ability to store and set free potential energy and to simultaneously exert a joint torque is really close to the muscle-tendon apparatus of human beings and animals. Since the ability of human beings and animals to adapt to varying tasks and surroundings is still unmatched by robotic systems, PMA-driven joints are representing a promising actuator in comparison with standard actuators like electrical motors. In this dissertation, the PMA-driven joint was investigated on its own, and it was shown that, once it is under torque control, it is characterized by only its static torque range and its bandwidth. Since only PMA-driven joints with two PMAs that were connected at half-contraction were investigated in this thesis, the extension of similar investigations to PMA-driven joints with any combination of two PMAs would be of interest in future. Although such an investigation for the static torque range of a PMA-driven joint is partly provided by Dirven and McDaid [30], a similar investigation for the resulting torque controller bandwidth and the resulting PMA-driven joint stiffness is not presented yet. In addition, the torque controller, as proposed in Chapter 4, should be extended by simultaneous

stiffness control because by controlling the torque and the joint stiffness simultaneously the full potential of a PMA-driven joint can be fully exploited.

The three exemplary robots of this thesis were controlled with a cascaded controller design with an underlying torque controller, one for every PMA-driven joint. By pre-controlling the joint torques provided by the PMA-driven joints, the design of the overlying position or CAM controller gets simplified as it is in Chapter 5, 6 and 7, respectively. In future, it would be of interest how this control architecture performs in new or even other existing robots with PMA-driven joints. Moreover, the promising ability of PMA-driven joints to vary their co-contraction should be included in future robotic systems. It is very likely that most robotic tasks can be solved with improved energy efficiency and that challenging problems like robotic walking could be solved by the selective application of this feature.

List of Figures

2.1.	Sonic conductance $C(x_v)$ in dependency of the normalized valve slide stroke x_v of a Festo MPYE-5-1/8-LF-010-B proportional servo valve taken from Cabos [21]	12
2.2.	Schematic of the planar robot with 1 DOF	15
2.3.	Schematic of the planar robot with 2 DOF	17
3.1.	McKibben-like PMA in the foreground and a Festo PMA in the background	21
3.2.	Photo of the test rig that is used to measure the characteristic force maps.	23
3.3.	Force of a Festo DMSP-20-300 measured isometrically for different pressures	24
3.4.	Photo of the test rig for an isobaric measurement of the PMA force map.	25
3.5.	Force map of a Festo DMSP-20-300 measured isobarically	26
3.6.	Force of a Festo DMSP-20-300 measured isometrically (blue) and isobarically (black), respectively, for different pressures	26
3.7.	Measured force map of a Festo DMSP-20-300	27
3.8.	Unreeled membrane of a Festo PMA	28
3.9.	Schematic of the PMA membrane and the fiber angle.	31
3.10.	Isobaric measured force map of a Festo DMSP-20-300 and its approximation	35
3.11.	Exemplary hysteresis curve of a Festo DMSP-20-300 measured @ 4 bar .	38
3.12.	Force prediction error of a model describing the DMSP-20-300 static force with (black) and without hysteresis (blue), respectively.	40
3.13.	Mechanical interpretation of a PMA as a combination of force source, spring and damper	41
3.14.	Stiffness of a Festo DMSP-20-300 for different pressures	42
4.1.	Schematic of a PMA-driven joint	45
4.2.	Structure of the sensor-less torque controller for a PMA-driven joint . .	46
4.3.	Overlap of two PMA force maps; PMA ⁺ colored in black, PMA ⁻ colored in blue	50
4.4.	Torque characteristics of a PMA-driven joint controlled by two different torque control approaches with integrated FIT and PM converters, respectively.	53
4.5.	Stiffness of the PMA-driven joint with FIT converter for an exemplary Festo DMSP-20-300 and a pulley radius of 23.24 mm	55
4.6.	Stiffness of the PMA-driven joint with PM-converter for an exemplary Festo DMSP-20-300 and a pulley radius of 23.24 mm	56

4.7.	Gain scheduling pressure controller with two degrees of freedom and disturbance cancellation	59
4.8.	Pressure controller with with integrator and anti-windup mechanism	63
5.1.	Robot arm with PMA-driven joint and 1-DOF	66
5.2.	Desired angle trajectory the 1 DOF robot should follow	68
5.3.	Torque characteristic of the 1-DOF robot	69
5.4.	Robot with 1 DOF - Magnitude of the closed pressure loop H_{clp} and its sensitivity \mathcal{S}_p	71
5.5.	Torque measurement setup and measured torque data for different frequencies	71
5.6.	Flatness-based control architecture to stabilize the angle of a 1 DOF robot with PMA-driven joint	73
5.7.	Angle controlled, 1 DOF robot arm is following a given angle trajectory	75
5.8.	Influence of a hysteresis torque compensation to the angle tracking performance of a 1 DOF robot with PMA-driven joint	77
6.1.	Planar robot with 2 DOF and PMA-driven joints	79
6.2.	Desired angle trajectory the 2 DOF robot should follow	81
6.3.	Required torque to follow the desired trajectory for joint 1 and 2, respectively	83
6.4.	Backstepping controller tracking performance with and without additional disturbance torque observer	88
6.5.	Tracking performance of a backstepping controller for time-delayed torque signals with and without additional disturbance torque observer	93
7.1.	Reconstructed CAMOped with PMA-driven joint	96
7.2.	Free-cut of the re-constructed CAMOped	97
7.3.	Torque range CAMOped controller for two DMSP-20-353 connected at half contraction	99
7.4.	Magnitude of the closed pressure loop H_{clp} and its sensitivity \mathcal{S}_p	100
7.5.	CAM controller CAMOped	101
7.6.	Torque over pulley angle during two different exemplary rehabilitation exercises using the CAMOped with PMA-driven joint	102

List of Tables

3.2.	Start points of parameter estimation for all models without units.	34
3.3.	Estimated parameters for F_{Martens} and F_{MartExt} ; optimization start point is given in Table 3.2.	34
3.4.	Maximum force error (3.25) of each model by percentage.	36
3.5.	Estimated parameters for the Maxwell-Slip hysteresis model for a Festo DMSP-20-300	39
6.1.	Constant parameters for the 2 DOF robot extracted from CAD data by Johannes Zawatzki (Research assistant at the Beuth Hochschule für Technik Berlin)	80

Acronyms

CAD computer aided design XVII, 80

CAM controlled active motion XVII, 95, 96, 98, 100, 102, 103, 106

CPM continuous passive motion XVII, 95, 98, 103

DOF degree of freedom XV–XVII, 5–8, 13–17, 19, 44, 54, 65, 66, 68, 71–73, 75–82, 85, 87, 92, 93, 106

FM force map XVII

MIMO multiple-input-multiple-output XVII, 78, 83

PD proportional-derivative XVII

PID proportional-integral-derivative XVII

PMA pneumatic muscle actuator XV–XVII, 1–8, 10, 11, 13, 20–33, 35–57, 59, 62, 64–71, 73, 75–79, 82–84, 89, 90, 92–108

SISO single-input-single-output XVII

TCP tool center point XVII, 5

List of Symbols

Symbol	Unit	Description
$\mathbf{0}_n$	-	Zero matrix with dimension nxn
A	m^2	Area
A_{clp}	-	Closed loop polynomial of the pressure control loop
α	$^\circ$	Function of the error angle
$\tilde{\alpha}$	Nm	Controller torque vector
A_p	-	Denominator of the pressure dynamics in the discrete-time domain
A_w	-	Controller polynomial of the pressure controller
b	-	Critical pressure ratio
B_p	-	Numerator of the pressure dynamics in the discrete-time domain
C	$\frac{\text{m}^3}{\text{sPa}}$	Sonic conductance
c_i	-	Free tunable parameter; $i \in \mathbb{N}$
χ	-	Polytropic exponent
D	m	Diameter
d_i	-	Free tunable parameter; $i \in \mathbb{N}$
D_0	m	PMA tube diameter at zero contraction, i.e. initial length
$\ddot{\varphi}$	rad/s^2	Angular acceleration
δ	1/s	Damping coefficient
Δ_{MS}	m	Maximum strain of spring element of the Maxwell-slip hysteresis model
$\Delta F_{\%}$	%	Force error
δ_{MS}	m	Strain of spring element of the Maxwell-slip hysteresis model
\dot{e}_φ	1/s	Error angular velocity
p_s	Pa	Supply pressure
$\dot{\varphi}$	rad/s	Angular velocity
E	N/m^2	Modulus of elasticity
e	-	Euler number
e_φ	rad	Angle error
η	-	Gear ratio
F	N	Force
$\mathbf{f}_{1,2}$	-	Vector
F_g	N	Gravity force
\mathcal{A}	m^2	Factor of F_{PMA}
\mathcal{B}	N	Factor of F_{PMA}

Symbol	Unit	Description
$\tilde{\mathbf{f}}_{1,2}$	-	Matrix
f_v	Hz	Valve cut-off frequency
g	m/s^2	Acceleration due to gravity
G_p	Ns/kgm^2	Pressure dynamics in the continuous-time domain
H	m	PMA membrane thickness
h	Nm	Coriolis vector
H_0	m	PMA membrane thickness at zero contraction, i.e. initial length
$\mathbf{h}_{1,2}$	-	Matrix
H_{aw-p}	-	Transfer function
H_{clp}	-	Transfer function of the closed pressure control loop
H_d	-	Transfer function
\dot{m}	kg/s	Mass flow
H_p	Ns/kgm^2	Pressure dynamics in the discrete-time domain
H_{rt-p}	-	Transfer function
h_s	m	Height of the center of gravity with respect to a chosen level of zero potential energy
$\hat{\tau}$	Nm	Torque
$\tilde{\mathbf{h}}_{1,2}$	-	Matrix
$V_{1,2}$	-	Lyapunov function
\mathbf{I}_n	-	Unit matrix with dimension nxn
K	-	Matrix
$k_{1,2}$	-	Controller gain
K_d	-	Controller gain
K_i	-	Controller gain
k_{MS}	N/m	Spring stiffness of Maxwell-slip model
K_p	-	Controller gain
$k_{v1,2}$	-	Controller gain
L	m	PMA length
l	m	Length
L_0	m	PMA length at zero contraction, i.e. initial length
\mathcal{K}	Nm	Kinetic energy
\mathcal{L}	Nm	Lagrange function
\mathcal{P}	Nm	Potential energy
L_{Fiber}	m	Fiber length of the fibers inside the PMA membrane
l_s	m	Distance previous joint and center of gravity of the following link
M	kg	Mass matrix
m	kg	Mass
\dot{m}	kg/s	Mass flow
n	-	Number of windings of the PMA membrane fibers
ω_v	$1/s$	Valve angular cut-off frequency
p	Pa	Absolute pressure

Symbol	Unit	Description
$P_{c,o}$	-	Pole in the discrete-time domain
Φ	Nm/s	Time derivative of torque
φ	rad	Angle
\dot{p}	Pa/s	Pressure time derivative
π	-	Circular number
ψ	-	Observer state variable
R	m	Radius
R_{gas}	Nm/kgK	Ideal gas constant
ρ_0	kg/m^3	Density of air under reference conditions
R_p	-	Controller polynomial of the pressure controller
r_s	m	Position vector of the center of gravity
s	-	Imaginary number
\mathcal{S}_p	-	Sensitivity of the closed pressure control loop
σ	N/m^2	Tension
S_p	-	Controller polynomial of the pressure controller
s_{pmc}	-	Factor to adjust the stiffness of a PMA-driven joint with PM converter
H_{st-p}	-	Transfer function
T	K	Temperature
t	s	Time
T_0	K	Temperature of air under reference conditions
τ	Nm	Torque
$\hat{\tau}_u$	Nm	Disturbance torque
θ	rad	Fiber angle of the PMA membrane fibers with respect to the PMA contraction axis
θ_0	rad	PMA fiber angle at zero contraction, i.e. initial length
Θ_s	kgm^2	Inertia with respect to the center of gravity
T_p	-	Controller polynomial of the pressure controller
T_s	s	Sample time
T_v	s	Valve time constant
\vec{e}	-	Unit vector
U_v	-	Laplace transform of the valve control signal u_v
u_v	-	Valve control signal
V	m^3	Volume
ε	-	Strain
\dot{V}	m^3/s	Volume flow
\mathcal{V}	-	Lyapunov function
v_s	m/s	Velocity vector of the center of gravity
W	Nm	Virtual work
ω_0	$1/s$	Eigenfrequency
x_φ	-	State vector of angle error and its time derivatives
\tilde{x}_φ	-	State vector

Symbol	Unit	Description
X_v	-	Laplace transform of the normalized valve slide stroke x_v
x_v	-	Normalized valve slide stroke
y	-	Output signal
z	-	Imaginary number

Bibliography

- [1] 04 2019. URL <https://www.bostondynamics.com/robots>.
- [2] J. Adamy. *Nichtlineare Systeme und Regelungen*. Springer, 2018.
- [3] H. Aguilar-Sierra, R. Lopez, W. Yu, S. Salazar, and R. Lozano. A lower limb exoskeleton with hybrid actuation. In *5th IEEE RAS/EMBS International Conference on Biomedical Robotics and Biomechanics*, pages 695–700. IEEE, 2014.
- [4] G. Andrikopoulos and G. Nikolakopoulos. Humanoid robotic leg via pneumatic muscle actuators: implementation and control. *Meccanica*, 53(1):465–480, Jan 2018. ISSN 1572-9648. doi: 10.1007/s11012-017-0738-6. URL <https://doi.org/10.1007/s11012-017-0738-6>.
- [5] G. Andrikopoulos, G. Nikolakopoulos, and S. Manesis. Incorporation of thermal expansion in static force modeling of pneumatic artificial muscles. In *2015 23rd Mediterranean Conference on Control and Automation (MED)*, pages 414–420, June 2015. doi: 10.1109/MED.2015.7158784.
- [6] G. Andrikopoulos, G. Nikolakopoulos, and S. Manesis. Novel considerations on static force modeling of pneumatic muscle actuators. *IEEE/ASME Transactions on Mechatronics*, 21(6):2647–2659, Dec 2016. ISSN 1083-4435. doi: 10.1109/TMECH.2016.2585503.
- [7] H. Aschemann and E. P. Hofer. Nonlinear trajectory control of a high-speed linear axis driven by pneumatic muscle actuators. In *IEEE Industrial Electronics, IECON 2006-32nd Annual Conference on*, pages 3857–3862. IEEE, 2006.
- [8] H. Aschemann and D. Schindele. Sliding-mode control of a high-speed linear axis driven by pneumatic muscle actuators. *IEEE Transactions on Industrial Electronics*, 55(11):3855–3864, 2008.
- [9] H. Aschemann and D. Schindele. Comparison of model-based approaches to the compensation of hysteresis in the force characteristic of pneumatic muscles. *IEEE Trans. Industrial Electronics*, 61(7):3620–3629, 2014.
- [10] K. J. Åström and B. Wittenmark. *Computer-controlled systems: theory and design*. Dover Publication, Inc., 3 edition, 2013.
- [11] S. Balasubramanian, R. Wei, M. Perez, B. Shepard, E. Koeneman, J. Koeneman, and J. He. RUPERT: an exoskeleton robot for assisting rehabilitation of arm functions. In *Virtual Rehabilitation, 2008*, pages 163–167. IEEE, 2008.

- [12] F. Bandau. EMG-basierte regelung und evaluation eines ellenbogen-exoskeletts. Master's thesis, TU Berlin, 2018.
- [13] P. Beater. *Pneumatic drives*. Springer, 2007.
- [14] J. M. Beer, A. Prakash, T. L. Mitzner, and W. A. Rogers. Understanding robot acceptance. Technical report, Georgia Institute of Technology, 2011.
- [15] P. Beyl, M. Van Damme, R. Van Ham, B. Vanderborght, and D. Lefeber. Pleated pneumatic artificial muscle-based actuator system as a torque source for compliant lower limb exoskeletons. *IEEE/ASME Transactions on Mechatronics*, 19(3): 1046–1056, 2014.
- [16] A. Bicchi, M. A. Peshkin, and J. E. Colgate. Safety for physical human–robot interaction. *Springer handbook of robotics*, pages 1335–1348, 2008.
- [17] I. Boblan. *Modellbildung und Regelung eines fluidischen Muskelpaares*. PhD thesis, Technical University of Berlin, 2010.
- [18] I. Boblan and A. Schulz. A humanoid muscle robot torso with biologically inspired construction. In *ISR 2010 (41st International Symposium on Robotics) and ROBOTIK 2010 (6th German Conference on Robotics)*, pages 1–6. VDE, 2010.
- [19] I. Boblan, J. Maschuw, D. Engelhardt, A. Schulz, H. Schwenk, R. Bannasch, and I. Rechenberg. A human-like robot hand and arm with fluidic muscles: modelling of a muscle driven joint with an antagonistic setup. In *3rd Int. Symposium on Adaptive Motion in Animals and Machines, Technische Universität Ilmenau, Germany*, 2005.
- [20] D. Büchler, R. Calandra, B. Schölkopf, and J. Peters. Control of musculoskeletal systems using learned dynamics models. *IEEE Robotics and Automation Letters*, 3(4):3161–3168, 2018.
- [21] A. Cabos. Parameter identification of a pneumatic servo valve and design of a model-based pressure controller. Master's thesis, TU Berlin, Germany, 2018.
- [22] D. G. Caldwell, N. G. Tsagarakis, S. Kousidou, N. Costa, and I. Sarakoglou. "soft" exoskeletons for upper and lower body rehabilitation - design, control and testing. *International Journal of Humanoid Robotics*, 4(03):549–573, 2007.
- [23] C.-P. Chou and B. Hannaford. Static and dynamic characteristics of mckibben pneumatic artificial muscles. In *Proceedings of the 1994 IEEE International Conference on Robotics and Automation*, pages 281–286 vol.1, May 1994. doi: 10.1109/ROBOT.1994.350977.
- [24] C.-P. Chou and B. Hannaford. Measurement and modeling of mckibben pneumatic artificial muscles. *IEEE Transactions on Robotics and Automation*, 12(1):90–102, Feb 1996. ISSN 1042-296X. doi: 10.1109/70.481753.
- [25] P. Corke. MATLAB toolboxes: robotics and vision for students and teachers. *IEEE Robotics & Automation Magazine*, 14(4), 2007.

- [26] P. Corke. *Robotics, Vision and Control: Fundamental Algorithms In MATLAB® Second, Completely Revised*, volume 118. Springer, 2017.
- [27] P. I. Corke. A robotics toolbox for MATLAB. *IEEE Robotics & Automation Magazine*, 3(1):24–32, 1996.
- [28] A. De Santis, B. Siciliano, A. De Luca, and A. Bicchi. An atlas of physical human–robot interaction. *Mechanism and Machine Theory*, 43(3):253–270, 2008.
- [29] T. Deaconescu and A. Deaconescu. Pneumatic muscle actuated isokinetic equipment for the rehabilitation of patients with disabilities of the bearing joints. In *Proceedings of the International MultiConference of Engineers and Computer Scientists*, volume 2, 2009.
- [30] S. Dirven and A. McDaid. A systematic design strategy for antagonistic joints actuated by artificial muscles. *IEEE/ASME Transactions on Mechatronics*, 22(6): 2524–2531, 2017.
- [31] M. Drummond. Development of a test rig for the automated measurement of the static force characteristic of pneumatic muscle actuators. Bachelor’s thesis, TU Berlin, Germany, 2016.
- [32] *Datasheet - Fluidic Muscle DMSP/MAS*. Festo AG, 2016.
- [33] P. L. Gribble, L. I. Mullin, N. Cothros, and A. Mattar. A role for cocontraction in arm movement accuracy. *Journal of neurophysiology*, 2003.
- [34] H.-W. Grollius. *Grundlagen der Pneumatik*. Carl Hanser Verlag GmbH Co KG, 2012.
- [35] A. Hildebrandt, O. Sawodny, R. Neumann, and A. Hartmann. A cascaded tracking control concept for pneumatic muscle actuators. In *2003 European Control Conference (ECC)*, pages 2517–2522, Sept 2003.
- [36] A. Hildebrandt, O. Sawodny, R. Neumann, and A. Hartmann. Cascaded control concept of a robot with two degrees of freedom driven by four artificial pneumatic muscle actuators. In *Proceedings of the 2005, American Control Conference, 2005.*, pages 680–685 vol. 1, June 2005. doi: 10.1109/ACC.2005.1470036.
- [37] A. Hošovský, J. Pitel’, K. Židek, M. Tóthová, J. Sárosi, and L. Cveticanin. Dynamic characterization and simulation of two-link soft robot arm with pneumatic muscles. *Mechanism and Machine Theory*, 103:98–116, 2016.
- [38] A. Isidori. *Nonlinear control systems*. Springer London, UK, 1995.
- [39] J. Jerosch and M. Prymka. Proprioceptive capacity of the knee joint area in patients after rupture of the anterior cruciate ligament. *Der Unfallchirurg*, 99(11): 861–868, 1996.
- [40] T. Kerscher, J. Albiez, J. Zollner, and R. Dillmann. Evaluation of the dynamic model of fluidic muscles using quick-release. In *Biomedical Robotics and Biomechatronics*,

2006. *BioRob 2006. The First IEEE/RAS-EMBS International Conference on*, pages 637–642. IEEE, 2006.
- [41] F. V. G. C. KG. *Datasheet - Proportional directional control valves MPYE*. Festo Vertrieb GmbH Co. KG, Festo Campus 1 - 73734 Esslingen - Germany, June 2017.
- [42] H. K. Khalil and J. Grizzle. *Nonlinear systems*, volume 3. Prentice hall Upper Saddle River, NJ, 2002.
- [43] M. Knestel, E. Hofer, S. K. Barillas, and R. Rupp. The artificial muscle as an innovative actuator in rehabilitation robotics. *IFAC Proceedings Volumes*, 41(2): 773–778, 2008.
- [44] S. Kriehs. Vergleich verschiedener messprinzipien zur längenmessung pneumatischer muskelaktoren. Bachelor’s thesis, TU Berlin, 2017.
- [45] J. Lei, J. Zhu, P. Xie, and M. Tokhi. Joint variable stiffness of musculoskeletal leg mechanism for quadruped robot. *Advances in Mechanical Engineering*, 9(4): 1687814017690342, 2017.
- [46] C.-J. Lin, C.-R. Lin, S.-K. Yu, and C.-T. Chen. Hysteresis modeling and tracking control for a dual pneumatic artificial muscle system using prandtl–ishlinskii model. *Mechatronics*, 28:35–45, 2015.
- [47] K. M. Lynch and F. C. Park. *Modern Robotics: Mechanics, Planning, and Control*. Cambridge University Press, 2017.
- [48] M. Martens and I. Boblan. Modeling the static force of a festo pneumatic muscle actuator: A new approach and a comparison to existing models. *Actuators*, 6(4.33), 2017.
- [49] M. Martens and I. Boblan. Erratum: Modeling the static force of a festo pneumatic muscle actuator: A new approach and a comparison to existing models. *actuators* 2017, 6, 33. *Actuators*, 7, 2018.
- [50] M. Martens, A. Passon, and I. Boblan. A sensor-less approach of a torque controller for pneumatic muscle actuator driven joints. In *2017 3rd International Conference on Control, Automation and Robotics*, pages 477–482. IEEE, April 2017.
- [51] M. Martens, T. Seel, and I. Boblan. A decoupling servo pressure controller for pneumatic muscle actuators. In *23rd International Conference on Methods and Models in Automation and Robotics*. IEEE, 2018.
- [52] M. Martens, T. Seel, J. Zawatzki, and I. Boblan. A novel framework for a systematic integration of pneumatic-muscle-actuator-driven joints into robotic systems via a torque control interface. In *Actuators*, volume 7, page 82. Multidisciplinary Digital Publishing Institute, 2018.
- [53] M. Martens, J. Zawatzki, T. Seel, and I. Boblan. A pneumatic-muscle-actuator-driven knee rehabilitation device for CAM therapy. In *41st International Engineering in Medicine and Biology Conference*. IEEE, 2019.

- [54] T. V. Minh, T. Tjahjowidodo, H. Ramon, and H. Van Brussel. Cascade position control of a single pneumatic artificial muscle–mass system with hysteresis compensation. *Mechatronics*, 20(3):402–414, 2010.
- [55] H. Murrenhoff. *Grundlagen der Fluidtechnik - Teil 2: Pneumatik*. Shaker, 2 edition, 1998.
- [56] T. Noritsugu and T. Tanaka. Application of rubber artificial muscle manipulator as a rehabilitation robot. *IEEE/ASME Transactions on Mechatronics*, 2(4):259–267, Dec 1997. ISSN 1083-4435. doi: 10.1109/3516.653050.
- [57] T. Noritsugu, M. Takaiwa, and D. Sasaki. Development of power assist wear using pneumatic rubber artificial muscles. *Journal of Robotics and Mechatronics*, 21(5): 607, 2009.
- [58] M. Oliver-Salazar, D. Szwedowicz-Wasik, A. Blanco-Ortega, F. Aguilar-Acevedo, and R. Ruiz-Gonzalez. Characterization of pneumatic muscles and their use for the position control of a mechatronic finger. *Mechatronics*, 42:25–40, 2017.
- [59] Y.-L. Park, J. Santos, K. G. Galloway, E. C. Goldfield, and R. J. Wood. A soft wearable robotic device for active knee motions using flat pneumatic artificial muscles. In *Robotics and Automation (ICRA), 2014 IEEE International Conference on*, pages 4805–4810. IEEE, 2014.
- [60] D. Rager, R. Neumann, and H. Murrenhoff. Simplified fluid transmission line model for pneumatic control applications. In *Proc. 14th Scandinavian International Conference on Fluid Power (SICFP15). Tampere, Finland, May 20-22 2015*.
- [61] J. Sárosi, I. Biro, J. Nemeth, and L. Cveticanin. Dynamic modeling of a pneumatic muscle actuator with two-direction motion. *Mechanism and Machine Theory*, 85: 25–34, 2015.
- [62] D. Schindele and H. Aschemann. Nonlinear model predictive control of a high-speed linear axis driven by pneumatic muscles. In *American Control Conference, 2008*, pages 3017–3022. IEEE, 2008.
- [63] D. Schindele and H. Aschemann. P-type ILC with phase lead compensation for a pneumatically driven parallel robot. In *American Control Conference (ACC), 2012*, pages 5484–5489. IEEE, 2012.
- [64] D. Schindele and H. Aschemann. Model-based compensation of hysteresis in the force characteristic of pneumatic muscles. In *Advanced Motion Control (AMC), 2012 12th IEEE International Workshop on*, pages 1–6. IEEE, 2012.
- [65] H. Schulte. J., “the characteristics of the mckibben artificial muscle,” in [the application of external power in prosthetics and orthotics], washington, dc: Nat. Acad. Sci.-Nat. Res. Council, 1961.
- [66] D. Shin, I. Sardellitti, Y.-L. Park, O. Khatib, and M. Cutkosky. Design and control of a bio-inspired human-friendly robot. *The International Journal of Robotics Research*, 29(5):571–584, 2010.

- [67] B. Siciliano and L. Sciavicco. *Robotics - Modelling, Planning and Control*. Springer-Verlag London, 2012.
- [68] J. Sonnenberg. Dynamische mobilisierung von patienten mittels aktoren. Master's thesis, Beuth Hochschule für Technik Berlin, Germany, 2018.
- [69] T. Thanh and T. Phuc. Neural network control of pneumatic artificial muscle manipulator for knee rehabilitation. *Science & Technology Development*, 11(3), 2008.
- [70] T. D. C. Thanh and K. K. Ahn. Nonlinear PID control to improve the control performance of 2 axes pneumatic artificial muscle manipulator using neural network. *Mechatronics*, 16(9):577–587, 2006.
- [71] B. Tondu and P. Lopez. Modeling and control of meckibben artificial muscle robot actuators. *IEEE Control Systems*, 20(2):15–38, Apr 2000. ISSN 1066-033X. doi: 10.1109/37.833638.
- [72] M. Tóthová and J. Pitel. Simulation of actuator dynamics based on geometric model of pneumatic artificial muscle. In *2013 IEEE 11th International Symposium on Intelligent Systems and Informatics (SISY)*, pages 233–237, 2013. doi: 10.1109/SISY.2013.6662577.
- [73] J. Ueda, D. Ming, V. Krishnamoorthy, M. Shinohara, and T. Ogasawara. Individual muscle control using an exoskeleton robot for muscle function testing. *IEEE Transactions on Neural Systems and Rehabilitation Engineering*, 18(4):339–350, 2010.
- [74] R. Van Ham, T. G. Sugar, B. Vanderborght, K. W. Hollander, and D. Lefeber. Compliant actuator designs. *IEEE Robotics & Automation Magazine*, 16(3):81–94, 2009.
- [75] N. Vitiello, T. Lenzi, S. M. M. De Rossi, S. Roccella, and M. C. Carrozza. A sensorless torque control for antagonistic driven compliant joints. *Mechatronics*, 20(3):355–367, 2010. doi: <https://doi.org/10.1016/j.mechatronics.2010.02.001>.
- [76] T. Vo-Minh, T. Tjahjowidodo, H. Ramon, and H. Van Brussel. A new approach to modeling hysteresis in a pneumatic artificial muscle using the maxwell-slip model. *IEEE/ASME Transactions on Mechatronics*, 16(1):177–186, 2011.
- [77] F. Von Lübken, C. Spengler, C. Claes, M. Melnyk, B. Friemert, and B. U. Orthopädie. Das neuromuskuläre defizit nach ruptur des vorderen kreuzbandes. *Schweizerische Zeitschrift für «Sportmedizin und Sporttraumatologie*, 56(1):17–22, 2008.
- [78] H. Watter. Hydraulik und pneumatik. *Wiesbaden: Vieweg+ Teubner Verlag*, 454: 19, 2008.
- [79] K. C. Wickramatunge and T. Leephakpreeda. Study on mechanical behaviors of pneumatic artificial muscle. *International Journal of Engineering Science*, 48(2): 188–198, 2010.

- [80] K. C. Wickramatunge and T. Leephakpreeda. Empirical modeling of dynamic behaviors of pneumatic artificial muscle actuators. *ISA transactions*, 52(6):825–834, 2013.
- [81] J. Zawatzki. Konstruktion und regelung eines mit pneumatischen muskeln angetriebenen humanoiden nackengelenkes. Master's thesis, TU Berlin, 2018.
- [82] J. Zehetner, J. Reger, and M. Horn. A derivative estimation toolbox based on algebraic methods-theory and practice. In *Control Applications, 2007. CCA 2007. IEEE International Conference on*, pages 331–336. IEEE, 2007.

A. Appendix

A.1. Derivatives for Chapter 3 and 4

$$\frac{\partial V}{\partial L} = \frac{L_{\text{Fiber}}^2 - 3L^2}{4\pi n^2} \quad (\text{A.1})$$

$$\frac{\partial D}{\partial L} = \frac{-L}{n\pi\sqrt{L_{\text{Fiber}}^2 - 3L^2}} \quad (\text{A.2})$$

$$\frac{\partial^2 D}{\partial L^2} = \frac{-\sqrt{L_{\text{Fiber}}^2 - L^2} - \frac{L^2}{\sqrt{L_{\text{Fiber}}^2 - L^2}}}{n\pi(L_{\text{Fiber}}^2 - L^2)} \quad (\text{A.3})$$

$$\frac{\partial E_{\text{ru}}}{\partial L} = 3c_3L^2 + 2c_2L + c_1 \quad (\text{A.4})$$

$$\frac{\partial \mathcal{A}}{\partial L} = \frac{\partial^2 V}{\partial L^2} = -\frac{3L}{2\pi n^2} \quad (\text{A.5})$$

$$\begin{aligned} \frac{\partial \mathcal{B}}{\partial L} = \pi H_0 & \left[L\varepsilon_{\text{pe}} \frac{\partial D}{\partial L} \frac{\partial E_{\text{ru}}}{\partial L} - D\varepsilon_{\text{L}} \frac{\partial E_{\text{ru}}}{\partial L} + L\varepsilon_{\text{pe}} \frac{\partial^2 D}{\partial L^2} + \frac{L}{D_0} \left(\frac{\partial D}{\partial L} \right)^2 \right] + \\ & \pi H_0 \left[\varepsilon_{\text{pe}} \frac{\partial D}{\partial L} - D\varepsilon_{\text{L}} - \varepsilon_{\text{L}} \frac{D}{L_0} - \frac{\partial D}{\partial L} \right] \end{aligned} \quad (\text{A.6})$$

A.2. Derivatives for Chapter 6

$$\tilde{\alpha} = \begin{pmatrix} \tilde{\alpha}_1 \\ \tilde{\alpha}_2 \end{pmatrix} = M\tilde{v}_\alpha + h \quad (\text{A.7})$$

$$\tilde{v}_\alpha = \begin{pmatrix} \tilde{v}_{\alpha 1} \\ \tilde{v}_{\alpha 2} \end{pmatrix} = \begin{pmatrix} \ddot{\varphi}_{\text{d1}} - (1 + k_1)\dot{e}_{\varphi 1} - (k_1 + 2k_{\text{v1}})e_{\varphi 1} \\ \ddot{\varphi}_{\text{d2}} - (1 + k_2)\dot{e}_{\varphi 2} - (k_2 + 2k_{\text{v2}})e_{\varphi 2} \end{pmatrix} \quad (\text{A.8})$$

$$M = \begin{pmatrix} m_{11} & m_{12} \\ m_{21} & m_{22} \end{pmatrix} \quad (\text{A.9})$$

$$\frac{\partial \tilde{\alpha}}{\partial x_\varphi} = \begin{pmatrix} \frac{\partial \tilde{\alpha}_1}{\partial e_{\varphi 1}} & \frac{\partial \tilde{\alpha}_1}{\partial e_{\varphi 2}} & \frac{\partial \tilde{\alpha}_1}{\partial \dot{e}_{\varphi 1}} & \frac{\partial \tilde{\alpha}_1}{\partial \dot{e}_{\varphi 2}} \\ \frac{\partial \tilde{\alpha}_2}{\partial e_{\varphi 1}} & \frac{\partial \tilde{\alpha}_2}{\partial e_{\varphi 2}} & \frac{\partial \tilde{\alpha}_2}{\partial \dot{e}_{\varphi 1}} & \frac{\partial \tilde{\alpha}_2}{\partial \dot{e}_{\varphi 2}} \end{pmatrix} \quad (\text{A.10})$$

$$\frac{\partial \tilde{\alpha}_j}{\partial x_{\varphi,i}} = \frac{\partial m_{j1}}{\partial x_{\varphi,i}} \tilde{v}_{\alpha 1} + m_{j1} \frac{\partial \tilde{v}_{\alpha 1}}{\partial x_{\varphi,i}} + \frac{\partial m_{j2}}{\partial x_{\varphi,i}} \tilde{v}_{\alpha 2} + m_{j2} \frac{\partial \tilde{v}_{\alpha 2}}{\partial x_{\varphi,i}} + \frac{\partial h_j}{\partial x_{\varphi,i}} \quad i = 1, \dots, 4 \quad j = 1, 2 \quad (\text{A.11})$$

$$\frac{\partial m_{11}}{\partial e_{\varphi 1}} = \frac{\partial m_{11}}{\partial \dot{e}_{\varphi 1}} = \frac{\partial m_{11}}{\partial \dot{e}_{\varphi 2}} = 0 \quad (\text{A.12})$$

$$\frac{\partial m_{11}}{\partial e_{\varphi 2}} = -2m_2 l_1 l_{s2} \sin \varphi_2 \quad (\text{A.13})$$

$$\frac{\partial m_{12}}{\partial e_{\varphi 1}} = \frac{\partial m_{12}}{\partial \dot{e}_{\varphi 1}} = \frac{\partial m_{12}}{\partial \dot{e}_{\varphi 2}} = \frac{\partial m_{21}}{\partial e_{\varphi 1}} = \frac{\partial m_{21}}{\partial \dot{e}_{\varphi 1}} = \frac{\partial m_{21}}{\partial \dot{e}_{\varphi 2}} = 0 \quad (\text{A.14})$$

$$\frac{\partial m_{12}}{\partial e_{\varphi 2}} = \frac{\partial m_{21}}{\partial e_{\varphi 2}} = -m_2 l_1 l_{s2} \sin \varphi_2 \quad (\text{A.15})$$

$$\frac{\partial m_{22}}{\partial x_{\varphi,i}} = 0 \quad i = 1, \dots, 4 \quad (\text{A.16})$$

$$\frac{\partial \tilde{v}_{\alpha 1}}{\partial e_{\varphi 1}} = -(k_1 + 2k_{v1}) \quad (\text{A.17})$$

$$\frac{\partial \tilde{v}_{\alpha 1}}{\partial \dot{e}_{\varphi 1}} = -(1 + k_1) \quad (\text{A.18})$$

$$\frac{\partial \tilde{v}_{\alpha 1}}{\partial e_{\varphi 2}} = \frac{\partial \tilde{v}_{\alpha 1}}{\partial \dot{e}_{\varphi 2}} = 0 \quad (\text{A.19})$$

$$\frac{\partial \tilde{v}_{\alpha 2}}{\partial e_{\varphi 1}} = \frac{\partial \tilde{v}_{\alpha 2}}{\partial \dot{e}_{\varphi 1}} = 0 \quad (\text{A.20})$$

$$\frac{\partial \tilde{v}_{\alpha 2}}{\partial e_{\varphi 2}} = -(k_2 + 2k_{v2}) \quad (\text{A.21})$$

$$\frac{\partial \tilde{v}_{\alpha 2}}{\partial \dot{e}_{\varphi 2}} = -(1 + k_2) \quad (\text{A.22})$$

$$\frac{\partial h_1}{\partial e_{\varphi 1}} = 0 \quad (\text{A.23})$$

$$\frac{\partial h_1}{\partial e_{\varphi 2}} = -m_2 l_1 l_{s2} \cos(2\dot{\varphi}_1 \dot{\varphi}_2 + \dot{\varphi}_2^2) \quad (\text{A.24})$$

$$\frac{\partial h_1}{\partial \dot{e}_{\varphi 1}} = -m_2 l_1 l_{s2} \sin(2\dot{\varphi}_2) \quad (\text{A.25})$$

$$\frac{\partial h_1}{\partial \dot{e}_{\varphi_2}} = -m_2 l_1 l_{s2} \sin(2\dot{\varphi}_1 + 2\dot{\varphi}_2) \quad (\text{A.26})$$

$$\frac{\partial h_2}{\partial e_{\varphi_1}} = 0 \quad (\text{A.27})$$

$$\frac{\partial h_2}{\partial e_{\varphi_2}} = m_2 l_1 l_{s2} \dot{\varphi}_1^2 \cos \varphi_2 \quad (\text{A.28})$$

$$\frac{\partial h_2}{\partial \dot{e}_{\varphi_1}} = 2m_2 l_1 l_{s2} \dot{\varphi}_1 \sin \varphi_2 \quad (\text{A.29})$$

$$\frac{\partial h_2}{\partial \dot{e}_{\varphi_2}} = 0 \quad (\text{A.30})$$